ENVIRONMENTAL DEPENDENCE OF THE STELLAR INITIAL MASS FUNCTION

by

Wen-Hsin Hsu

A dissertation submitted in partial fulfillment
of the requirements for the degree of
Doctor of Philosophy
(Astronomy and Astrophysics)
in the University of Michigan
2013

Doctoral Committee:

Professor Lee W. Hartmann, Chair
Professor Fred C. Adams
Lori E. Allen, National Optical Astronomy Observatory
Professor Edwin A. Bergin
Professor Nuria P. Calvet
Assistant Professor Fabian Heitsch, University of North Carolina

To my family.

ACKNOWLEDGMENTS

I would like to thank all the people that helped and supported me throughout my six years in graduate school. Without you, this thesis would not have been possible. My thesis advisor, Lee Hartmann, is the best advisor one can ever wish for. He has given me guidance and insights in every aspect of the thesis. He is not only a great scientist who is full of exciting ideas, but also a wonderful mentor whose advice has contributed significantly to my professional development. He also opened my eyes to the humor and wisdom of Monty Python: Fear, surprise, ruthless efficiency, and near fanatical devotion to the Advisor!

I am very grateful to my committee members, Fred Adams, Ted Bergin, Nuria Calvet, Fabian Heitsch and Lori Allen. They helped keep my project on track through the yearly committee meetings. Their questions helped me clarify ideas that I had not yet fully appreciated and their suggestions pointed me in new directions that I had not thought about before.

I had the pleasure to collaborate with many astronomers both at University of Michigan and other institutions. Lori Allen has been an essential part of my observational project, since she has worked extensively on L1641 going back to her own PhD thesis. It was very generous of her to let me use the Hectospec data, which motivated my entire project and provided a solid foundation for my work to build upon. Tom Megeath, who led the *Spitzer/IRAC* survey of Orion and other star-forming regions, allowed me to use their results in my paper before the data was publicly available. Fabian Heitsch has helped me through many of the pitfalls one can fall through in numerical simulations. Jesus Hernandez and John Tobin taught me everything I know about observations, from making sure to get enough food before heading up the mountains to reducing the data to get stellar properties. In particular, Jesus'

SPTCLASS code saved me from classifying more than a thousand stars by eye.

The observations used in this thesis would not have been possible without the assistance and dedication of the staff at the MDM Observatory, the Magellan Telescopes at Las Campanas Observatory, Chile, and the MMT Observatory, a joint facility of the Smithsonian Institution and the University of Arizona. The thesis is supported in part by the Rackham Dissertation Fellowship, NSF grant AST-0807305 and the Origins grant NNX08AI39G. Chapter 2, 3, 4 are based on publications in the Astrophysical Journal (Hsu et al., 2010, 2012, 2013). Chapter 5 is based on a manuscript submitted to the Astronomical Journal.

Finally, I want to thank my family for their support and understanding. My parents and grandparents always wish I could spend more time at home, but I know they try their best to be supportive of my decisions. I also want to thank Joel Lamb, who will soon become my family, for always being a hopeless optimist through my ups and downs.

CONTENTS

LIST OF FIGURES

Figure

LIST OF TABLES

Table

ABSTRACT

I present an in-depth study of how the stellar initial mass function (IMF) depends on the environmental density from both theoretical and observational aspects.

In the theoretical part of my thesis, I used Gadget-2, an SPH code with sink particles, to test the applicability of competitive accretion in an initially non-clustered environment and see how the resulting IMF depends on the environment. The results show that in a sheet-like geometry, as well as a uniform sphere, the accretion rates of individual sinks follow the Bondi-Hoyle accretion at high masses, resulting in a continual flattening of the slope of the mass function towards an asymptotic form $\Gamma = 1$ where the Salpeter slope is $\Gamma = 1.35$. The asymptotic limit is most rapidly reached when starting from a broad distribution of initial sink masses. In general the higher sink masses are found in simulations with flatter upper mass slopes. Although these simulations are highly idealized, the results suggest that competitive accretion may be relevant in a wider variety of environments than previously considered.

In my observational work, I conducted a survey of the stellar population in the L1641 region, the distributed star-forming region in the Orion A molecular cloud south of the Orion Nebula Cluster (ONC). 864 confirmed low-mass members of L1641 are identified through optical photometry and spectroscopy. Overall, L1641 may contain up to 1600 stars if the disk fraction is constant throughout the cloud. Compared to the standard IMFs (Chabrier, 2005; Kroupa, 2001), L1641 is deficient in O and early B stars to a 3-4σ significance level. I then searched for high-to-intermediate mass members of L1641 in order to make a direct comparison with the mass function of the ONC. The observation that the most massive star in L1641 is a B4 star (corresponding to $7M_{\odot}$) is confirmed. I compared the spectral type distribution to that of the ONC (Hillenbrand, 1997) and the K-band luminosity function to Trapez-

ium cluster (Muench et al., 2002). Based on Fisher's exact test, there is only 3% probability that the ONC and the southern region of L1641 were drawn from the same distribution. This supports the hypothesis that the upper-mass of the IMF depends on the environmental density. Additionally, in an attempt to characterize the highly-extincted population in L1641 and ensure that the luminous members in high extinction regions are not missing, I observed 115 members of L1641 with the MMT and Magellan Infrared Spectrograph in H and K band. The IR spectra, along with 2MASS photometry, are used to characterize the accretion luminosities, spectral-types and ages of the YSOs.

CHAPTER 1

Introduction

1.1 The Stellar Initial Mass Function

The mass of a star is the single most important factor in predicting its evolution, feedback and interaction with the environment. Since most, if not all, stars form with neighbors, it is natural to study how the masses of individual stars relate to the environment they are formed in.

The stellar initial mass function (IMF) describes the relative number of stars as a function of mass when a group of stars are formed. The IMF was first introduced by Salpeter (1955), where he only studied the high-mass end of the distribution and found a power-law slope of α = -2.3 (in linear mass bins) or $-\Gamma$ = -1.3 (in log mass bins). The IMF of many young clusters and the field has been extensively studied. Within the Galaxy, the IMF has been found to be quite consistent from region to region (Bastian et al., 2010). It generally consist of a high-mass power-law tail similar to the Salpeter slope and a characteristic mass of 0.1 - 0.3 $M_\odot$, which generally corresponds to the peak of the IMF. The most widely used parametrization of the IMF are broken power-laws such as the Kroupa (2001) IMF:

$$\xi(m) \begin{cases} = A_0\ m^{-0.3}, & 0.01 M_\odot \leq m < 0.08 M_\odot, \\ = A_1\ m^{-1.3}, & 0.08 M_\odot \leq m < 0.5 M_\odot, \\ = A_2\ m^{-2.3}, & m \geq 0.5 M_\odot, \end{cases} \tag{1.1}$$

or a log-normal distribution with a power-law tail, such as the Chabrier (2005)

IMF:

$$\xi(\log m) = \begin{cases} = A_0 \ \exp\{-\dfrac{(\log m - \log 0.25)^2}{2 \times (0.55)^2}\}, & m < 1 M_\odot, \\ = A_1 \ m^{-1.35}, & m \geq 1 M_\odot, \end{cases} \tag{1.2}$$

1.2 The Origin of the IMF and Competitive Accretion

The IMF is one of the most important observables that can be used to constrain and test star-formation theories. Extensive literature exists to explain the origin of the IMF. While the origin of the IMF remains controversial, there are generally two competing theories, motivated by different interpretations of molecular cloud environments, that are most important and widely discussed (e.g., McKee & Ostriker 2007; Zinnecker & Yorke 2007; Clarke 2009). The first theory starts with molecular clouds that are highly turbulent and supersonic. The dense cores created by supersonic turbulence collapse into individual stars and therefore the dense core mass function (CMF) maps into the stellar IMF (e.g., McKee & Tan 2002; Padoan et al. 2007; Klein et al. 2007). The second theory assumes gravitationally-bound clouds where the gravity of individual clumps or cores produces the supersonic motions. Initial low-mass fragments are made due to thermal physics and turbulence in early stages; then the protostars compete to accrete from the common gas reservoir. In this picture, massive stars are formed by accreting most of their mass through gravitational focusing (e.g., Bonnell et al. 2001a,b, 2007; Bate 2009). In these models, if the potential is dominated by gas, the power-law tail approaches a slope of $\Gamma = 0.5$ whereas if the potential is dominated by stars, the Bondi-Hoyle accretion leads to a power-law tail of $\Gamma = 1$. Zinnecker (1982) also showed mathematically that, in an ideal situation where the gas supply is unlimited and accretion rates scale strictly as $\dot{M} \propto M^2$, the power-law tail will flatten and approach $\Gamma = 1$ asymptotically.

1.3 Environmental Dependence of the Stellar Initial Mass Function

As Bonnell et al. (2007) pointed out, it is easy to develop a theory that has many parameters to explain the population distribution dependent on only one variable, the stellar mass. Therefore a successful theory of the IMF has to reproduce other aspects of real clusters, such as clustering, mass segregation, and multiplicity. One potential test of the theories is whether or how the IMF vary as a function of environment. Besides, the IMF has important implication on the galaxy evolution. In a review paper on this subject, Bastian et al. (2010) concluded that there is no clear evidence for variations of the stellar IMF as a function of initial conditions at the time the review was published, but also pointed to specific local and extragalactic environments where indications of non-standard IMFs need further investigation. In extragalactic environments where the stellar populations are unresolved, the IMF is probed by integrated properties such as near IR, FUV and Hα luminosities. These integrated light studies are complicated by metallicity, extinction and star-formation history and is beyond the scope of my thesis. Here we will focus on Galactic environments where the individual stars are resolved and counting stars is possible.

Non-standard IMFs with flatter high-mass slopes have been observed in starburst clusters such as NGC 3603 (Sung & Bessell, 2004; Stolte et al., 2006; Harayama et al., 2008) and the Arches Cluster (Stolte et al., 2005; Espinoza et al., 2009). In the case of the Arches cluster, the flattening of the IMF can be explained mostly by mass segregation and the global IMF is marginally consistent with the Salpeter value (Espinoza et al., 2009) whereas in NGC 3603, the IMF appears to be flatter than Salpeter even after mass segregation is taken into account. In order to demonstrate that there is an environmental dependence in the IMF, one needs a large contrast in density. Therefore, while observations of massive, dense clusters are important, studies of lower-density regions are also needed to test the hypothesis of universality.

Various studies suggest that IMF in low-density regions may be different than the canonical IMFs, with marginally significant results. For example, Luhman (2000)

found that the IMF for Taurus exhibits a modest deficit of stars above $1M_{\odot}$. Massi et al. (2006) found a drop-off near $10M_{\odot}$ in the combined IMF of the six small embedded clusters in the Vela-D molecular cloud, while the combined stellar content would predicts a star with mass $> 22.5M_{\odot}$. Kirk & Myers (2012) found that in a compilation of nearby star-forming regions, the mean stellar mass is higher in higher density regions, even though they did not take into account the bias as a result of varying extinction. Kryukova et al. (2012) found that the protostars with the highest luminosities in Orion preferentially reside in regions of highest surface density of YSOs. Weidner & Kroupa (2006) and Weidner et al. (2010) proposed that there is a relation between the highest mass of a member of a cluster (m_{max}) to the total mass of the cluster (M_{cl}), indicating that high-mass stars form exclusively in massive clusters. Weidner et al. (2010) attributes this to the interplay between stellar feedback and the binding energy of the cluster-forming molecular cloud core. Theoretically, Bonnell et al. (2004) also proposed a similar relation based on simulations of competitive accretion simulations. In their simulations, the most massive star tends to form in the center of a cluster and gains the majority of its mass from the infalling gas onto the cluster, which is accompanied by newly formed low mass stars. Therefore, the formation of the high-mass stars correlates with high stellar surface density. The Weidner & Kroupa (2006) and Bonnell et al. (2004) M_{cl} - m_{max} relations are almost identical for clusters up to a few thousand $M_{\odot}$. In the competitive accretion models, high-mass stars are can only be formed in dense regions near the center of the cluster. On the other hand, the core collapse models (e.g., McKee & Tan 2002; Padoan et al. 2007; Klein et al. 2007) and models that include radiation and feedback (e.g., Krumholz et al. 2012) tend to form more high-mass stars in dense regions, even though it is still possible to form high-mass stars in low-density regions. This is also consistent with the finding by Lamb et al. (2010) where they find high-mass stars in very sparse, low-density regions, even though an unknown fraction of these could be run-away stars that are ejected from high-density clusters.

1.4 The Orion A Molecular Cloud – an Ideal Laboratory

Finding observational evidence of IMF variations has proven to be challenging. On one hand, one needs to study a large stellar population in order to sample the high-mass end of the IMF. Elmegreen (2009) conducted a numerical experiment to show how drastically the rms error in the IMF fitting decreases with the mass of the cluster (Figure 3 and 4 in the paper). A cluster of $1000M_{\odot}$or more is needed in order to constrain the upper-IMF slope down to rms of 0.2. On the other hand, one needs to be able to resolve individual stars and characterize the lower-mass population.

The Orion A cloud is the best laboratory to test the proposition that fewer high-mass stars are formed in lower-density environments. At a distance of $\sim$ 414 pc (Menten et al., 2007; Kim et al., 2008), the Orion Nebula Cluster (ONC) is the closest young cluster with enough stars to show a statistically-significant, well-populated upper IMF. It has been well-characterized with optical spectra of $\sim$ 1600 members (Hillenbrand 1997) and K-band surveys penetrating the high-extinction regions (Muench et al. 2002). It has 2 O stars and seven early B stars (earlier than B4) and its IMF is consistent with the Chabrier IMF, with a Salpeter upper-mass slope (Bastian et al. 2010). The surface density of the molecular gas is ~ 300 $M_{\odot}$ pc^{-2} for the whole ONC. The stellar surface density is ~ 1000 pc^{-2} for the Trapezium cluster and ~ 200 pc^{-2} for the whole ONC. The lower part of the Orion A cloud, south of the ONC, is the lower-density, lower-extinction L1641 cloud. The number of stars in L1641 is comparable to that in the ONC ($N > 1000$; Hsu et al. 2012). Unlike the ONC, the L1641 region has small aggregates of YSOs, but not large-scale clustering (Allen & Davis, 2008). The typical gas surface density (~ 30 $M_{\odot}$ pc^{-2}) and the stellar surface density (~ 10 pc^{-2}) in L1641 are both lower than the ONC values. The earliest star in this region is B4, and there are only five late B stars projected on the cloud.

Megeath et al. (2012) conducted a thorough survey of the Orion A cloud with *Spitzer/IRAC* as part of the Gould's Belt survey [1]. They identified IR-excess objects

[1] `http://www.cfa.harvard.edu/gouldbelt/`

in the Orion A cloud, including more than seven hundred in the L1641 region. The work of Megeath et al. (2012) provides the basis of my thesis work, where I search for evidence of IMF dependence on the environment.

1.5 Thesis Overview

My thesis work consist of three peer-reviewed papers and one paper that has been submitted. Chapter 2 is based on Hsu et al. (2010), where we conduct a numerical experiment to investigate whether competitive accretion is applicable in a non-clustered, sheet-like cloud. Chapter 3 and Chapter 4 focus on observation of the L1641 cloud. In Chapter 3, we surveyed the low-mass population of L1641, finding that given the large number of low-mass stars in L1641, we would expect stars with masses higher than $7M_{\odot}$if the IMF were standard (Hsu et al., 2012). In Chapter 4, we expand our survey of L1641 to the high-to-intermediate mass population and compare the spectral type distribution and the K-band luminosity function to that of the ONC. Our results show that the L1641 is indeed deficient in high-mass stars (Hsu et al., 2013). In Chapter 5, we study the more extincted population of IR-excess objects in L1641 with IR spectroscopy in an attempt to ensure that we are not missing luminous members in high extinction regions.

CHAPTER 2

Competitive Accretion in Sheet Geometry and the Stellar IMF

2.1 Introduction

The stellar initial mass function (IMF) among other things determines the fraction of stellar populations in massive stars; this in turn affects the production of heavy elements, the stellar feedback of energy into the ISM, and the evolution of galaxies. Salpeter (1955) first pointed out the power law distribution in the "original mass function"; subsequent observational work has established the general form of the IMF, which at high masses is still comparable to the "Salpeter slope" Γ, where $dN/d\log M = M^{-\Gamma}$, $\Gamma = 1.35$. The most widely used functional form is a power-law distribution or a combination of power-law distribution at different mass ranges. Other widely used forms of the IMF include log-normal distributions and combination of power-law and log-normal distribution (e.g. Chabrier, 2003; Bastian et al., 2010). As Bonnell et al. (2007) noted, the essential features of the IMF include a peak at a mass of a few tenths of $M_\odot$ and a declining power-law tail toward higher masses.

While the origin of the IMF remains a matter of extensive debate, two general ideas have come to prominence in recent years (e.g., Clarke 2009). The first supposes that the mass spectrum of dense structures within star-forming clouds, suggested to be the result of supersonic turbulence, more or less directly maps into the stellar mass distribution (e.g., Padoan & Nordlund 2002; Klein et al. 2007). In these models the IMF results from local mass reservoirs that are relatively isolated (Padoan et al., 2007; Hennebelle & Chabrier, 2008), possibly affected by gravity (Klessen et al., 2000; Klessen & Burkert, 2001). The second type of model invokes two processes

to produce the IMF; the low-mass end is determined by turbulence and thermal physics, qualitatively similar to the first picture, but the high-mass "tail" is a result of continuing accretion from a mass reservoir (e.g., Zinnecker 1982; Bonnell et al. 2001a,b, 2007). Thus the accumulation of material by the most massive stars is the result of non-isolated accretion, from size scales greater than the local Jeans length. The process resulting in producing the high-mass end of the IMF in this approach is usually called "competitive accretion" (CA).

As summarized by Clark et al. (2009) and Bonnell et al. (2007), the high-mass power-law tail in CA simulations typically arises from formation in a stellar cluster; the potential well results in high gas densities near the center, helping to feed material into the most massive objects (see also Bate 2009). Bonnell et al. (2001b) found that the slope of the mass function depended upon whether the gravitational potential was dominated by gas - in which case they found an asymptotic limit of $\Gamma = 0.5$, due to tidal lobe limitation of mass accretion; or by stars, in which case the asymptotic limit was $\Gamma = 1$, where Bondi-Hoyle accretion dominates. The latter is consistent with the analysis of Zinnecker (1982), who showed that $\Gamma = 1$ results asympotically from accretion rates which scale as $\dot{M} \propto M^2$.

These investigations suggest that CA can account for the high-mass end of the IMF in clusters. However, while most stars form in clusters, a non-negligible number do not, at least in the solar neighborhood. In addition, the properties of clusters vary widely, with most being relatively small (Lada & Lada 2003); this raises the question as to whether the IMF might be affected by the mass of the cluster. Moreover, the initial states and evolution of protocluster clouds and clusters are uncertain; current assumptions range from relatively slow evolution in a roughly virialized condition (e.g., Tan, Krumholz & McKee 2006) to the the opposite assumption of rapid gravitational collapse (e.g., Tobin *et al.* 2009; Proszkow *et al.* 2009). We are therefore motivated to investigate a schematic model of competitive accretion which does not employ the assumption of formation in an initially clustered environment. In addition, we wish to adopt a simple initial physical model with as few parameters as possible to isolate the most important properties for producing the high-mass IMF.

In this chapter, we report a set of numerical simulations in a simplified model to address some general aspects of competitive accretion. Our results suggest that values of Γ close to the Salpeter slope can result in a wider variety of environments than previously discussed; they also suggest that the value of Γ may be correlated with the maximum mass achieved through CA. These findings suggest additional new approaches for numerical simulations of the production of stellar IMFs.

2.2 Model and Methods

Our initial setup is motivated by our models of molecular cloud formation as a result of large-scale flows in the interstellar medium (Heitsch et al., 2006; Vázquez-Semadeni et al., 2006; Heitsch & Hartmann, 2008; Heitsch et al., 2008a,b). In these models the dense material formed in post-shock gas is geometrically thin rather than spherical, due to post-shock compression by large-scale flows (e.g., Hartmann, Ballesteros-Paredes & Bergin 2001). As there is no particular mechanism which would enforce virialization, the cloud as a whole collapses laterally under gravity; eventually, much if not most of the supersonic motion in the cloud is due to acceleration by the cloud's self-gravity, rather than the initial turbulent velocities injected during cloud formation (e.g., Heitsch *et al.* 2008; Heitsch & Hartmann 2008). The most important role of this mostly gravitationally driven turbulence in the post-shock gas is to provide density enhancements which can gravitationally collapse faster than the cloud as a whole (Heitsch, Hartmann, & Burkert 2008).

We adopt an extremely simplified version of this cloud formation model; specifically, we use an initially circular isothermal sheet with many thermal Jeans masses initially in hydrostatic equilibrium in the short dimension. We then introduce local Jeans-unstable mass concentrations in a spatially-random pattern within a given radius which rapidly form sink particles (protostars). For simplicity we do not introduce initial velocity perturbations; instead, we allow the cloud and sinks to evolve under their own gravity. The random placement of the sinks (along with any density fluctuations imposed in the gas) quickly results in complex "turbulent" gas velocities which are gravitationally-generated. This setup allows us to avoid the issue of frag-

mentation for the present and concentrate on the development of CA in an initially non-clustered environment with a minimum of free parameters.

We use Gadget-2 (Springel et al., 2001; Springel, 2005) to simulate the gas dynamics and the formation of "protostellar" sink particles. Jappsen et al. (2005) implemented the sink particle formulation into the form of Gadget-2 we use. Collapsing structures above a density threshold ($n = 10^7 \mathrm{cm}^{-3}$ in our case) are replaced by sink particles, which interact with gas and other sink particles through only gravity.

For simplicity, we assume an isothermal equation of state at 10 K for the gas particles, with a molecular weight of $\mu = 2.36$. We use a code unit system in which the unit length is 1 pc, the unit time is 1 Myr and the unit mass is 0.058 $\mathrm{M}_\odot$. In these units the radius of the sheet is then 2 pc and the total mass of the sheet is 820 $\mathrm{M}_\odot$. The surface density of the unperturbed sheet is $1.37 \times 10^{-2} \mathrm{g\,cm}^{-2}$ ($A_V = 3.8$ perpendicular to the sheet). The (initial) number of gas particles in each simulation is $N_{tot} = 1.6 \times 10^6$. For convenience we report results scaled to the above physical units, but note that the simulations can be rescaled given the assumed isothermal equation of state. Specifically, if the unit length is scaled to d pc, the unit of time becomes d Myr and the unit of mass becomes $0.058\, d\, \mathrm{M}_\odot$.

The initial vertical structure of the sheet follows

$$\rho(z) = \rho_0 \ \mathrm{sech}^2(\mathrm{z/H}), \tag{2.1}$$

with $\rho_0 = 3.7 \times 10^{-20}$ g cm^{-3} and scale height $H = 0.06$ pc. However, the equilibrium density distribution of an isothermal infinite sheet will follow the same form, with a scale height of $H = c_s^2(\pi G \Sigma)^{-1} = 0.04$ pc.

In x and y directions, the gas particles are randomly placed in a uniform sheet, with a radius of 2 pc (except for the non-uniform sheet case, see Section 2.3.2). This leads to density fluctuations due to the random positioning of the particles. To plot the surface density and velocity fields, we interpolated the densities and velocities of the SPH particles onto a rectangular grid. Each cell has an area of $(0.015)^2$ in code unit or $(0.015\mathrm{pc})^2$.

We start each simulation with 100 Jeans unstable clumps. The rapid collapse of these clumps leads to dynamic creation of sink particles before 0.1 Myr. We were unable to put sinks in at the start, probably because of problems with the boundary conditions around the sinks; when the sinks are dynamically created within the simulation, the boundary conditions are properly calculated to account for the discontinuities in density and gas pressure around the sinks (Bate et al., 1995; Jappsen et al., 2005).

Because the sheet itself is also highly Jeans unstable, it also collapses under gravity, on a timescale $t_c \sim R(\pi G\Sigma)^{-1/2} \approx 1.4 Myr$ (Burkert & Hartmann 2004; hereafter BH04). Due to gravitational focusing, a ring of material piles up quickly along the edge of the cloud. The edge can then become gravitationally unstable and fragment (BH04; Vázquez-Semadeni et al. 2007; Figure 2.1). With our isothermal equation of state, we find relatively uncontrolled (numerically) fragmentation in this ring; we therefore turn off the creation of sinks after the initial 100 clumps collapse, allowing us to focus entirely on competitive accretion within the main body of the cloud. Our restriction on the initial placement of clumps to a radius of 1 pc avoids accretion from the ring.

Gas particles that come within a certain radius of a sink (0.003 pc in our setup) are tested for accretion individually. If a gas particle is bound to a sink, the gas particle is accreted by the sink. Gas particles which come within 0.0003 pc of the sink are always accreted. We ran each simulation for 1.2 Myr, or approximately 0.8 t_c, with an output file written every 0.1 Myr.

Within this general setup we considered several cases. In the first set of simulations, we assumed a uniform surface density for the cloud and that each clump had the same mass, $0.82 M_\odot$. In a second set, we assumed the same equal initial clump masses, but a varying density distribution in the gas. The final sets of simulations assumed constant surface density gas but log-normal initial mass distributions for the clumps, keeping the total mass of the clumps to be 10% of the cloud mass. To improve statistics, we ran six realizations of each of the simulations described above, differing only in the random positions of the clumps.

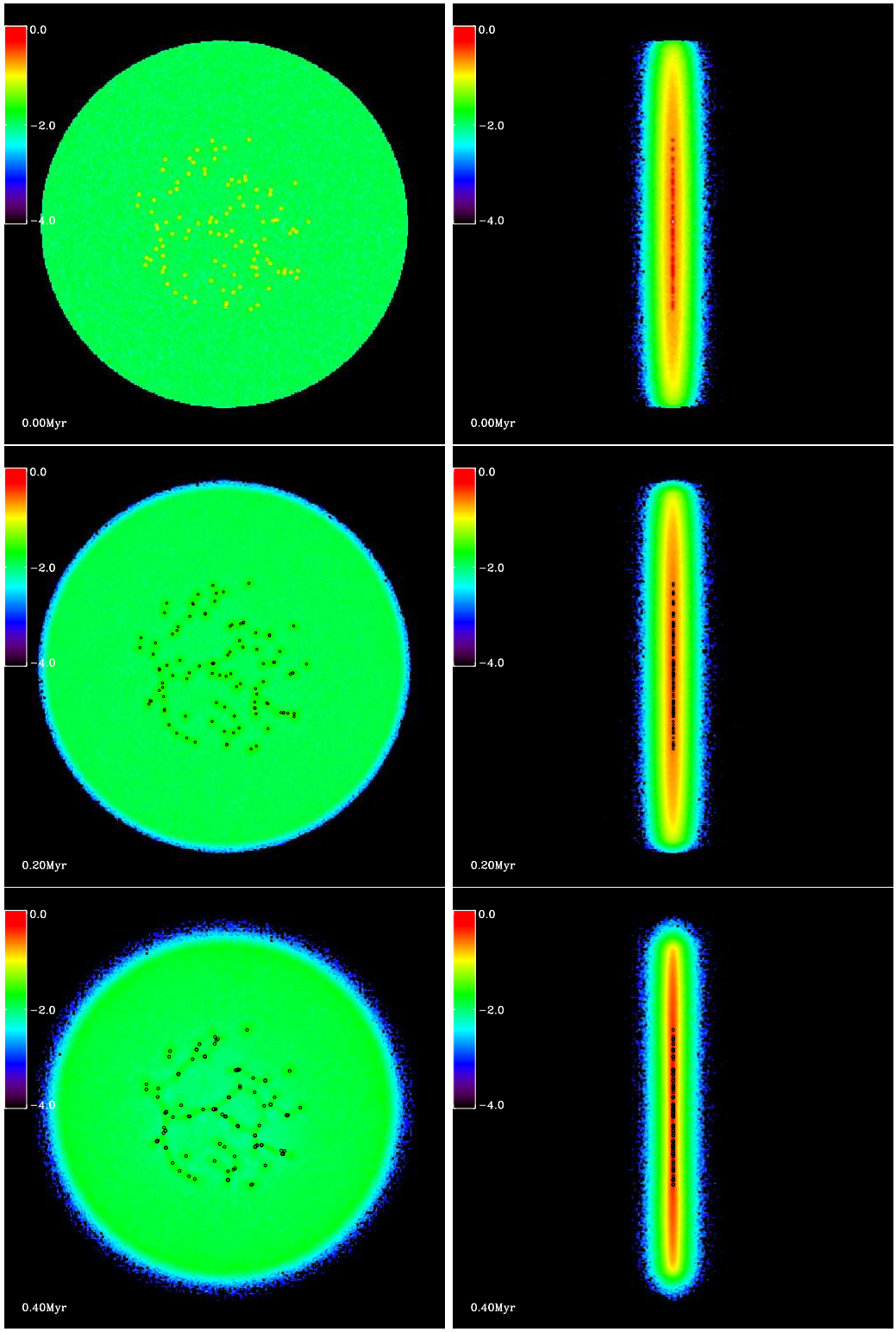

Figure 2.1: The collapse of a sheet-like molecular cloud and the growth of the clumps in a simulation at 0, 0.2, 0.4, 0.6, 0.8, 1.0 and 1.2 Mpc. The left panel is the molecular cloud as viewed from the top, and the left panel from the side. Each box is 4.8 by 4.8 pc. The colors correspond to the logarithm of column density in g cm^{-2}.

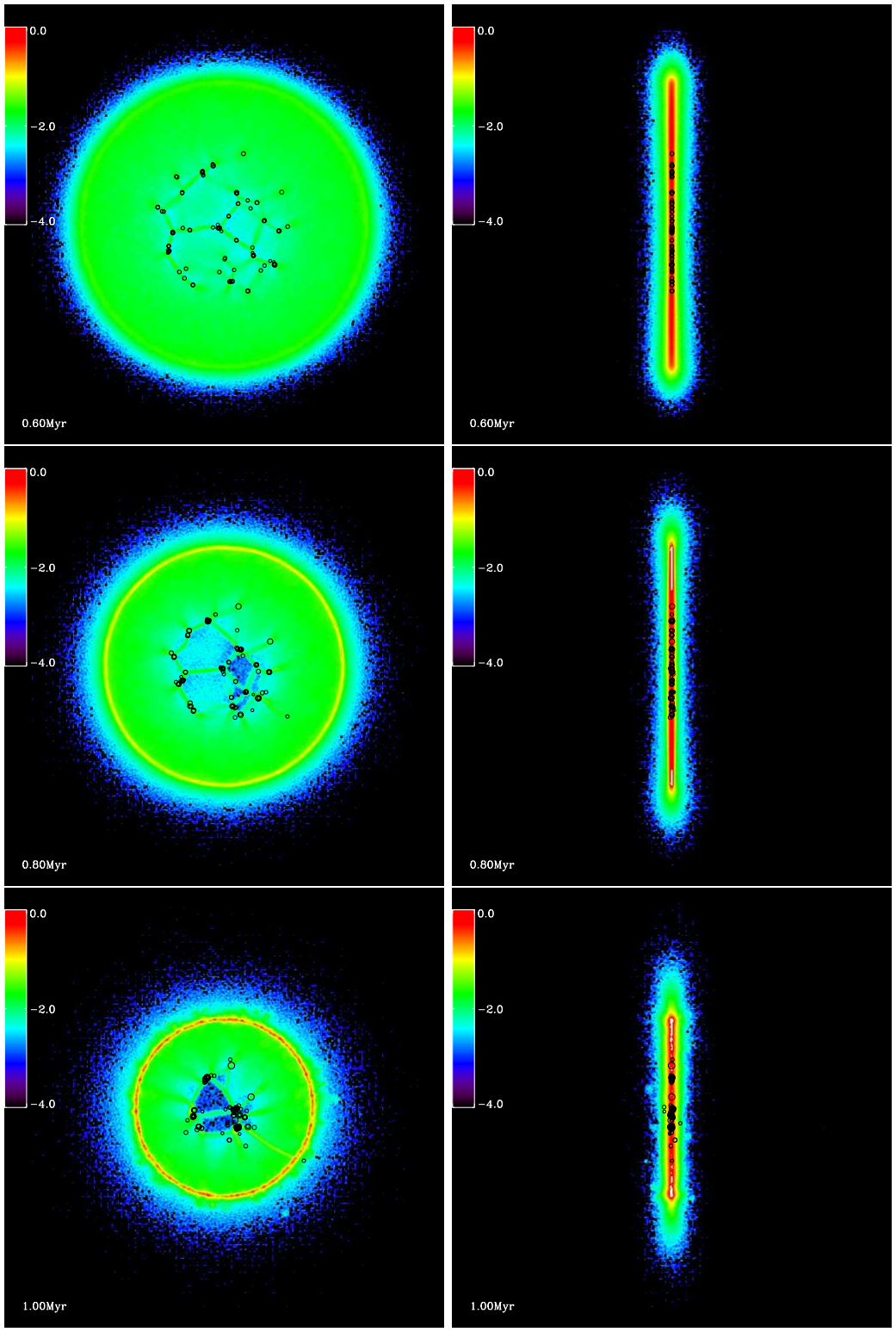

Figure 2.1: (Continued)

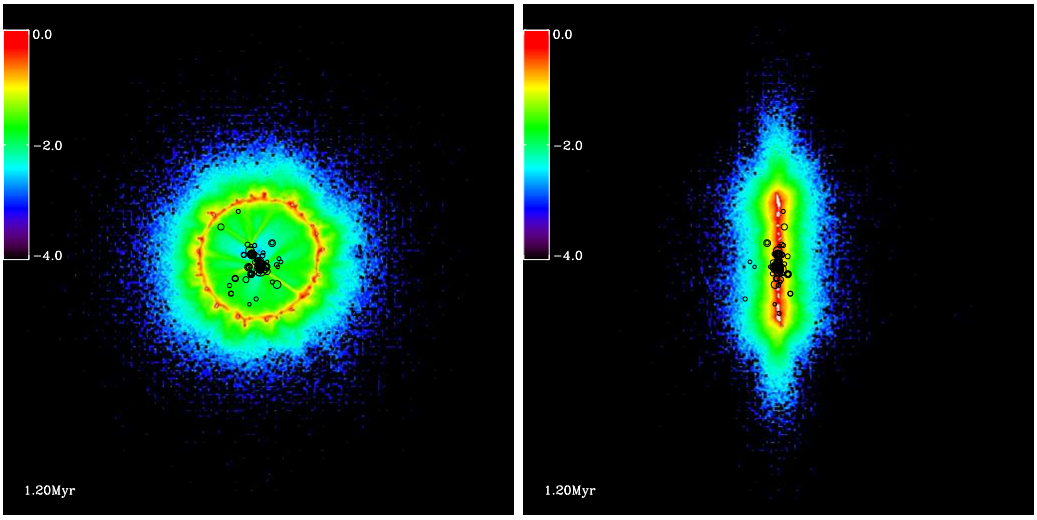

Figure 2.1: (Continued)

2.3 Results

2.3.1 Equal Mass Clumps in a Uniform Sheet

Figure 2.1 shows one of the realizations of the simplest case, equal mass clumps in a uniform sheet. The left panel shows the view from the top, and the right panel shows the side view. Figure 2.2 shows a close-up view of the central 2.4 by 2.4 pc. The circles mark the location of the sink particles, and the area of the circles correspond to the mass of the sinks.

Early on (before 0.2 Myr), most sinks evolve independently of each other, accreting mass from the original clump and the environment. However, as the entire cloud collapses, after 0.2 Myr, the sink particles start to affect each other, forming small groups, in a manner reminiscent of the simulations of Bonnell et al. (2003) (see also Maschberger et al. 2010). By 0.5 Myr, the gas between the sink particles starts to form a filamentary structure that resembles the "cosmic web" in cosmological simulations. At this stage, part of the gas is accreted first onto the filament, and then from the filament to the sinks. The regions between the web become depleted of gas. As time goes on, the small groups collapse, creating larger groups while the sink particles accrete gas from the environment. The more massive sinks in a group can accrete mass faster, thus broadening the mass distribution

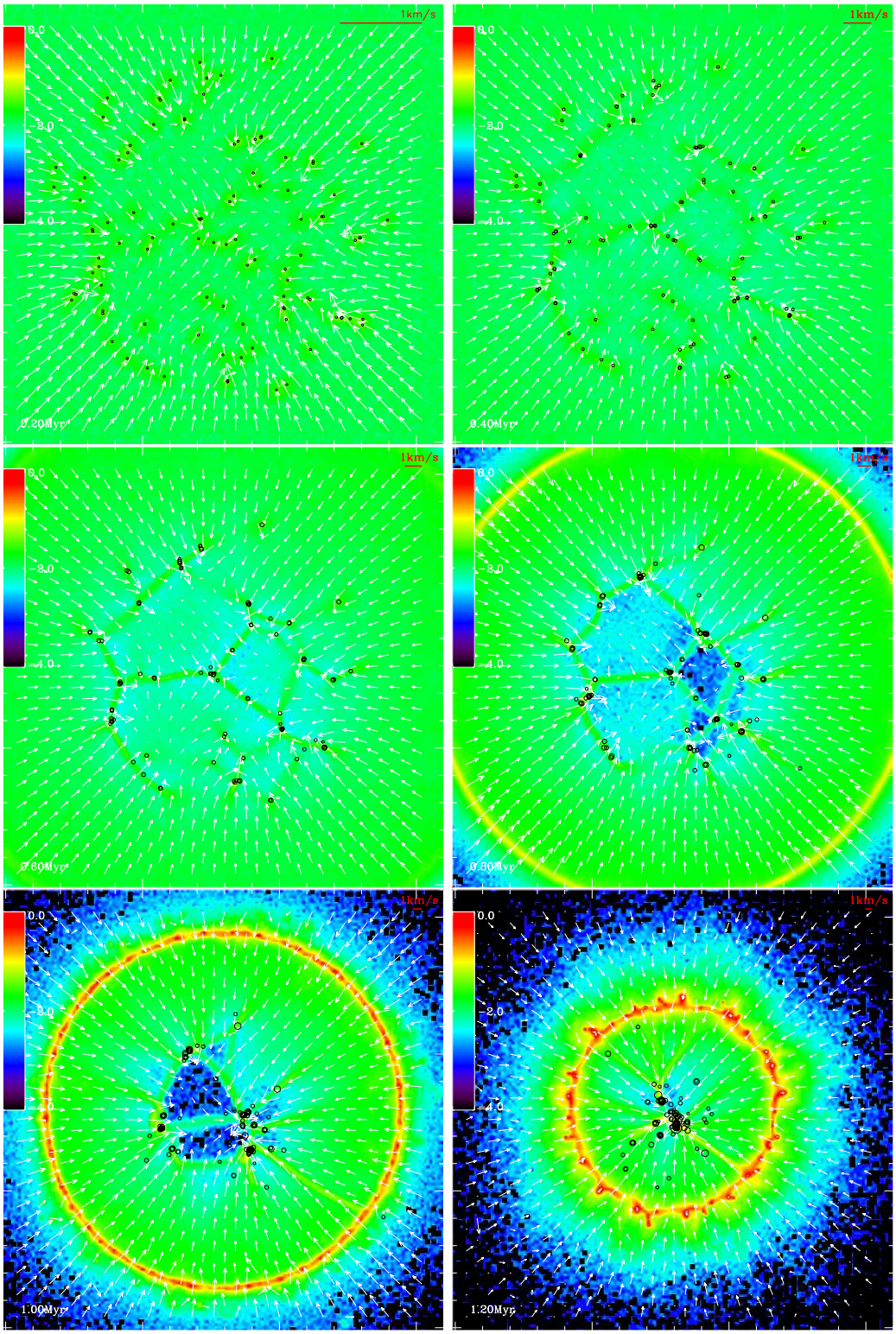

Figure 2.2: Collapse of a sheet-like molecular cloud zooming in on the inner part. The same simulation as in Figure 2.1. Each box is 2.4 pc by 2.4 pc. The arrows indicate the velocity vectors of the gas, with 1 kms^{-1} marked on the upper right corner of each panel. The colors correspond to the log of column density in g cm^{-2}.

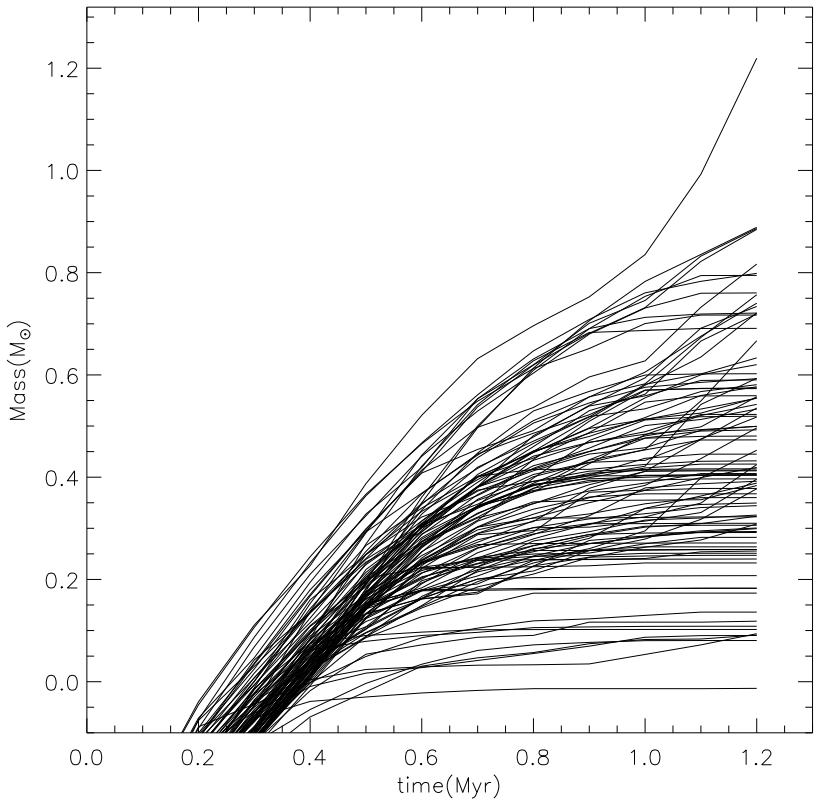

Figure 2.3: Evolution of sink mass as a function of time in one of the runs of the equal mass case.

Table 2.1. Fitting range and slope of the mass function

Case	Background	Clump Mass	Fitting Range $\log(M_\odot)$	Slope	Final Mass in Sinks %
1	uniform	same	0.4 - 1.15	-2.07± 0.15	39%
2	varying	same	0.4 - 1.15	-1.97 ± 0.15	40%
3	uniform	gaussian ($\sigma = 0.05$)	0.4 - 1.15	-1.67± 0.14	40%
4	uniform	gaussian($\sigma = 0.1$)	0.45 - 1.2	-1.42 ± 0.14	40%
5	uniform	gaussian($\sigma = 0.2$)	0.55 - 1.3	-1.03 ± 0.16	40%

Figure 2.3 shows the growth of each sink particle as a function of time. Initially, all the clumps have the same mass, but the final sink masses span over 1.5 dex in mass. Note that the initial clump mass is not equal to the sink mass when the sinks are created because it takes about 0.2 to 0.4 Myr for the all the clump gas to fall in.

Figure 2.4 shows the mass accretion rate of each sink at intervals of 0.2 Myr, including the sink particles from all six runs. The accretion rates of the more massive sinks exhibit a roughly $dM/dt \propto M(\mathrm{sink})^2$ behavior. As the system evolves, the accretion rates decrease due mostly to the removal of gas into sinks, and the lower-mass sinks lose the competition for material to the high-mass sinks.

As shown in Figure 2.5, in an initially non-clustered environment, the accretion rate shows no clear dependence on the position of the sink within the sheet. This is unsurprising given the uniform nature of the sheet, although the global motions of the sheet do depend upon radius. This is in contrast to formation in an initially clustered environment, as described by Bonnell et al. (2001), where the accretion rate depends on the position of the sink in the cluster through the tidal lobe radius. While the center of the cluster is the preferred location to form the most massive star, the most massive stars in our simulations do not necessarily form in the center (though eventually everything collapses to the center).

The combined mass distribution of the six runs is shown in Figure 2.6. The thin black line represents the initial mass of the clumps. The thick lines show the mass distribution at 0.4, 0.6, 0.8, 1.0 and 1.2 Myrs after the beginning of the simulation. The distribution starts with a delta function, evolves into a Gaussian-like distribution

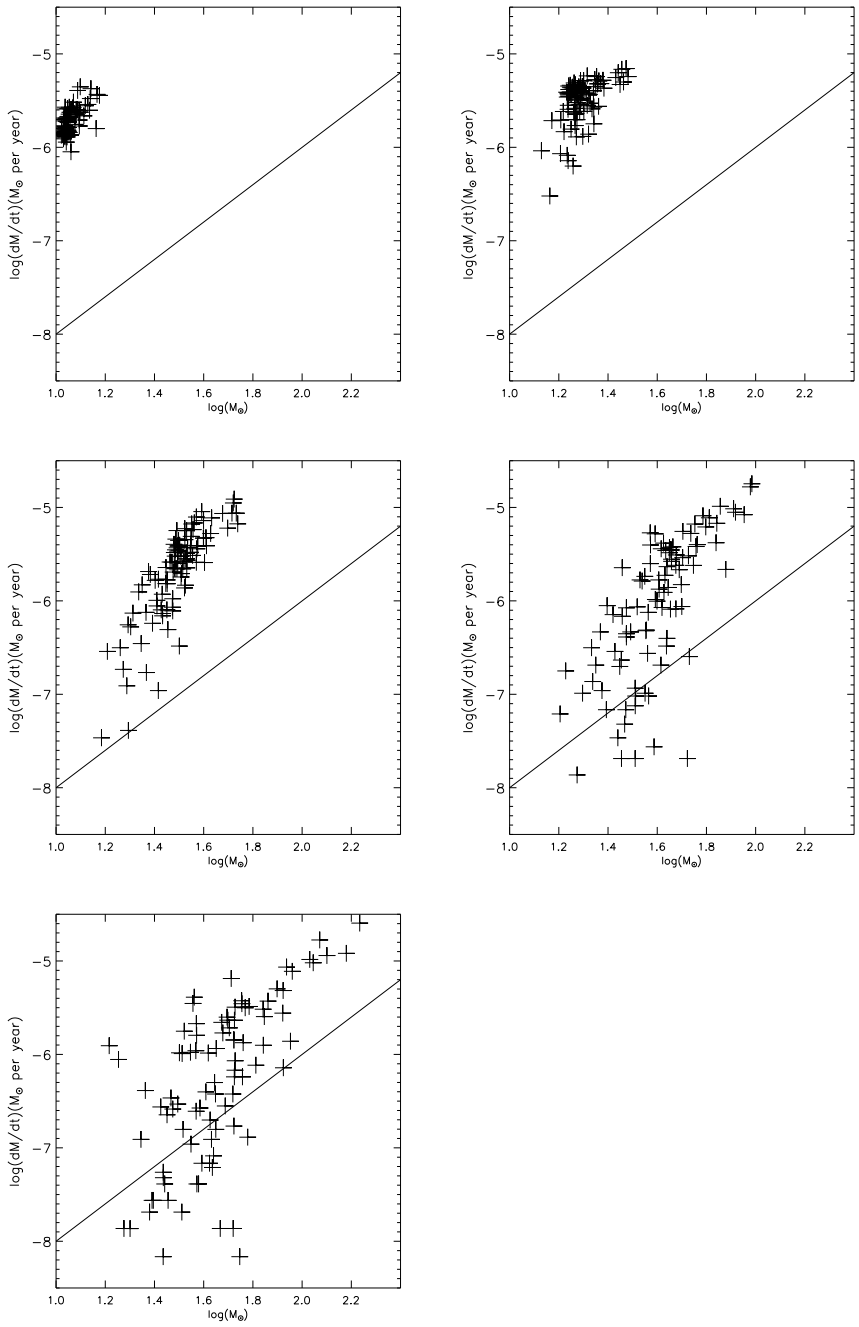

Figure 2.4: Accretion rate vs. mass of sinks at 0.2, 0.4, 0.6, 0.8 and 1.0 Myr in one of the runs of uniform initial sink mass and uniform cloud surface density. The accretion rates for the higher-mass sinks follow $\dot{M} \propto M^2$.

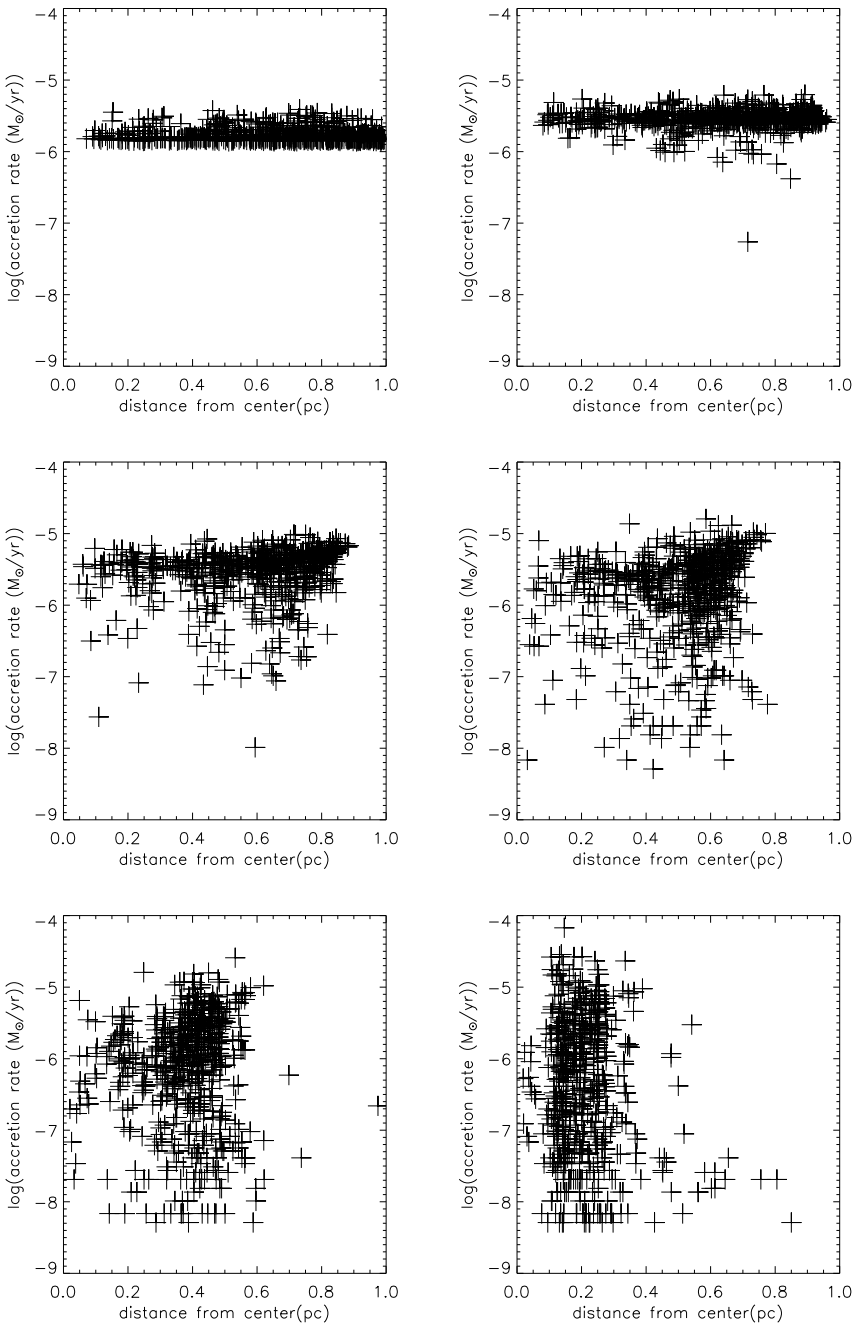

Figure 2.5: The accretion rate vs. distance of sink from the center of the sheet at t=0.2, 0.4, 0.6, 0.8, 1.0 and 1.2 My in uniform initial sink mass and uniform cloud surface density case. All 600 sinks from the six runs are included.

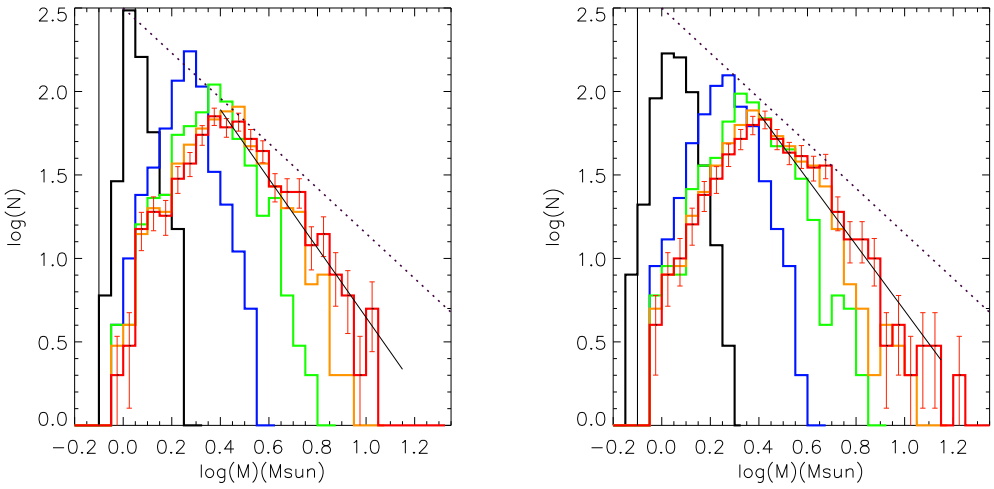

Figure 2.6: Left: Mass distribution of sinks at t=0.4, 0.6, 0.8, 1.0 and 1.2 Myr for the uniform surface density, uniform initial sink mass case. The weighted linear fit has a slope of -2.08. Right: The distribution of mass at t = 0.4, 0.6, 0.8, 1.0 and 1.2 Myr for the varying surface density, equal clump mass case. The weighted linear fit has a slope of $-\Gamma$ = -1.95. The dotted lines represent the Salpeter slope $-\Gamma$ = -1.35 (see Table 2.1).

and then develops a high-mass power-law toward the end of the simulation. The solid black line show a fit to the distribution from $10^{0.4}$ to $10^{1.15}$ $M_{\odot}$when we terminate the simulation, or at $t = 1.2$ Myr, with a slope of -2.07 ± 0.15. The derived slope does depend modestly on the range of masses which are fitted. The slope and the fitting range in mass is tabulated in Table 2.1.

2.3.2 Equal Mass Clumps in a Non-uniform Sheet

The setup is mostly the same as the previous case, but with background density fluctuations. To construct a varying surface density, we used the linear superposition of sine waves in both the x and y directions whose magnitude is proportional to the wavelength:

$$d(x,y) = \sum_{k_x,k_y} k^{-1} \sin(k_x x + \phi_x(k_x)) \sin(k_y y + \phi_y(k_y)),$$

where $d(x,y)$ is the surface density at location x, y; k_x and k_y are the wavenumbers in

x and y directions; ϕ_x and ϕ_y are the randomly chosen phases. The k^{-1} factor is used simply to ensure that the fluctuations are mostly on large scales while still having noticeable effects on smaller scales. On the smallest scales, the density fluctuations are dominated by random positioning of the particles. The largest wavelength allowed is the diameter of the sheet; the smallest wavelength allowed is 1/20 of the diameter. The fluctuating part of the surface density is then added to a constant surface density part so that the minimum density is 30% of the maximum density. The phases of the surface density are randomly chosen for each of the six simulations. Figure 2.7 shows a close-up view of the central 1.2 x 1.2 pc of one of the runs of this case. The fluctuations in the background density are not very prominent in the figure partly because the surface density is plotted on a log scale, and the clumps are dominating the density fluctuations.

In this set of simulations, the accretion rate is again proportional to M(sink)^2 for the more massive sinks (Figure 2.8). The sink mass distribution grows in a similar way as in the previous case, but the distribution spreads to higher masses slightly faster. At $t = 1.2$ Myr, the linear fit to the distribution gives a slope of -1.97 ± 0.15, with a fitting range of $10^{0.4}$ to $10^{1.15}$ $M_\odot$. Thus, including these density fluctuations in the simulation makes little difference to the final result.

2.3.3 Clumps with an Initial Mass Distribution

The previous results suggested that a wider initial distribution of masses should grow the power-law tail faster. We therefore constructed three sets of simulations with initial mass distributions

$$N(\log M) \propto \exp\left(-\frac{(\log M - \log M_c)^2}{2\sigma^2}\right), \tag{2.2}$$

where $\log(M_c/M_\odot) = -0.1$ and $\sigma = 0.05$, 0.1 and 0.2 dex. Figure 2.9 shows the sink mass distributions for these three cases. The thin black lines represent the initial clump mass distributions, and the thick lines are the mass distribution at t=0.4, 0.6, 0.8, 1.0 and 1.2 Myr. The wider distribution of initial clump masses

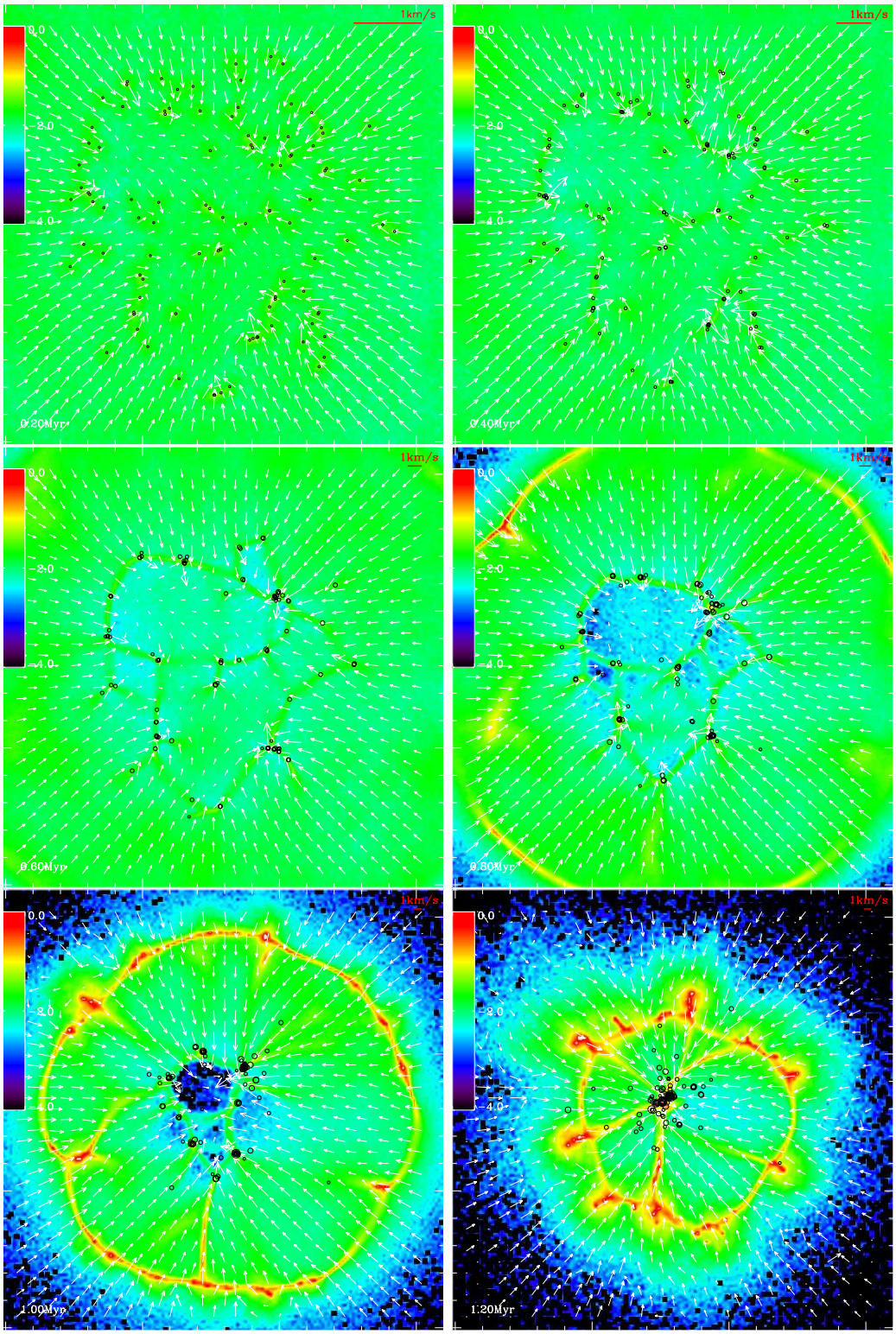

Figure 2.7: Collapse of a sheet-like molecular cloud with equal initial sink mass and surface density fluctuation, zooming in on the inner part. Each box is 2.4 pc by 2.4 pc. The arrows indicate the velocity vectors of the gas, with $1\,\mathrm{km s^{-1}}$ marked on the upper right corner of each panel. The colors correspond to the log of column density in g $\mathrm{cm^{-2}}$.

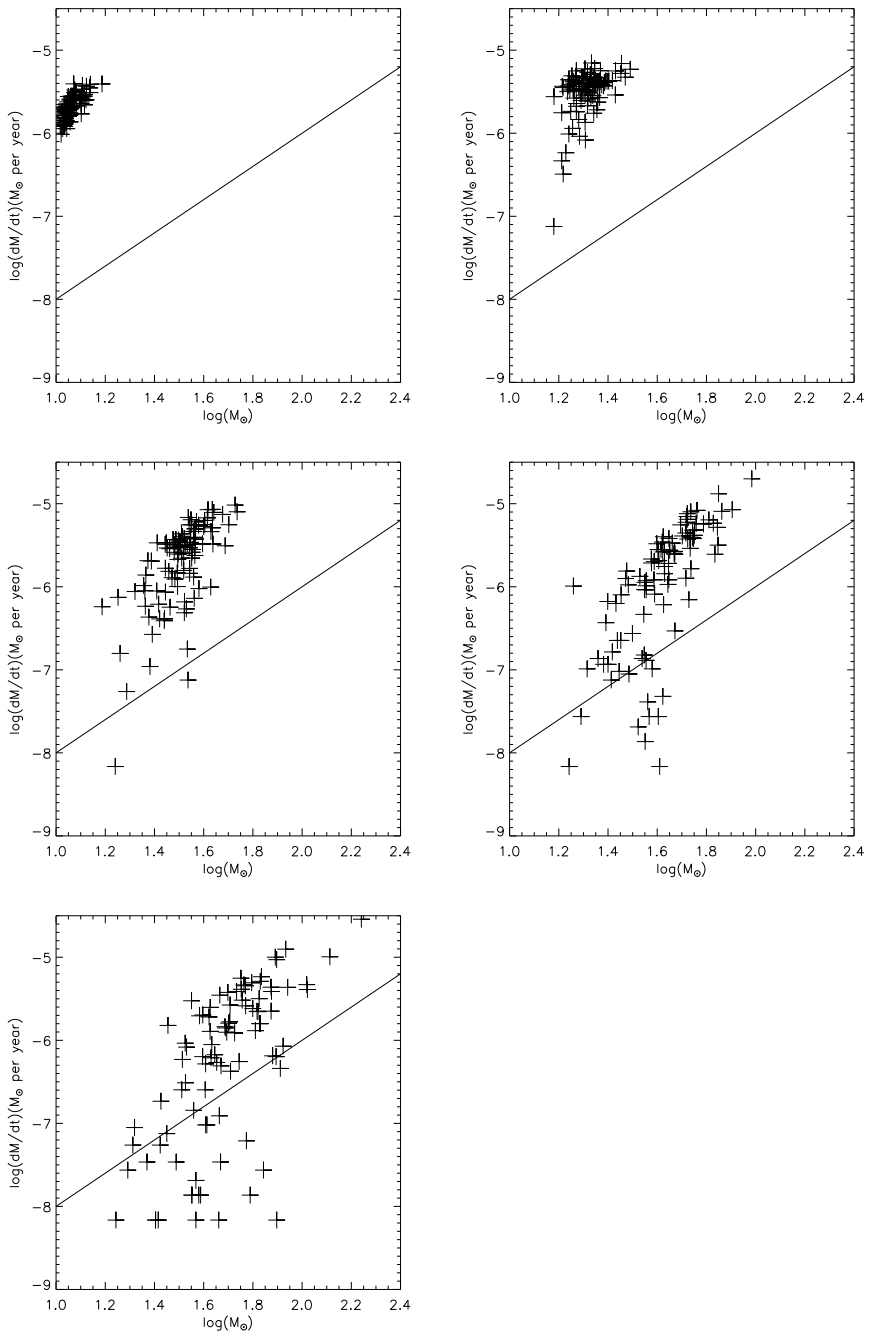

Figure 2.8: Accretion rate vs. mass of sinks at 0.2, 0.4, 0.6, 0.8 and 1.0 Myr in one of the runs of the fluctuating surface density case. The accretion rates for the higher-mass sinks follow $\dot{M} \propto M^2$; the surface density fluctuations have little effect (see Figure 2.4 for comparison).

yields faster growth of the high mass power law, as expected. Linear fits to the final mass distribution at t=1.2 Myr yield slope of -1.67±0.15, -1.42±0.14 and -1.03±0.16. Again, the parameters for the fitting are tabulated in Table 2.1.

The slope of the mass distribution depends on the spread of the initial clump masses. The final slope can be flatter than the Salpeter value of -1.35. In fact, if the mass accretion rate grows strictly as $\dot{M} \propto M^2$, all the slopes would approach -1 if the sinks have enough time and enough gas to accrete (*e.g.* , Zinnecker 1982). Our numerical results are consistent with an asymptotic slope of $\Gamma = 1.0$, although the statistical errors are large enough to prevent an absolutely secure conclusion, even with simulations totalling 600 objects. This emphasizes the long-standing problem of achieving sufficient numbers of objects, either theoretically or observationally, to make firm statistical conclusions about IMF slopes.

2.4 Discussion

2.4.1 Accretion and clustered environments

Figures 2.4 and 2.8 show the main result of this chapter: a strong tendency for $\dot{M} \propto M^2$ to develop at the high-mass end of the sink mass distribution, in initially non-clustered, flat, collapsing cloud environments. This results in a general tendency for the high-mass power low to approach $\Gamma = 1$ asymptotically, depending upon how much mass the sinks can accrete beyond their initial values, as shown in Figures 2.6 and 2.9. To put this in context, we constructed a simple analytic model where an initial Gaussian distribution of masses is modified by accretion with $\dot{M} \propto M^2 = \alpha M^2$, where α is a constant. For an initial mass M_0, the mass grows as a function of time

$$M(t) = \frac{M_0}{1 - \alpha M_0 t} \tag{2.3}$$

(Zinnecker, 1982). The resulting mass grows as $M(t) \rightarrow \infty$ as $t \rightarrow t_\infty = (\alpha M_0)^{-1}$. Figure 2.10 shows how the mass distribution grow with time, plotted in increments of $0.16 t_\infty = (\alpha M_0)^{-1}$. This does a suprisingly good job of reproducing the numerical simulation results, if accretion is stopped at differing times. Even though the

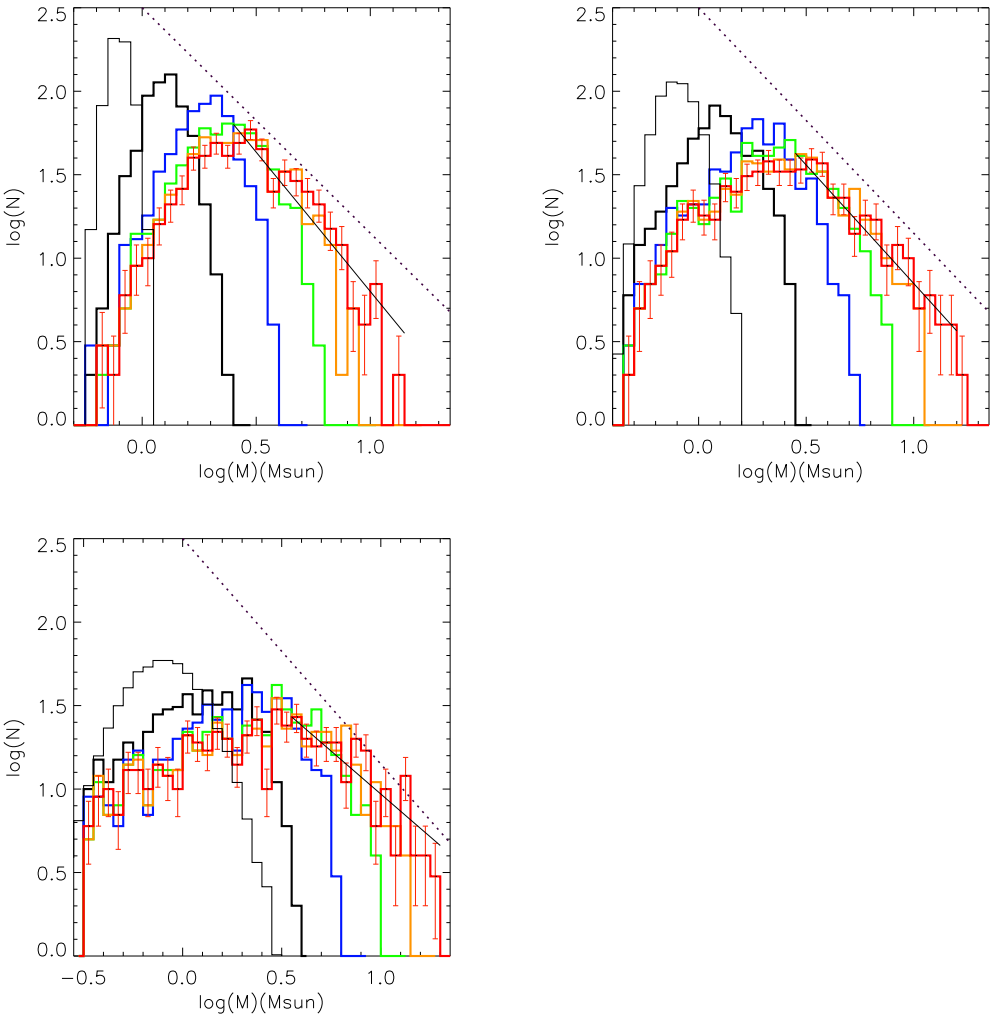

Figure 2.9: Resulting mass distributions for initial clump masses with Gaussian distributions (Top left: σ = 0.05; top right: σ = 0.1; bottom left: σ = 0.2) with constant background density. The linear fit slopes are $-\Gamma$ = -1.66, -1.42 and -1.03, respectively. The thin solid lines represent the initial clump mass distribution. The dotted lines represent the Salpeter slope $-\Gamma$ = -1.35.

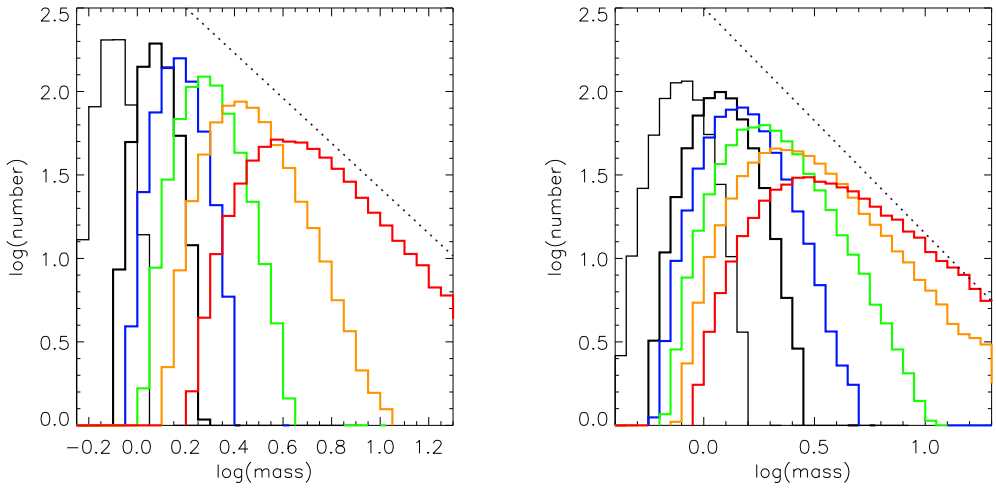

Figure 2.10: Mass distribution of analytical model with $\dot{M} = \alpha M^2$ The left figure has a narrower initial mass range ($\sigma = 0.05$ dex) than the right figure($\sigma = 0.1$ dex). The thin solid line represents the initial distribution of masses, and the colored lines represent the mass distribution in increments of $0.16t_\infty = (\alpha M_0)^{-1}$. The dotted line represent the Salpeter slope $-\Gamma$ = -1.35.

simulation accretion rates do not scale exactly as M^2, with the lower-mass sinks accreting more slowly, this makes little difference on the resulting mass distribution. This comparison emphasizes that the "competitive" effect in CA is not only starving the low-mass systems at the expense of the high-mass objects; in terms of producing the high-mass power-law, it is the result of differential accretion, enhancing the rates at which the higher-mass sinks accrete.

While our starting conditions do not assume an initial clustered structure or a deep central gravitational potential, our assumed cloud symmetry and lack of turbulence or rotation results in forming a cluster of sinks at the center. However, the high-mass tail of the mass function is strongly developing well before the final central cluster is formed. Indeed, we observe $\dot{M} \propto M^2$ at the earliest stages in our simulations, where the clustering is minimal (we also see this in a simulation with sinks in a uniform sphere - unsurprisingly). It does appear that some local grouping is necessary to achieve enough differential accretion to develop a clearly asymmetric mass function, based on simulations (not presented here) that show when the sinks are initially

placed further apart, the groups take longer to form and the high-mass tail of the IMF evolves more slowly.

In our simulations, the local groupings happen relatively quickly compared to the simulation of Bonnell et al. (2001b). This is probably because the relaxation time in a sheet be faster than in a sphere of the same central density and total mass (*e.g.* , Rybicki 1971).

2.4.2 Applicability of Bondi-Hoyle accretion

From their simulations of formation in a cluster potential, Bonnell *et al.* (2001a,b) argued that there are two regimes of accretion. The first phase was where the gravitational potential of the cluster gas dominated, and accretion was tidally limited, leading to a $\Gamma \sim -0.5$. This occurs when both the protostars and the gas both fall in toward the cluster center (see, e.g., discussion in Clark *et al.* 2009, Section 2). During the second phase, the stars dominate the potential, become virialized, and then Bondi-Hoyle accretion leads to an upper mass distribution $\Gamma \rightarrow 1$.

In contrast, we find $\Gamma \rightarrow 1$ even during global collapse, for a situation where the infall velocities tend to be larger at large radii and the average density is roughly constant with position (see also Burkert & Hartmann 2004). This occurs as the groups begin to dominate the local gravitational potential and generate significant relative velocities of the sinks and the infalling gas. This may provide local environments equivalent to the global second accretion regime of Bonnell *et al.* (2001b). The tidal limiting phase is much less important in our simulation because of the shallower gravitational potential gradient of the sheet, so that the characteristic Bondi-Hoyle radius of accretion (see below) is always smaller than the tidal radius.

In the simple, isolated version of Bondi-Hoyle accretion in three dimensions,

$$\dot{M} \propto \rho R_{acc}^2 v \,, \tag{2.4}$$

where ρ is the gas density and v is the (assumed supersonic) relative velocity of the

gas and sink, both averaged at the accretion radius

$$R_{acc} \propto GM/v^2 \,. \tag{2.5}$$

This results in the usual scaling

$$\dot{M} \propto M^2 \rho v^{-3} \,. \tag{2.6}$$

Initially, we thought that in our adopted flat geometry the accretion rates might scale as

$$\dot{M} \propto 2\pi \Sigma R_{acc} v \,, \tag{2.7}$$

where Σ is the gas surface density of the sheet; this would imply

$$\dot{M} \propto M \Sigma v^{-1} \,. \tag{2.8}$$

In fact, the accretion of the sink particles is more like a 3D than a 2D flow. This is because the accretion radius is effectively embedded in the sheet. In the small groups, the velocity dispersion amongst the sinks is about 1- 2 kms^{-1}. The accretion radius is then

$$R_{acc} = 0.08 \left(\frac{M}{10 M_\odot} \right) \left(\frac{v}{1 \text{ km s}^{-1}} \right)^{-2} \text{pc.} \tag{2.9}$$

From the above equation, we conclude that for sink masses up to $10 M_\odot$, the accretion radius is in general smaller than the scale height of the sheet. Thus the mass flow is (non-spherical) Bondi-Hoyle accretion (Bondi & Hoyle, 1944).

It is worth noting that our sheets are undoubtedly much thinner than realistic molecular clouds. Thus, our results suggest that formation of clouds by large scale flows, which tend to produce flattened clouds (see Section 2.4.3, does not alter the basic applicability of Bondi-Hoyle accretion for the upper mass IMF (though conceivably the results might be different in filament geometry).

It is difficult to apply the standard formula (2.6) to our numerical results because the background medium rapidly becomes strongly perturbed. The gas motions are

not uncorrelated with the sink velocity, as assumed in the development leading to equation (2.6), but instead tend to be *focused* toward mass concentrations. The local gas density distribution is also highly perturbed, with strong, gravitationally-accelerated flows into and along filaments. Bonnell *et al.* (2001b) attempted to deal with these difficulties through the following argument. Consider a point mass at radius R in some environment, with infall velocities

$$v_{rel} \propto R^{-\eta} \tag{2.10}$$

and gas densities

$$\rho \propto R^{-\xi} \,. \tag{2.11}$$

With these assumptions Bonnell *et al.* found

$$\dot{M} \propto g(t) M^2 R^{3\eta-\xi} \,, \tag{2.12}$$

where $g(t)$ is a function which allows for the assumed homologous evolution of the cluster. This analysis results in $\Gamma \rightarrow 1$ for sinks whose masses are initially uncorrelated with position; Bonnell *et al.* (2001b) suggested that the slope might be steeper if the higher-mass objects reside preferentially in the cluster center.

To see whether the densities and velocities correlate with sink mass, we evaluate these quantities at two radii: first, at a radius of $2GM/c_s^2$, the maximum accretion radius in the Bondi accretion formulation in the case where the relative velocity between the sink and the gas is subsonic; the other at a radius of 0.024 pc, which is the distance sound waves can travel in 0.1 Myr (the time between snapshots). Figure 2.11 shows scatter plots of sink masses vs. velocities relative to the gas, gas density, surface density and surface density divided by v, with all properties evaluated at R=$2GM/c_s^2$ at t=0.6Myr. Figure 2.12 shows the same plots, with gas properties evaluated at 0.024pc away from the sink. The results show that the densities and velocities of the gas are not strongly correlated with the individual sink masses. Therefore, the accretion rate scales as $\dot{M} \propto M^2$. This may be a result of having

a group of accreting sinks experiencing the same environment, as in the discussion leading to equation 2.12; whatever sets the local density and flow velocity, the capture cross-section will still scale as M^2.

This suggests that the important factor is not the form of the initial density and velocity distribution but whether the *global* features are uncorrelated with the *individual* sink masses, as in equation (2.12). In this view as long as a group of objects of differing mass "see" the same conditions- gas densities and velocities - their *differential* accretion rates will scale as M^2 (the proportionality due to the gravitational cross-section). This only holds for the most massive objects in each group; the low-mass sinks are starved of material to accrete. More generally, the absolute value of the mass accretion rate may vary from group to group; but as long as each group can set up an $\dot{M} \propto M^2$ relative accretion rate with differing constants of proportionality, one may argue that the summed population will still asymptotically evolve towards $\Gamma = 1$.

2.4.3 Turbulence

Most simulations of star-forming clouds invoke an imposed turbulent velocity field, in view of the supersonic spectral line widths observed in molecular tracers. Our simplified approach, in which we do not impose initial velocity fluctuations but initial density perturbations, is motivated by recent simulations which form turbulent star-forming clouds from large-scale flows Heitsch et al. (2006); Heitsch & Hartmann (2008); Heitsch et al. (2008b) and Vázquez-Semadeni et al. (2006, 2007). These simulations found that while hydrodynamically-generated turbulence in the post-shock gas dominates the cloud structure and motions in early phases, gravitational acceleration dominates the motions at late stages (e.g., Heitsch et al. 2008a). Similar behavior is seen in models in which the turbulence is not continually driven but allowed to decay (e.g., Bate et al. 2003). Thus, the initial turbulence provides density fluctuations or "seeds" which then generate supersonic motions as a result of gravitational forces in clouds with many thermal Jeans masses. Our models take this view to a simple extreme, where we let gravity do all of the (supersonic) acceleration of the gas given

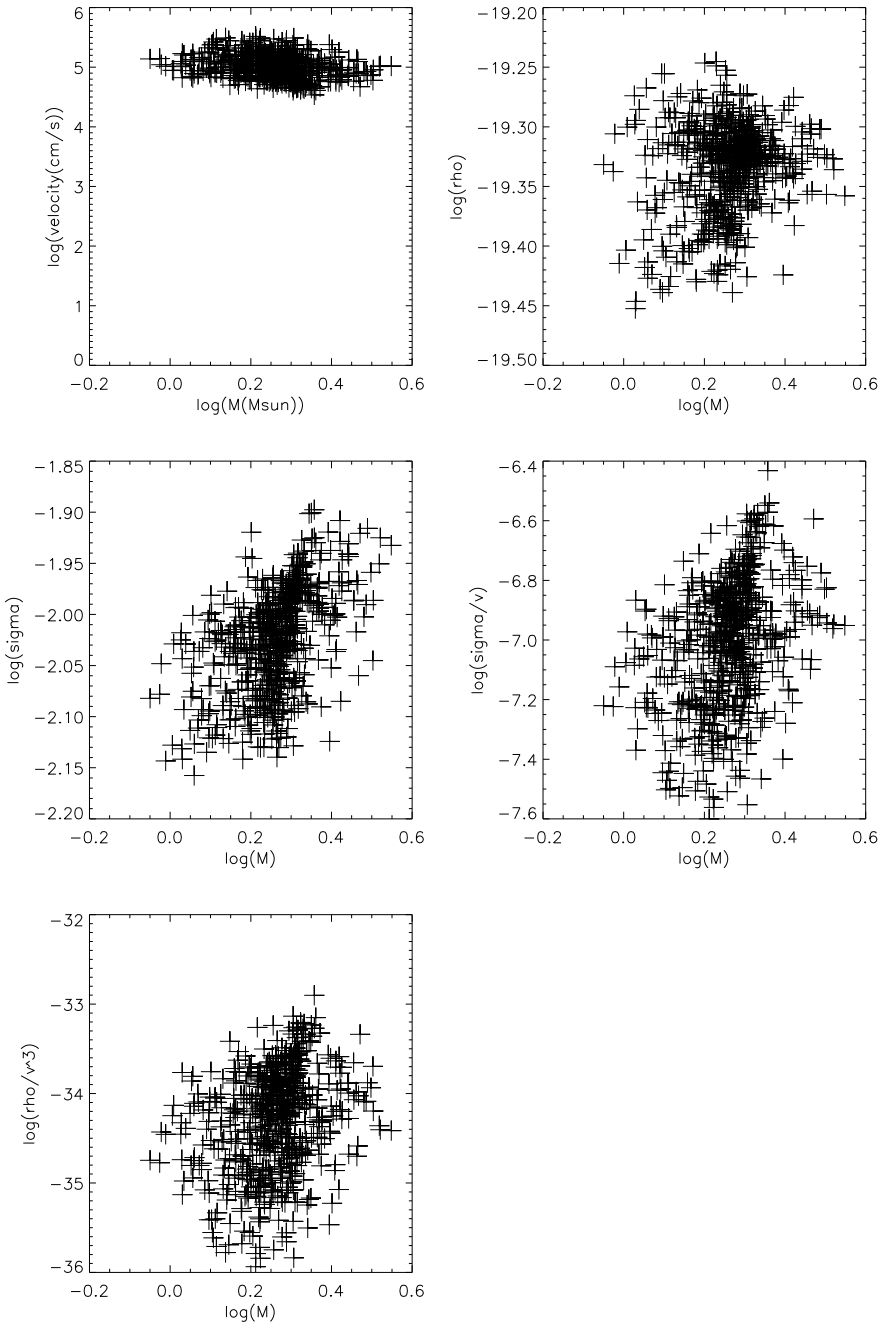

Figure 2.11: Mass of sinks vs. the gas properties around the sinks for all the cases in the equal initial mass, uniform density case at t = 0.6Myr. The gas properties are evaluated at $R_{acc} = 2GM/c_s^2$ from each sink. Top left: mass vs. gas velocity relative to the sink, top right: mass vs. gas density, middle left: mass vs. surface density, middle right: mass vs. surface density/velocity, bottom left: mass vs. ρ/v^3. There is no obvious correlation between the gas properties and the sink mass.

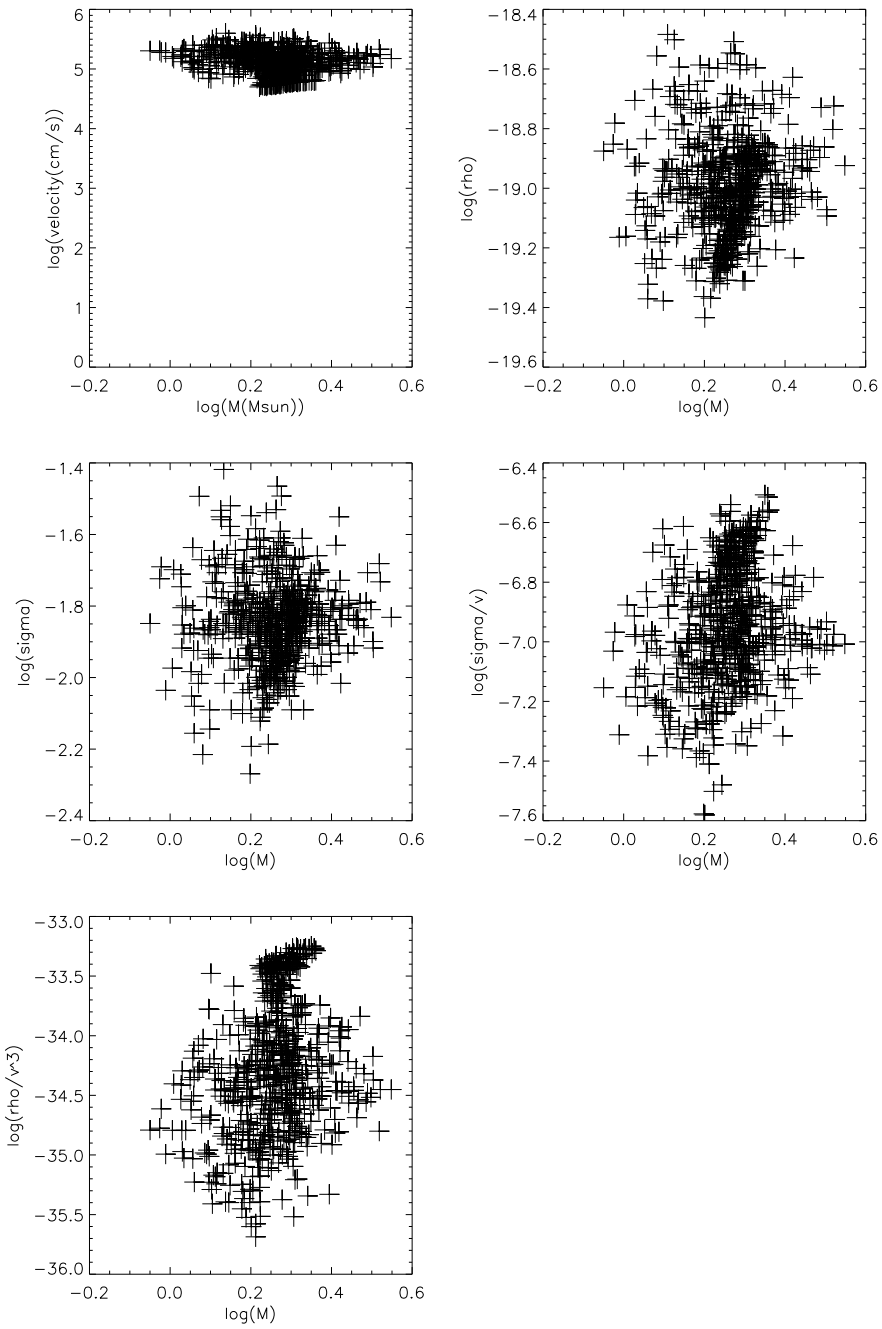

Figure 2.12: Mass of sinks vs. the gas properties around the sinks for all the cases in the equal initial mass, uniform density case at t = 0.6Myr. The gas properties are evaluated at $R = c_s \times 0.1 Myr = 0.024$ pc from each sink. Top left: mass vs. gas velocity relative to the sink, top right: mass vs. gas density, middle left: mass vs. surface density, middle right: mass vs. surface density/velocity, bottom left: mass vs. ρ/v^3. There is no obvious correlation between the gas properties and the sink mass.

initial density fluctuations (our clumps).

The assumption that the largest "turbulent" motions are mostly gravitationally-driven is an essential part of the competitive accretion picture. Krumholz et al. (2005) argued that the supersonic velocity dispersions of molecular clouds are too large for Bondi (and thus competitive) accretion to be effective; however, this assumes that the "turbulent" motions persist and are spatially uncorrelated with the accreting masses. In contrast, even though large (and roughly virial) velocities develop in our simulations, competitive accretion still operates because the motions are largely the result of gravitational infall to groups, plus global, spatially-correlated collapse of both the sheet gas and the sinks. These considerations emphasize the importance of understanding the nature of "turbulence" in star-forming clouds.

2.4.4 Mass functions

Recently, there have been suggestions that the stellar IMF is not universal; in particular, that the most massive star in a region depends upon its richness ((Kroupa & Weidner, 2003, 2005); also Weidner, Kroupa, & Bonnell 2010 and references therein). The models presented here also result in a non-universal upper-mass IMF, with a suggestion that $\Gamma \sim 1$ is an asymptotic limit which is approached most closely when the matter accreted is much larger than the initial "seed" mass; and thus, to some extent, the slope may correlate with the most massive object formed. This is difficult to ascertain observationally, in part because of the tradeoff between upper mass slope and truncation mass (e.g., Maschberger & Kroupa 2009). Using the simulations of Bonnell et al. (2003) and Bonnell, Clark, & Bate (2008), Maschberger *et al.* (2010) found global values of Γ slightly greater than unity, and $\Gamma \sim 0.8$ in the richest sub-clusters. This may be consistent with our findings of a correlation between slope and upper mass.

It may be worth noting two other situations in which $\Gamma \sim 1$ mass functions are found: dark-matter halo simulations (below the upper-mass cutoff; e.g., Jenkins *et al.* 2001); and star cluster mass distributions (Elmegreen & Efremov, 1997; McKee & Williams, 1997; Zhang & Fall, 1999; Chandar, 2009; Chandar et al., 2010), although

some estimates yield flatter power-law slopes (e.g., Maschberger & Kroupa 2009). Gravitational accretion thus could potentially provide a unified explanation of the similarities in these mass functions.

2.5 Conclusions

In this chapter, we present numerical experiments using SPH simulations to address the general applicability of competitive accretion in initially non-clustered environments. A flat geometry is used to construct a shallow gravitational potential as opposed to the spherical clustered potential used in previous simulations by Bonnell *et al.* (2001a,b). The simplified setup consists of only the most important elements in forming the high-mass IMF: differential gas accretion onto protostars under gravity. With this setup, we were able to produce the high-mass end of the IMF with slopes comparable to the Salpeter slope $\Gamma = 1.35$. The simple setup also allows us to understand the mass growth of sinks in details without worrying about fragmentation and thermal physics, and also permits us to generate reasonably statistically-significant results for upper mass function slopes.

The mass growth rate of the sinks follows $\dot{M} \propto M^2$ for all high mass sinks, while low mass sinks sometimes accrete at lower rates. The high-mass end of the IMF develops a power-law tail and flattens, with an asymptotic slope of $\Gamma = 1$. Variations in initial clumps masses and surface density help the power-law tail to flatten faster. In our simulations, most systems do not reach the asymptotic slope due to gas depletion. In real molecular clouds, stellar feedback as well as gas depletion can terminate the accretion and determine the final high-mass IMF slope.

The present set of simulations are obviously quite idealized. Our purpose was to elucidate the basic physics of CA in as easily-visualized and interpretable a situation as possible. The next steps, which are currently under way, are to start with more complex density distributions and allow sink formation and consequent evolution in more complex geometries, and include velocity fields as necessary. While we suspect that the physics of competitive accretion will remain the most important factor in creating the high-mass region of the IMF, as previously argued by Bonnell *et al.*

(2001a,b, 2003), and Clark *et al.* (2009), further study is needed.

CHAPTER 3

The Low-mass Stellar Population in L1641

3.1 Introduction

Do the most massive stars form preferentially in dense, massive environments? Answering this question has proved to be frustratingly difficult. The recent review by Bastian et al. (2010) concludes that there is no clear evidence for nonstandard stellar initial mass functions (IMFs) in specific environments, though this issue "clearly warrant(s) further study". One problem is that most of the studies of IMFs in relatively unevolved young regions have been conducted on young star clusters (Bastian et al. 2010; Weidner et al. 2010, and references therein), because it is much more difficult to study low-density, dispersed regions. Perhaps the most extensive survey to date on star formation in low-density environments is that of Luhman et al. (2009), which argued that samples of roughly 150 and 300 members of Taurus (depending upon the region surveyed) showed an anomalous IMF, particularly in suggesting a peak near spectral types K7-M0 not observed in other regions. However, the low-mass population of Taurus is insufficiently numerous to make a strong test of the high-mass end of the IMF.

The lower part of the Orion A molecular cloud, south of the Orion Nebula Cluster (ONC) region, appears to be one site where a significant test of the dependence of the upper mass distribution in a lower-density environment can be carried out. For simplicity we call this region "L1641", though this is a broader use of the original Lynds cloud designation (as discussed further in Section 3.4.2, also see Allen & Davis (2008) for a discussion of the individual clouds). As the lower part of the Orion A cloud is contiguous with the ONC region, it can be assumed that L1641 is at roughly

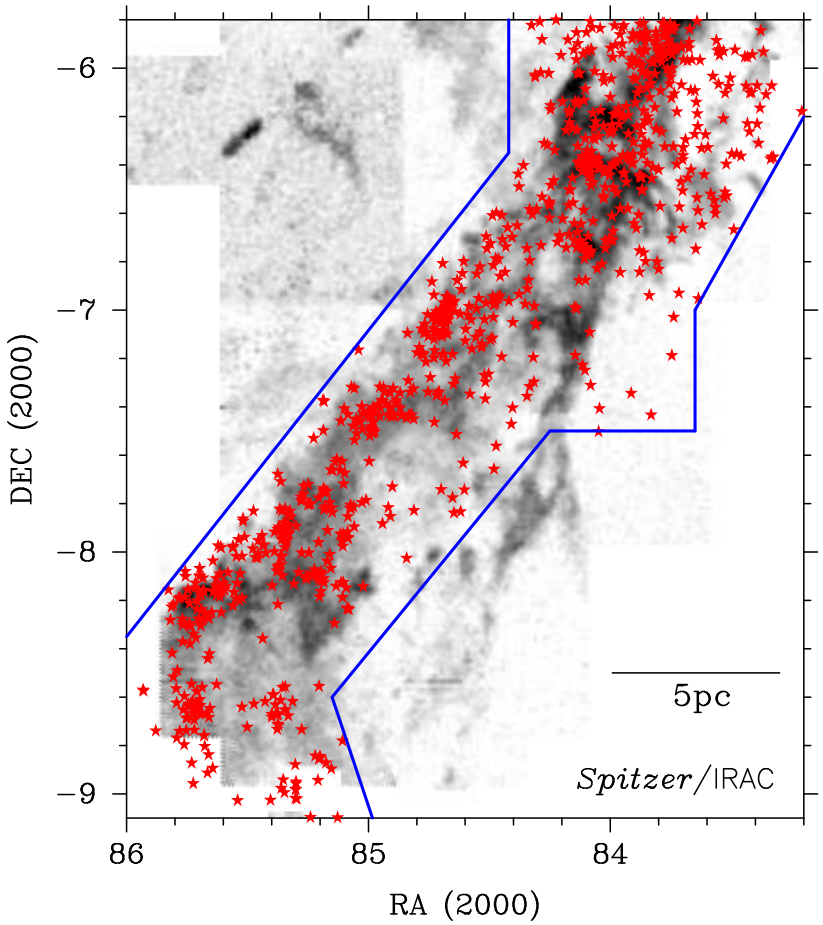

Figure 3.1: Blue boundary lines represent the fields covered by the *Spitzer*/IRAC survey of Orion (Megeath et al., 2012) and the red stars show IR-excess objects identified by this survey, which are overlaid on ^{13}CO map from Bally et al. (1987). The physical scale of 5 pc is also shown in the plot, assuming a distance of 414 pc.

the same distance as the ONC ($\sim$ 414 pc; Menten et al. 2007; Kim et al. 2008), allowing the stellar populations of the two regions to be compared directly. Based on previous surveys, as well as the recent *Spitzer/IRAC* survey of infrared-excess stars (see Figure 3.1 for locations of the IR excess objects, data to be published in Megeath *et al.* 2012), it appears that L1641 contains a much larger pre-main sequence population than other nearby low-density regions such as Taurus-Auriga (see, e.g Luhman et al. 2009; Rebull et al. 2011).

The star of earliest spectral type spatially associated with the molecular gas south of -6.1° declination is B4 (Racine, 1968), with only an additional 12 late B stars

projected on the cloud according to current surveys (Skiff, 2010). The ONC, on the other hand, has two O stars and seven stars with spectral types earlier than B4, and its IMF is consistent with a Salpeter upper-mass slope (Muench et al., 2002; Da Rio et al., 2009). The question to be addressed is whether this apparent deficit of high-mass stars in L1641 is the result of its being a relatively low-density environment, in contrast to the densely clustered ONC, or whether L1641 simply does not have enough members in comparison with the ONC (with $\sim$ 2000 members; Hillenbrand & Hartmann 1998, Muench et al. 2002, Da Rio et al. 2009, Robberto et al. 2010) that high mass stars are probable, assuming a universal IMF.

In this chapter, we present optical V and I band photometry and low resolution optical spectroscopy of low mass stars in L1641. We estimate that there are about 1600 low-mass members in the region, assuming that the disk fraction is constant throughout the cloud. Furthermore, we show that the average age of the stars in our sample is only slightly greater than that of the ONC region. Thus, our findings support the idea that the comparison between L1641 and the ONC ultimately will provide a good test of the possible environmental dependence of the upper mass IMF. For this chapter, we consider O & B stars found in the literature and assume that there are no deeply embedded early B stars that we do not already know. Under this assumption, we then make comparisons with standard forms of the IMF which indicate that L1641 is deficient in early B and O stars, based on the known low-mass population. In Chapter 4, we will discuss our search for high-mass members and add intermediate-mass members verified by spectroscopy, which are currently missing from our sample. In Section 3.2 we describe our observational program and the procedures used to reduce the data. In Section 3.3 we present an analysis of our photometric and spectroscopic results. Then in Section 3.4, we summarize our knowledge of the low-mass population, briefly relate our results to the known population of early-type stars, consider some uncertainties related to deciding where to divide the region between low- and high-density areas, and make some preliminary tests using standard models of the IMF. Finally, we present our conclusions in Section 3.5

3.2 Observations and Data Reduction

3.2.1 Optical Photometry

We obtained V and I band optical photometry with the Ohio State Multi-Object Spectrograph (OSMOS) on the MDM 2.4m Hiltner telescope (Stoll et al., 2010; Martini et al., 2011). The detector has a 18.5′ x 18.5′ field of view, vignetted by a 20′ diameter circle. We used 2 x 2 binning, which gives a plate scale of 0.55″ per pixel. The majority of L1641 from -6° to -9.2° was covered with 41 fields (see Figure 3.2). The exposure sequence consists of one short exposure (5 seconds) and two long exposures (60 seconds) in both V and I bands. The photometry was obtained on the nights of Dec 7 - Dec 8 and Dec 8 - Dec 9, 2010. Most fields were observed with the exposure sequence once on each night, but a few fields were only observed on one night. The conditions were not completely photometric, with some visible cirrus at the beginning of each night, and the seeing ranged from 1.1″ to 1.8″ FWHM. However, we started observing L1641 three to four hours after twilight ended and most of the cirrus had disappeared by then. We observed two Landolt standard fields every two hours throughout the night for photometric calibration. SA92, SA95, SA98 and SA101 were used according to the time of the night.

Each CCD frame was first corrected by overscan using the IDL program proc4k written by Jason Eastman. Note that the original program is written for the Ohio State 4k CCD imager alone, and has been modified to process OSMOS data. We then performed the basic reduction following the standard procedure using IRAF. Note that we used sky flats in the flat-field correction. We determined the astrometric solution with *imwcs* in *WCSTools*, using the coordinates of stars from the 2MASS catalog. The astrometric solutions are in general good within one pixel, or 0.55″. We then obtained aperture photometry with the IRAF *phot* package, using an aperture of 8, or $\sim$ 3-4 times the FWHM. We used the Landolt fields for photometric calibrations. The rms departures of the standard stars from the calibration equations are $\sim$ 0.05 mag for both V and I bands. The MDM 4k imager used by OSMOS has a known issue of crosstalk between the four CCD segments. When a CCD pixel is saturated,

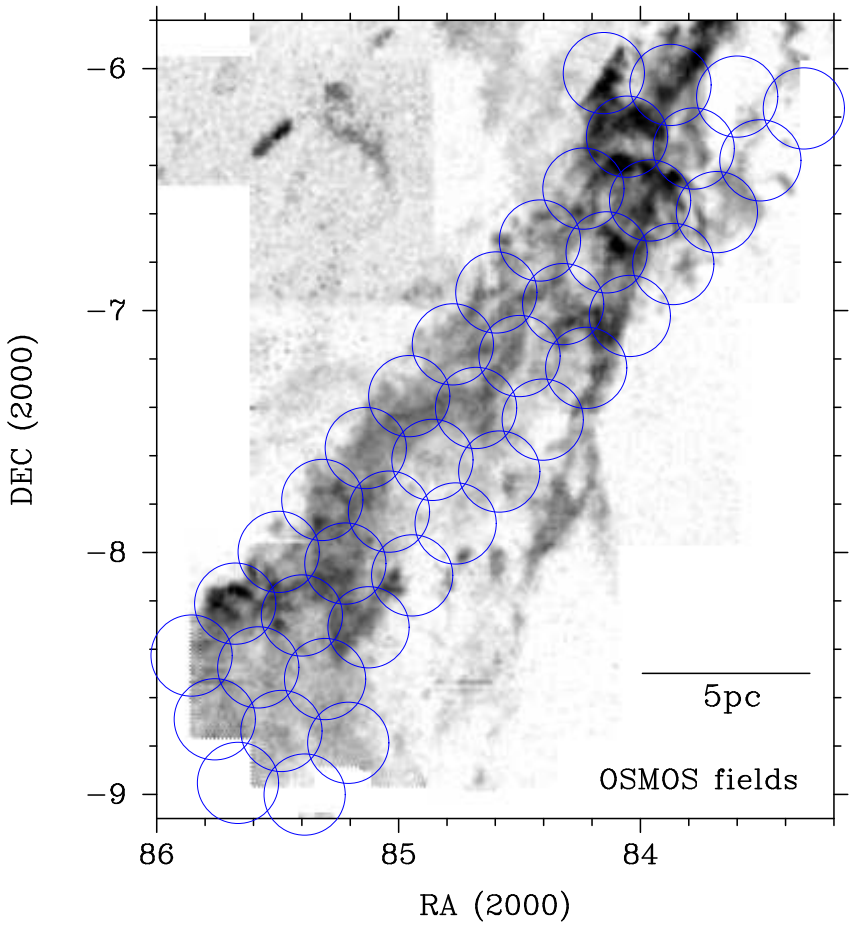

Figure 3.2: OSMOS optical photometry fields (blue circles) overlaid on ^{13}CO map (Bally et al., 1987). The physical scale of 5 pc is also shown in the plot, assuming a distance of 414 pc.

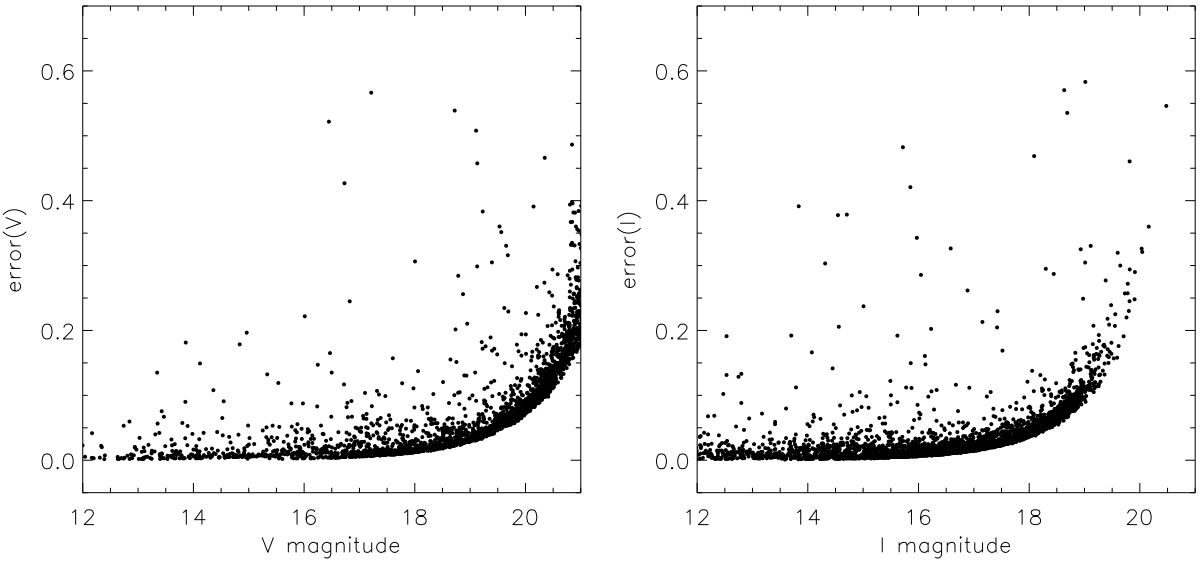

Figure 3.3: Errors in V (left) and I (right) band photometry. The errors shown here are the greater of the IRAF calculated error and the median absolute deviation.

it creates spurious point-sources in corresponding pixels on all other three segments. Therefore, instead of finding point sources in the images with *daofind*-like packages, we used the positions of all 2MASS point sources for our photometry. Non-detections and saturated stars in either bands are removed. If a star is saturated in the long exposure but not in the short exposure, the short exposure is used for the photometry. Measurements that are affected by bleeding or crosstalk from a saturated star are manually removed. Finally, we combine all the photometry measurements for the same star by taking the median value.

To estimate the photometric error, we use both the error estimated by the IRAF *phot* and the variation in separate observations of the same star. The IRAF *phot* package only takes into account of Poisson statistics which tends to underestimate the true uncertainty. To provide a better estimate of our errors, we take the stars that we have at least four long-exposure measurements to find the median absolute deviation (MAD), a robust measure of the deviation. Since most fields are observed on both nights and the measurements from both nights are used, the deviation implicitly takes into account of the potential effects due to variable atmospheric extinction and

seeing from one night to another. If a star is saturated in the long exposures, then the short-exposure measurements (in the case where there are more than two short exposures) are used. We estimate the photometric error for each star from the greater of the *phot* calculated error and the MAD. The results are shown in Figure 3.3. The typical errors are less than 0.05 magnitude for stars brighter than V = 19 or I = 18. This error is comparable to the errors obtained in the calibration of Landolt stars and is most likely due to the non-photometric weather conditions. The typical error then increases drastically with fainter stars due to uncertainties in photon statistics. A small fraction of stars have errors much larger than the typical errors, which can be due to non-photometric conditions (cirrus in the beginning of the night) as well as intrinsic variability of the stars from one night to another. We think intrinsic variability contributes to the measured errors because we examined the list of stars with the largest errors and many of them turned out to be known variable stars.

We were able to obtain photometry of stars with V and I magnitude between 12 and 22 mags. However, from Figure 3.3, we know that the typical error of a V = 21 mag star is about 0.2 mag and the error increases rapidly for fainter objects. We therefore limit our photometric sample to stars with V magnitudes between 12.5 and 21, I magnitudes between 12 and 20.5 and V-I between 0.5 and 4 mags. with the typical error of a 21 magnitude star being 0.2 mags.

Figure 3.4 shows the V vs. V-I color-magnitude diagram of the sample mentioned above. The top panel shows all the stars in our sample, regardless of its IR-excess and the bottom panel shows the same plot, with the class I protostars shown in blue diamonds and the class II's (IR excess objects with disks) shown in red circles.

We note that most of the class II stars in Figure 3.4 fall in a small region on the CMD, which we approximate with the top two parallel lines. The bottom of the YSO region is traced by a line through the two points (V-I, V) = (0.5, 11.5) and (4, 21.5), and the top is 2 magnitudes above it in V at a given V-I. We expect that the Class III's (pre-main sequence objects with no IR excess) have similar ages and distances and therefore fall in the same region of the CMD. However, not all the non-IR excess objects in this region are members. We therefore target them in our

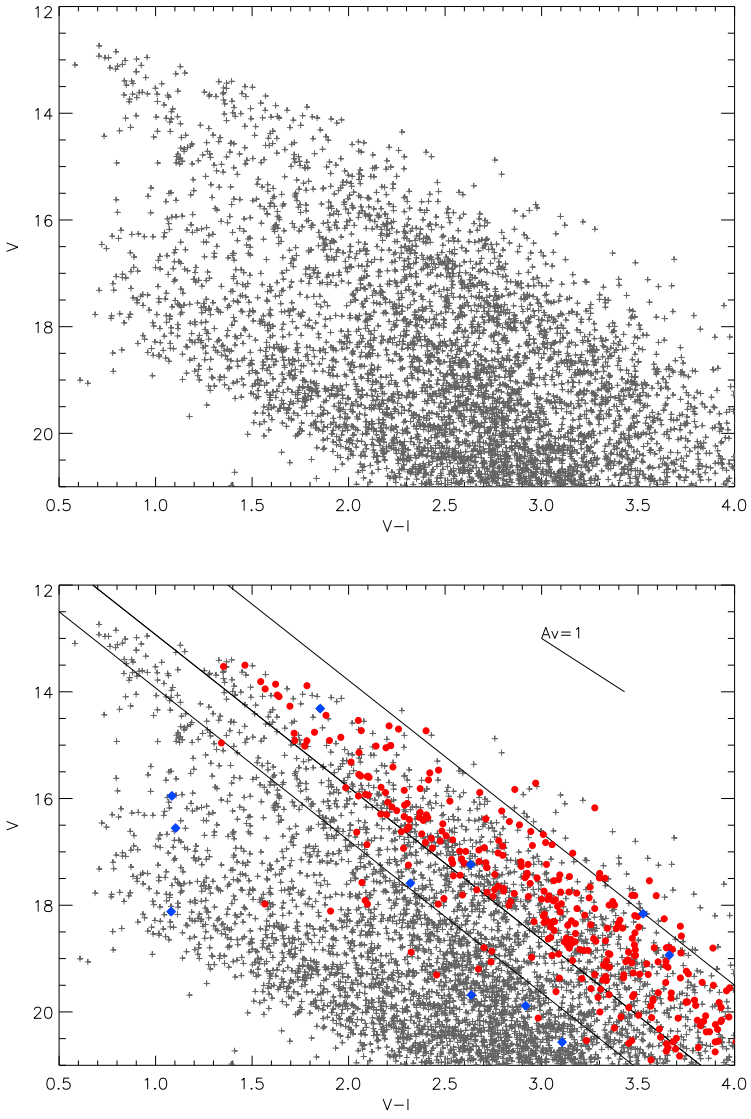

Figure 3.4: Top: V vs. V-I color-magnitude diagram of objects in L1641, showing all the photometric data. Bottom: Same figure, with protostars (blue diamonds) and disk objects (red circles) overplotted. The YSOs with disks (red circles) lie mostly in a small region of the CMD, marking the region populated by the pre-main sequence stars. There are 772 non-IR excess sources (grey crosses) in the same region of the CMD. This photometry was taken in Dec 2010 with OSMOS on the MDM 2.4m telescope. The extinction vector is the standard extinction taken from Cardelli et al. (1989) with $R_V = 3.1$. The parallel lines are discussed in Section 3.4.1.

optical spectroscopy surveys to confirm their membership.

3.2.2 Optical Spectra

There are two parts to our optical spectroscopic sample. The first part is the sample of infrared-excess stars from the *Spitzer* survey of Megeath *et al.* (2012). Figure 3.1 shows fields covered by the *Spitzer* survey and the positions of the IR-excess stars. The *Spitzer* survey identified 166 protostars and 723 disk objects in L1641 (defined as the field outlined in Figure 3.1 but stops at -6°.) Note that only 8% of the protostars and 48% of the disk objects are found in our optical photometric sample and are therefore sufficiently bright for optical spectroscopy. The second part of our sample is non-IR excess objects selected based on their optical photometry. There are a total of 772 non-excess stars that satisfy the optical photometry selection and we were able to target 95% of these objects in our spectroscopy. The sample is, however, biased against heavily-reddened objects.

The spectra were obtained with multi-aperture spectrographs covering extended fields of view. Approximately 75% of our spectra were obtained with Hectospec, the fiber-fed multiobject spectrograph on the 6.5m MMT on Mt. Hopkins (Fabricant et al., 2005). It has 300 fibers that can be placed within a 1° diameter field. Each Hectospec fiber subtends 1.5″ on the sky. The observations were taken with 270 line mm^{-1} grating, providing $\sim$ 6.2Å resolution and spectral coverage of 3650 to 9200Å. With 17 observations from 2006 to 2011, a total of 2369 stars were observed. The total on-target exposure times are 45 to 50 minutes for most fields, with the exception that the Jan 30, 2009 field was observed for 22.5 minutes. The top panel of Figure 3.5 shows fields of the Hectospec observations. Targets for observing runs from 2006 to 2009 are selected based on their IR colors (fields shown in blue) and the targets of the 2011 run are selected based on their optical photometry (fields shown in magenta, see Section 3.2.1 for selection criteria). We first maximized the number of targets that satisfy either the IR excess or optical selection criteria, and then filled in the remaining fiber positions with other stars in the field.

The Hectospec data were reduced through the standard Hectospec data reduction

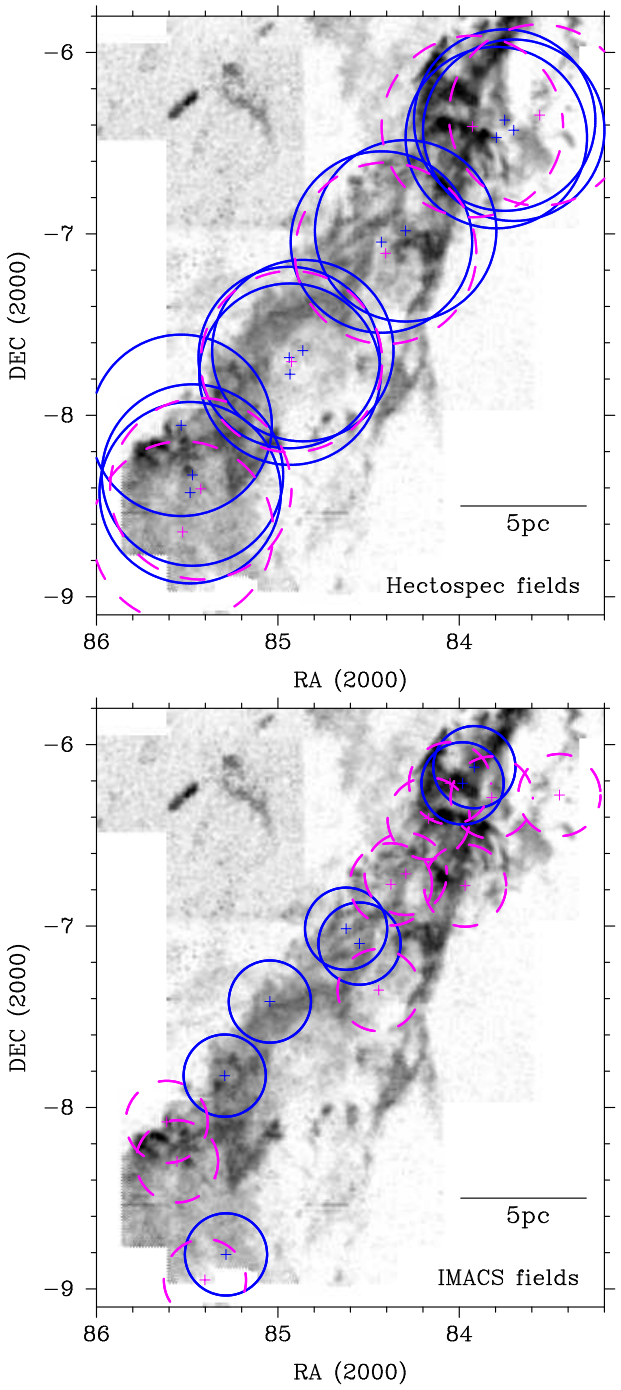

Figure 3.5: Optical spectroscopy fields overlaid on ^{13}CO map from Bally et al. (1987). The Hectospec fields (top) are chosen to maximize number of IR excess objects observed. The IMACS fields (bottom) sample are either IR-selected (blue solid circles) or optical-selected (magenta dashed circles). The IMACS fields are mainly used to compliment the Hectospec fields in crowded regions. The physical scale of 5 pc is also shown in the plot, assuming a distance of 414 pc.

pipeline (Mink et al., 2007), except for sky background subtraction. The pipeline assumes that the sky background does not vary significantly with position on the sky and uses "sky fibers", or fibers that point to empty portions of the sky, to correct for the sky background. However, in a star-forming region, nebulosity may result in significantly varying sky background and therefore bad estimates of nebular lines. Our sky subtraction takes into account the spatial variations of the sky background. Some of the observations were taken along with offset sky spectra, 5″ apart from the star, in which case we subtracted the offset sky spectra from the science target spectra. When the offset sky spectra were not taken, we used the closest 3 to 5 sky fibers as the average sky and subtract it from the science spectra. We tested our sky subtraction methods with sky fibers (so a perfect sky subtraction would leave a spectrum with only noises around 0) and found that the quality of the resulting spectra is significantly improved with the offset sky spectra, with most of the Hα emission and other sky lines accounted for whereas the nearest 3 - 5 sky fibers improves the overall sky subtraction (especially night-sky emission lines in the near-IR) but does not correct for the nebular lines very well.

Another 25% of our spectra were obtained with IMACS, the Inamori-Magellan Areal Camera & Spectrograph on the Magellan Baade telescope (Bigelow & Dressler, 2003). We used IMACS f/2 camera in multi-slit spectroscopy mode with the 300 line grism at a blaze angle of 17.5°. With a 0.6″ slit, this configuration yields a resolution of 4Å and spectral coverage of approximately 4000 to 9000Å (stars close to the edge of the fields may not have full spectral coverage). From 17 observations in 2010 and 2011, a total of 715 stars were observed. The standard observation time for each field is 5 x 10 minutes, but we increased the time to 6 x 10 minutes for a few observations at higher airmasses. The bottom panel of Figure 3.5 shows the fields of the IMACS observations. The targets of the first IMACS run were selected based on their IR colors (shown in blue), and the targets of the second run are selected based on their optical photometry (shown in magenta, see Section 3.2.1 for selection criteria). The IMACS data were reduced with COSMOS, the Carnegie Observatories System for MultiObject Spectroscopy, following the standard cookbook.

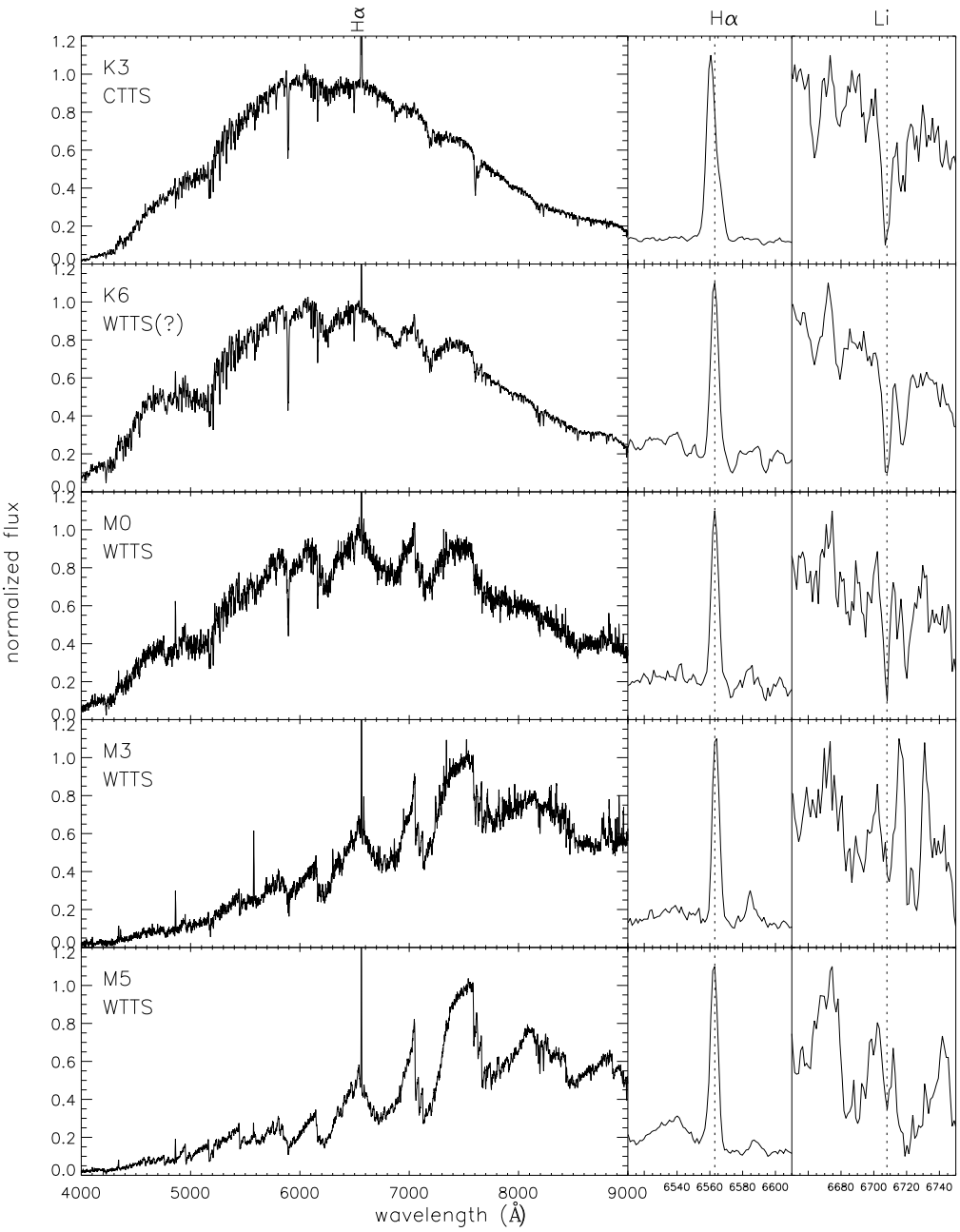

Figure 3.6: Examples of Hectospec spectra with a zoom-in view around Hα (λ 6563) and Li I (λ 6707). From top to bottom, the spectra are spectral typed: K3, K6, M0, M3 and M5. The [O *I*] line at 5577Å is a prominent sky line. The red end of the M type spectra are affected by series of sky lines. Their TTS type are classified using the definition given by White & Basri (2003). The Hα equivalent width in the K6 star is bordering the cutoff in the definition.

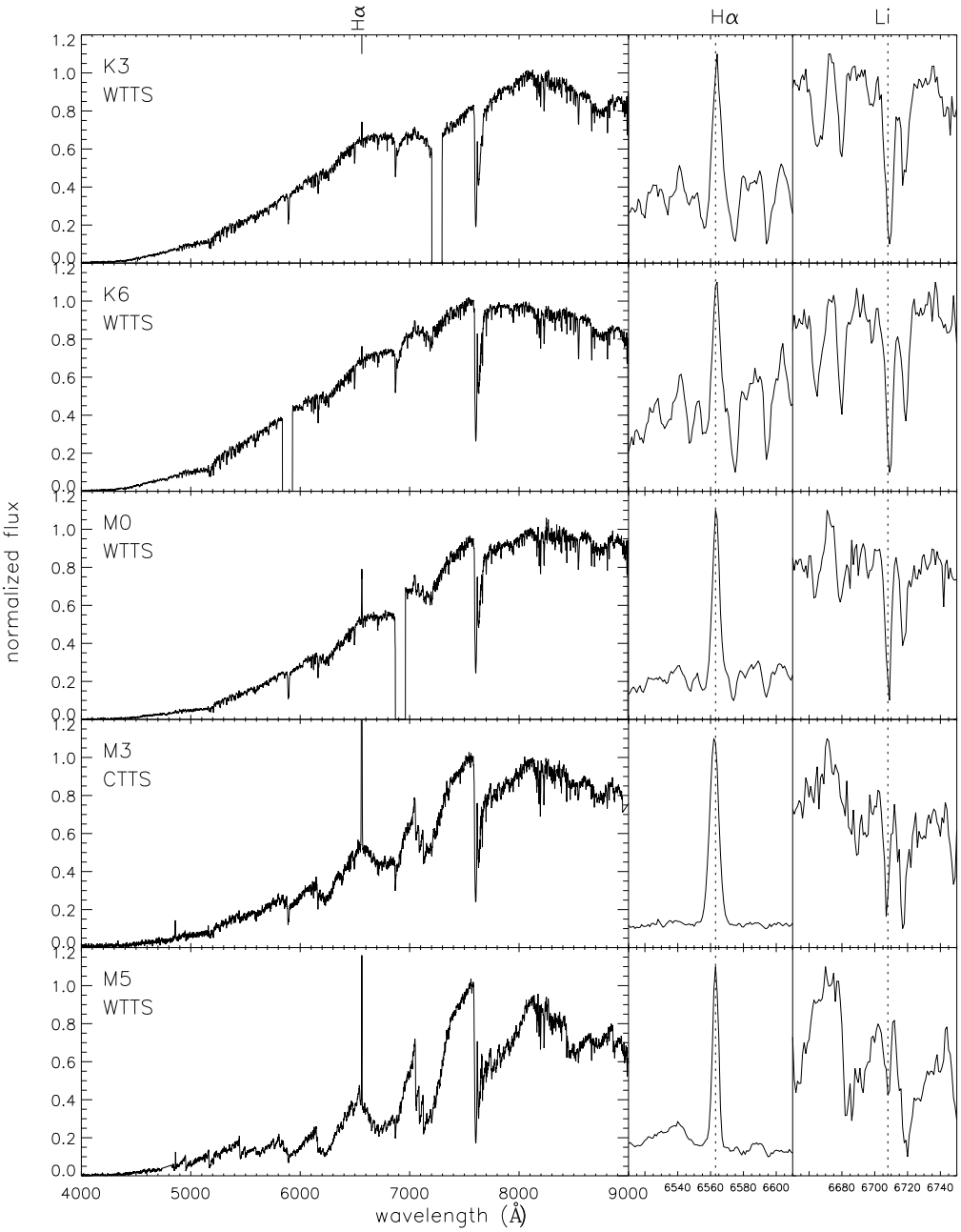

Figure 3.7: Examples of IMACS spectra with a zoom-in view around Hα (λ 6563) and Li I (λ 6707). From top to bottom, the spectra are spectral typed: K3, K6, M0, M3 and M5.

Under good observing conditions, we were able to spectral-type stars as faint as V $\sim$ 21. However, the faintest magnitude we can spectral type depends on the seeing and the instrument used.

3.3 Results

3.3.1 Photometry

Figure 3.4 shows the V vs. $V-I$ color-magnitude diagram of the stars between $V-I \sim 0.5-4$ and $V < 21$. There are a total of 4475 stars in this photometric sample. Correlating the optical photometry and the IR-excess classification (Gutermuth et al., 2009), we mark the IR-excess objects in our photometry (bottom panel). 13 of the stars were protostars (blue diamonds) and 347 of them were YSOs with disks (red circles). Compared to the number of IR-excess objects identified in the *Spitzer* survey, only 8% of the protostars and 48% of the disk objects are found in our photometric sample. The optical photometry fields cover slightly less area than the *Spitzer* survey, but cover the 95% of the IR-excess objects. It is not surprising that we do not find most of the protostars as they are highly embedded in their envelopes. We were only able to identify half of the stars with disk excesses in the optical photometry due to extinction (see Section 3.3.4).

3.3.2 Spectra and Spectral Types

Figure 3.6 and 3.7 show some example spectra of confirmed members from Hectospec and IMACS, respectively, arranged by their spectral types. The Hα equivalent width criteria by White & Basri (2003) is used to determine whether they are classical T Tauri stars (CTTS) or weakline T Tauri stars (WTTS). Note that IMACS has very little transmission in the blue whereas the transmission of Hectospec is more uniform across the spectral range. The [O I] line at 5577Å is very prominent in some Hectospec data but is actually a sky line that was not correctly subtracted. In this case, the Hα emission is also likely affected by bad sky subtraction. Figure 3.8 show IMACS spectra of rapidly- accreting stars. They not only have a high Hα equivalent width, but also have other emission lines such as [O I], He I and the infrared Ca triplet. The

last two spectra have particularly high Hα equivalent widths and show O I emission at 7773Å and the higher orders of the Paschen series.

We determine the spectral types of our Hectospec and IMACS data with SPTCLASS, a semi-automatic spectral-typing program (Hernández et al., 2004). It uses empirical relations of spectral type and equivalent widths to classify stars. It has three schemes optimized for different mass ranges (K5 or later, late F to early K and F5 or earlier), which use different sets of lines. The user has to manually choose the best scheme for each star based on the prominent features in the spectrum and the consistency of several indicators. While SPTCLASS is insensitive to reddening and S/N of the spectra (as long as one can obtain a good flux estimate), it does not take into account the effect of the hot continuum emission produced by the accretion shocks. This continuum emission makes the photospheric absorption lines appear weaker. SPTCLASS generally assigns an earlier spectral type to veiled stars than their and therefore the SPTCLASS outputs should be considered as the earliest spectral type limits. Highly veiled stars (such as the ones shown in Figure 3.8) are not spectral-typed. Eight of our program stars are too veiled for spectral-typing.

We also complement our results with data from Fang et al. (2009, hereafter F09), which include spectral type estimates and Hα and Li I equivalent widths for 266 stars. The majority of the spectral types come from their VLT/VIMOS observations and some are from Gâlfalk & Olofsson (2008) and Allen (1995). We observed 206 of the stars in the F09 sample; Figure 3.9 compares our spectral types with theirs. Since the spectral types in F09 come from multiple sources, we use different symbols to indicate the source. Most of the spectral type are consistent within 2 subclasses and there is no systematic trend in the differences; the only major large inconsistency is for a rapidly-accreting G type star, which has an uncertain spectral type because of very high veiling. For consistency we therefore use the spectral type from our observations for the objects in common, and incorporate the data from F09 for the stars we did not observe.

Figure 3.10 shows the distribution of spectral types of confirmed members. The distribution peaks around M4; we are systematically incomplete in the later-type

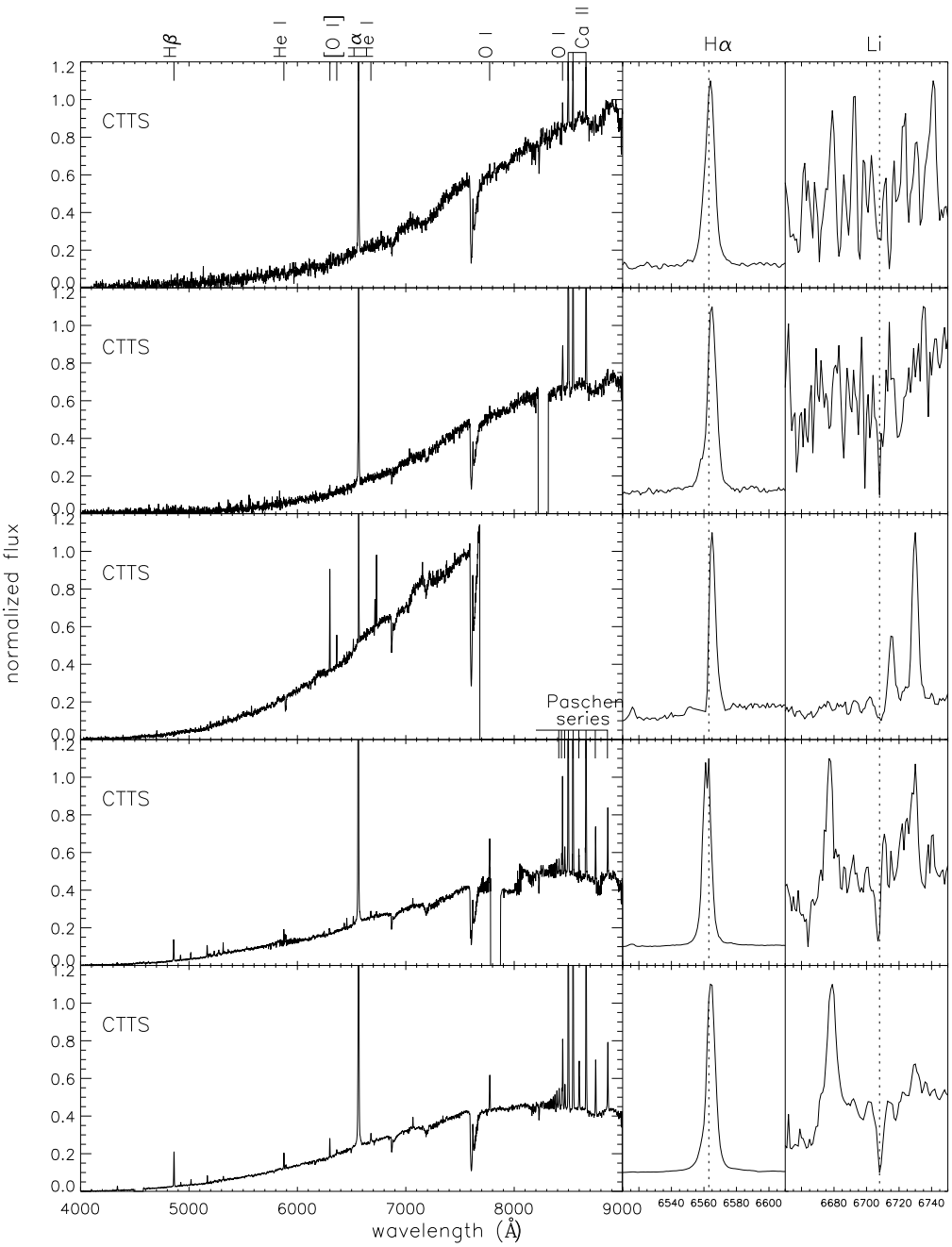

Figure 3.8: Examples of IMACS spectra of rapid accretors with a zoom-in view around Hα (λ 6563) and Li I (λ 6707). The spectra are highly-veiled and therefore makes spectral typing difficult. The main emission lines have been marked.

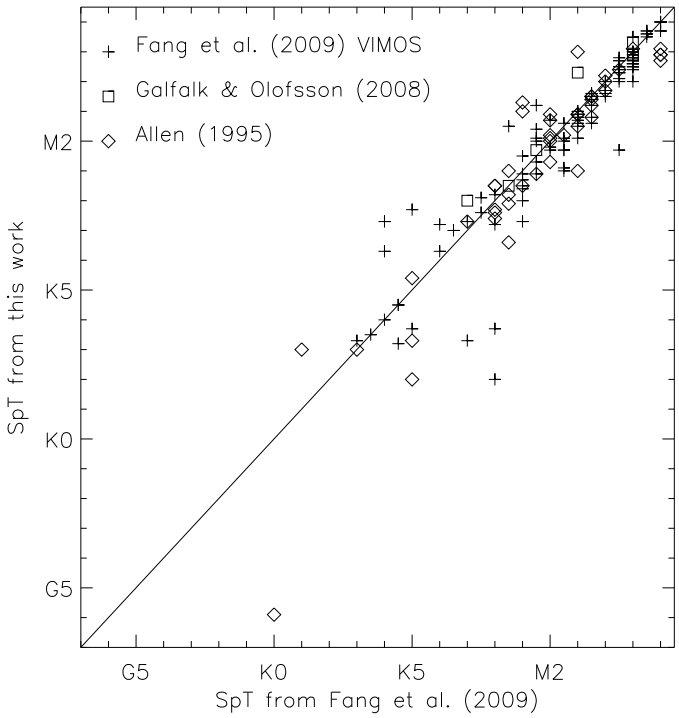

Figure 3.9: Comparison of the spectral types obtained by Fang et al. (2009) and this work for the 166 objects that are included in both samples. The catalog of Fang et al. (2009) comes from three sources: 1. their VLT/VIMOS observations (crosses) , 2. Galfalk&Olofsson(2008) (squares) and 3. Allen (1995) (diamonds). The highly discrepant star near the bottom is heavily veiled (see text)

population because of extinction (see Section 3.3.4). Due to the magnitude criteria in our target selection, there are very few stars earlier than K in our sample. We will address this in a Chapter 4, where we attempt to identify the intermediate-mass members.

We use the following criteria to identify young stars in our sample:

(1) We include all IR excess stars using *Spitzer/IRAC* and 2MASS JHK colors (the IR-excess selection criteria can be found in Gutermuth et al. 2009; the complete catalog will be published in Megeath *et al.* 2012). For all non-IR excess stars, we identify them as members if (2) Li absorption at λ6707Å is clearly detectable, and has an equivalent width consistent with youth (the EW(Li) has to be greater than the Pleiades value for the same spectral type from Briceno et al. (1997)), or (3) Hα

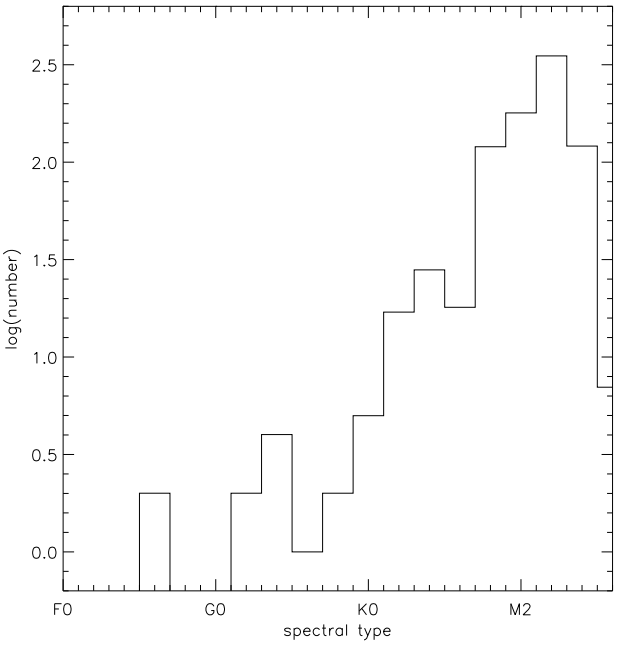

Figure 3.10: Distribution of spectral types of all confirmed members with spectral type information from Table 3.2. Due to the magnitude criteria in our target selection, there are missing stars earlier than K in our sample.

Table 3.1. Spectroscopic Members

Source	Confirmed Members	IR excess	no IR excess	Probable	Total
Hectospec	517	235	282	69	586
IMACS	311	142	169	24	335
Fang09[a]	36	29	7	5	41
Total	864	406	458	98	962

[a]Fang et al. (2009) cataloged 266 stars in L1641. The numbers here show only stars we did not observe.

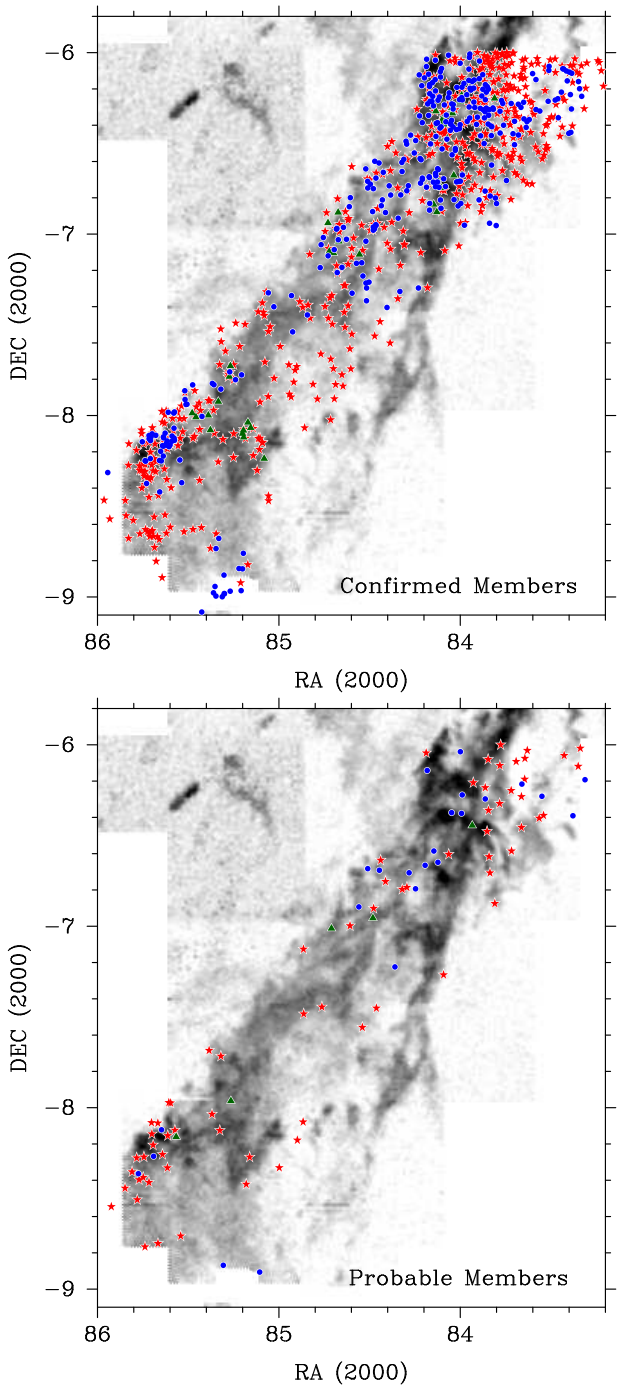

Figure 3.11: Top: Positions of spectroscopically confirmed members in Table 3.2 overplotted on ^{13}CO map from Bally et al. (1987). The symbols indicate the sources of the spectra. Red stars and blue circles represent objects observed with Hectospec and IMACS, respectively. Green triangles represent spectral types taken from F09. Bottom: Positions of probable members in Table 3.3.

emission is clearly above the background nebulosity.

Criterion (2) is reliable in selecting pre-main sequence M and late K stars, but for early K and G stars it can be more problematic, as Li depletion timescales can be quite long (see, e.g., discussion in Briceno et al. 1997). Thus, to identify G and early K members, we require that the equivalent widths of Li absorption lines to be greater than that observed in Pleiades (Briceno et al., 1997) or the Hα equivalent widths in emission or filled in above the expected absorption equivalent widths (Stauffer et al., 1997).

Whether or not the observed Hα emission - criterion (3) - is actually from the star or simply nebular emission can be difficult to distinguish in some regions and especially for faint stars. We therefore compiled two lists of objects, one with only confirmed members of L1641 and one that are potential members but have a higher contamination rate.

To ensure a self-consistent sample, we extracted members from the F09 sample using the same criteria used in our own spectra; therefore not all the members listed in F09 are included in our results here. In total, we adopted the F09 data for 41 stars that were not targeted in our observations, five of them are considered "probable members" due to the lack of Li absorption data.

Table 3.1 lists the number of confirmed members (including IR-excess members and non-excess members) and probable members from the three sources (Hectospec, IMACS, F09). Table 3.2 gives the positions, photometry, spectral types, etc. of the 864 confirmed members, confirmed either by their IR excess or unambiguous Li absorption. Out of the 864 confirmed members, 406 of them have IR excess, while 458 have no excess. Eight of the confirmed members are highly veiled by excess continuum emission, thought to be produced by the accretion shock on the stellar photosphere (Koenigl, 1991). Spectral typing is not possible for these objects.

Table 3.3 gives the positions, photometry, spectral types, etc. of the 98 probable members. The probable members are stars that show Hα emission and are in the strip of V vs. V-I CMD (see bottom panel of Figure 3.4) that most of the confirmed YSOs reside in. They do not, however, have IR-excess or unambiguous Li absorption line

(most likely due to low S/N of the spectra). We therefore catalog them as probable members. These probable members are excluded in our analysis and statistics unless otherwise noted.

The top panel of Figure 3.11 shows the positions of spectroscopically confirmed members overplotted on the ^{13}CO map from Bally et al. (1987). The distribution of the spectroscopic members in general follow the gas distribution. The bottom panel shows the positions of probable members. Probable members that are located near the group of confirmed members are more likely members whereas the ones far away from any confirmed members are likely non-members with nebular Hα emission.

Figure 3.12 shows the spectroscopically confirmed members on the CMD color-coded by their spectral types. It shows that we can spectral type objects down to M5-M6 as long as they are not highly extincted (in general, $A_V < 2$). There are some objects well below the YSO regions and most of which are IR-excess objects. Most likely they are edge on disk objects that are seen in scattered light and therefore appear much bluer than typical YSOs. This figure also shows that the magnitude limits of our optical photometry and spectroscopy are well-matched.

The solid lines in Figure 3.12, from top to bottom, are the Siess et al. (2000) isochrones for 1, 2, 3 and 4 Myr. Because the isochrones are almost parallel to the reddening vector, we can use the non-extinction corrected CMD to estimate the age of the population. Most of the population lies within the 1 Myr and 4 Myr isochrone, and the distribution peaks around 3 - 4 Myrs. Using the Siess isochrones, Da Rio et al. (2010) found the age of the ONC to be $\sim$ 2 - 3 Myr. The L1641 population, on average, thus appears to be slightly older than the ONC population, even though the age difference is comparable to the age uncertainties. This means that ultimately we should be able to make a direct comparison for IMFs using spectral types without correction.

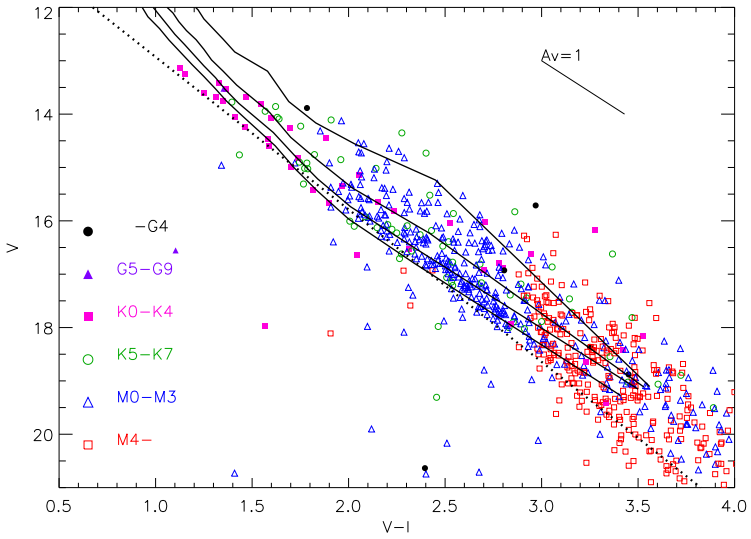

Figure 3.12: Spectroscopically confirmed members on the CMD color-coded by their spectral types (not corrected for extinction). The solid lines are 1, 2, 3 and 4 Myr isochrones from Siess et al. (2000) (from top to bottom) and the dotted line is the line used to define the YSO region. The minimum mass of the plotted isochrones is $0.1 M_{\odot}$.

3.3.3 Hα as a Membership Indicator and Accretion Diagnostics

The optical spectra also provide us with diagnostics of accretion. Table 3.2 and 3.3 list equivalent widths of Hα, which can be used as an indicator of accretion as the Hα luminosity correlates with the accretion luminosity. Fang et al. (2009) has an extensive discussion on accretion rates and disk properties in selected areas of L1641 using Hα, Hβ and He I λ 5876.

Table 3.4 lists other accretion indicator emission lines we found in the spectra. Note that if an emission line is not listed, it does not necessarily mean there is no emission line, but rather we cannot confidently tell that there is an emission line due to sky subtraction issues or limited spectral coverage in some IMACS data.

Figure 3.13 shows Hα equivalent widths of all confirmed members vs. spectral type. The Hα equivalent widths can be used as an indicator of accretion as the Hα luminosity correlates with the accretion luminosity. In general, the Hα equivalent widths have an increasing trend toward later spectral types and the IR-excess objects (red open diamonds) have higher Hα equivalent widths than the non-excess objects (black solid triangles). The shaded region shows the Hα equivalent width criteria for CTTS and WTTS by White & Basri (2003). Using this T Tauri criteria, 299 of the confirmed are CTTS and 565 are WTTS, which gives a CTTS/ WTTS ratio of 53%. In the early K to G spectral type range, there are a few stars with very low EW(Hα) equivalent widths.

We now look at the stars with very low Hα equivalent widths in more detail. The top panel of Figure 3.14 shows the Hα equivalent widths vs. spectral type for objects with Hα equivalent widths less than 1Å in emission. Note that in this plot emission is positive and that the y axis is in linear scale. The dashed line show the Hα equivalent widths measured in the Pleiades from chromospheric activity (Stauffer et al., 1997). We note that four of the members fall on or below the dashed line. The bottom panel of Figure 3.14 shows the Li equivalent widths of the same stars, where the stars with particularly low Hα are shown in asterisks. All the low-Hα stars shown in the top panel show Li absorption above the Pleiades level (Briceno et al., 1997) and are listed as confirmed members. Although it is possible that some of these objects are

Table 3.2. Confirmed Members of L1641

ID	RA (J2000)	Dec (J2000)	V (mag)	I (mag)	J[a] (mag)	H[a] (mag)	K_S[a] (mag)	Spectral Type	IR excess[b]	EW(Hα) (Å)	EW(Li) (Å)	Date observed[f]
1	83.21121	-6.18593	17.430	14.793	13.450	12.740	12.537	M3.0±0.6[c]	N	-4.30	0.4	Oct 22, 2011
2	83.22298	-6.10026	17.670	14.743	13.146	12.499	12.259	M3.6±0.6[c]	N	-11.0	0.4	Oct 22, 2011
3	83.23454	-6.05524	16.566	14.356	13.040	12.405	12.235	M1.5±0.7[c]	N	-6.00	0.5	Oct 22, 2011
4	83.24131	-6.04519	16.819	14.377	12.975	12.324	12.117	M2.6±0.5[c]	N	-4.00	0.3	Oct 22, 2011
5	83.30244	-6.05771	17.607	14.925	13.508	12.879	12.632	M3.0±0.6[c]	N	-4.20	0.3	Oct 22, 2011
6	83.30896	-6.19689	17.006	14.462	13.006	12.329	12.074	M2.6±0.5[c]	N	-22.6	0.3	Oct 22, 2011
7	83.31703	-6.30980	15.290	13.320	12.061	11.383	11.151	M0.5±0.5[c]	N	-3.60	0.5	Oct 22, 2011
8	83.33062	-6.24046	17.858	14.796	13.158	12.535	12.274	M4.6±0.6[d]	N	-7.90	0.3	Oct 11, 2011
9	83.33256	-6.07309	16.396	14.081	12.722	12.013	11.826	M2.2±0.6[c]	Y	-5.90	0.4	Oct 22, 2011
10	83.34235	-6.19836	15.604	13.608	12.415	11.724	11.530	M0.6±0.5[d]	N	-3.20	0.5	Oct 11, 2011

[a] J,H,K_S photometry is from 2MASS

[b] Criteria for IR excess are defined in Gutermuth et al. (2009) and Megeath et al. (2012).

[c] Data from Hectospec spectra.

[d] Data from IMACS spectra.

[e] Data from Fang et al. (2009). No spectral-typing error estimate.

[f] Local date at the beginning of the night.

Only a portion of the table is shown here. The full table is available on-line at `http://iopscience.iop.org/0004-637X/752/1/59/fulltext/apj429575t2_mrt.txt`

Table 3.3. Probable Members in L1641

ID	RA (J2000)	Dec (J2000)	V (mag)	I (mag)	J[a] (mag)	H[a] (mag)	K_S[a] (mag)	Spectral Type	IR excess[b]	EW(Hα) (Å)	EW(Li) (Å)	Date observed[f]
1	83.31244	-6.19215	18.897	15.697	14.001	13.429	13.142	M4.6±0.7[d]	N	-9.40	···	Oct 11, 2011
2	83.33856	-6.01960	19.102	15.608	13.731	13.171	12.890	M4.6±1.0[c]	N	-11.6	···	Oct 22, 2011
3	83.35003	-6.11952	16.900	14.259	12.708	12.051	11.804	M3.2±1.1[c]	N	-11.3	···	Nov 20, 2006
4	83.37934	-6.39085	18.752	15.434	13.776	13.197	12.927	M5.0±0.7[d]	N	-12.7	···	Oct 11, 2011
5	83.42722	-6.05974	19.915	16.364	14.475	13.786	13.501	M4.5±1.0[c]	N	-6.40	···	Oct 22, 2011
6	83.54100	-6.38943	17.206	14.619	13.204	12.576	12.333	M3.1±0.5[c]	N	-6.90	···	Oct 22, 2011
7	83.55022	-6.28399	18.653	15.151	13.345	12.711	12.427	M5.0±0.7[d]	N	-9.70	···	Oct 11, 2011
8	83.56502	-6.40473	19.209	15.796	13.950	13.362	13.053	M4.0±1.0[c]	N	-5.70	···	Oct 22, 2011
9	83.63090	-6.03181	19.917	16.230	14.216	13.575	13.287	M5.1±0.8[c]	N	-8.70	···	Nov 20, 2006
10	83.64370	-6.07540	19.709	16.125	14.116	13.593	13.246	M5.0±2.0[c]	N	-8.70	···	Oct 22, 2011

[a] J,H,K_S photometry is from 2MASS

[b] Criteria for IR excess are defined in Gutermuth et al. (2009) and Megeath et al. (2012).

[c] Data from Hectospec spectra.

[d] Data from IMACS spectra.

[e] Data from Fang et al. (2009). No spectral-typing error estimate.

[f] Local date at the beginning of the night.

Only a portion of the table is shown here. The full table is available on-line at `http://iopscience.iop.org/0004-637X/752/1/59/fulltext/apj429575t3_mrt.txt`

Table 3.4. YSOs with strong emission lines

ID	RA (J2000)	Dec (J2000)	[O I] 5577Å	[O I] 6300Å	[O I] 6363Å	[N II] 6548Å	[N II] 6583Å	He I 6678Å	[S II] 6716Å	[S II] 6731Å	[O I] 7773Å	[O I] 8446Å	[Ca II] 8498Å	[Ca II] 8542Å	[Ca II] 8662Å
6	83.30896	-6.19689	···	···	···	···	···	···	···	···	···	···	-0.56	-0.27	-0.12
9	83.33256	-6.07309	···	-2.0	-0.37	···	···	···	···	···	···	···	···	···	···
13	83.35634	-6.10948	···	-5.5	-1.4	···	-0.40	-1.4	···	···	-0.70	-1.9	-6.8	-6.5	-5.8
20	83.38751	-6.31044	-4.7	-81.	-27.	···	-7.7	-1.1	-5.6	-8.7	-1.0	-5.6	-15.	-16.	-13.
29	83.42479	-6.26354	···	-4.8	···	···	···	-2.2	···	···	···	-6.4	-5.7	-6.3	-5.2
34	83.43911	-6.07385	···	-0.49	···	···	···	-1.8	···	···	-1.0	-1.8	-20.	-22.	-18.
38	83.45954	-6.36361	···	-2.7	-0.70	···	-1.5	···	-0.16	-0.47	···	···	···	···	···
64	83.57055	-6.54707	···	-4.7	-1.2	···	···	···	···	···	···	···	···	···	···
89	83.65066	-6.09297	···	-0.75	-0.13	···	···	-1.4	···	···	-0.59	-1.4	-2.0	-2.1	-2.0
91	83.65124	-6.27344	···	-1.3	···	···	···	-2.2	···	···	···	···	···	···	···

Only a portion of the table is shown here. The full table is available on-line at `http://iopscience.iop.org/0004-637X/752/1/59/fulltext/apj429575t4_mrt.txt`

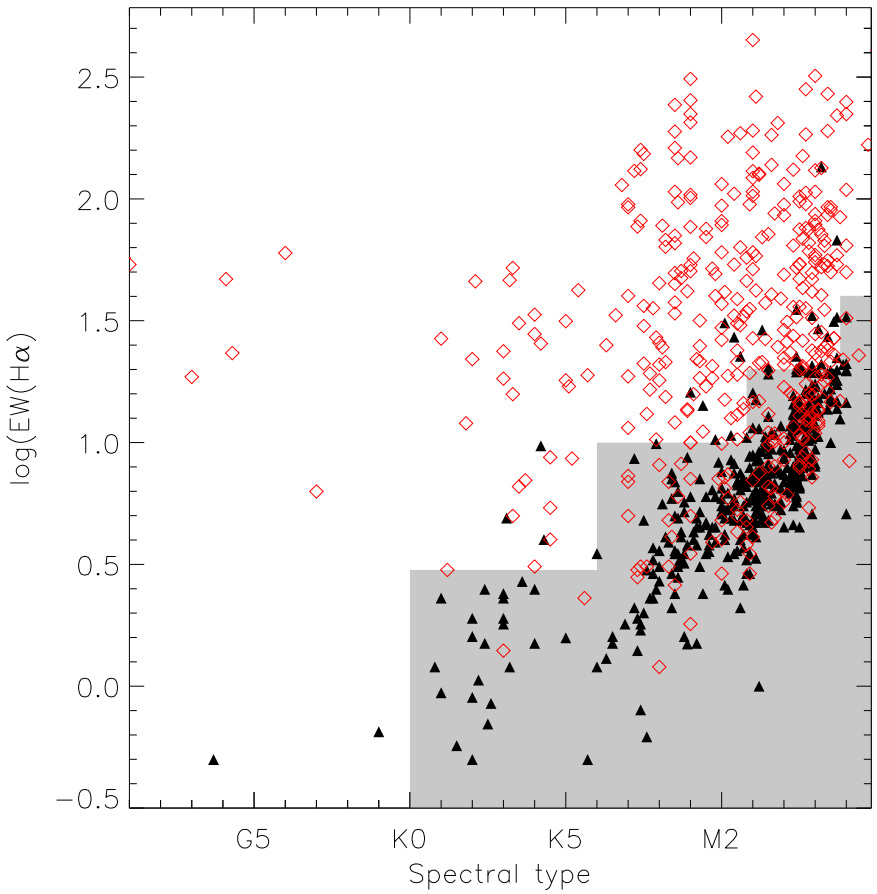

Figure 3.13: Hα equivalent widths (in log scale) of all confirmed members vs. spectral type. The red open diamonds are IR-excess members and black filled triangles are non IR-excess members. The shaded region shows where the WTTS objects reside using CTTS/WTTS classification from White & Basri (2003). Note that this classification only applies to stars later than K0.

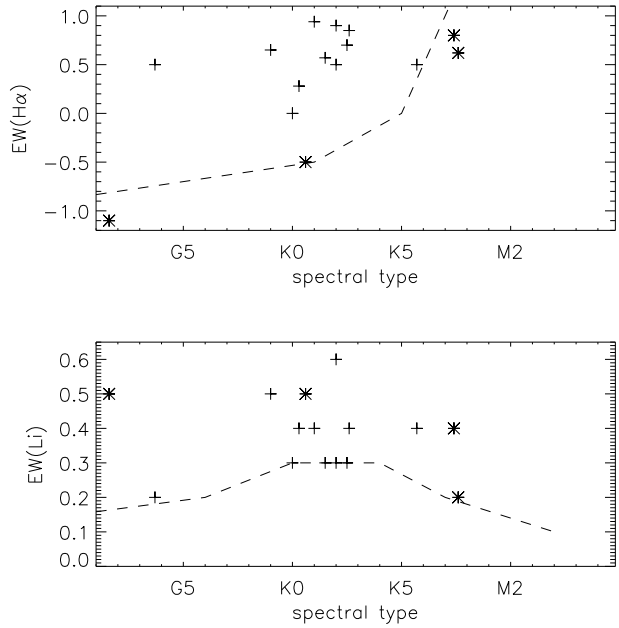

Figure 3.14: Top:Hα equivalent widths (in linear scale) of objects with Hα equivalent widths less than 1Å in emission. The dashed line is the approximate relation for chromospheric activity in the Pleiades (Stauffer et al., 1997). Note that here emission in Hα is defined as positive equivalent width, consistent with Figure 3.13, but different from Table 3.2. Bottom: Equivalent widths of Li absorption for the same objects. Absorption in Li is defined as positive equivalent width. The dashed line shows the approximate relation for the maximum Li absorption in the Pleiades for a given spectral type (Briceno et al., 1997).

from previous star-forming events in the Orion complex and still show Hα and Li, the number of low Hα objects is very small and has little effect on our overall sample.

3.3.4 Extinction

We use the color excess E(V-I) to estimate the extinction toward a star. For stars earlier than M4, we use the main-sequence colors from Kenyon & Hartmann (1995); For stars M4 and later, we use the intrinsic colors of young disk population described by Leggett (1992). We then calculate the extinction assuming a standard extinction law with R_V of 3.1 (Cardelli et al., 1989). The E(V-I) method has certain limitations and uncertainties. For example, Da Rio et al. (2010) have shown that accretion onto a star makes it look bluer and therefore the extinction would be underestimated.

Figure 3.15 shows the distribution of extinction vs. spectral type . 80% of our spectral-typed members have $A_V \leq 2$. On average, the IR-excess objects (open red diamonds) appear to have higher extinction than the non-excess objects, which is partially a selection effect because we are unable to identify non-excess members through Li absorption in high A_V regions where the S/N is much lower for the same spectral type. Negative values of A_V's are non-physical and are due to errors in spectral-types, photometry and also uncertainties in their intrinsic colors. Since the spectral-typing errors and photometric errors are larger for the faintest objects, it makes sense to see more negative A_V's s in the latest spectral types.

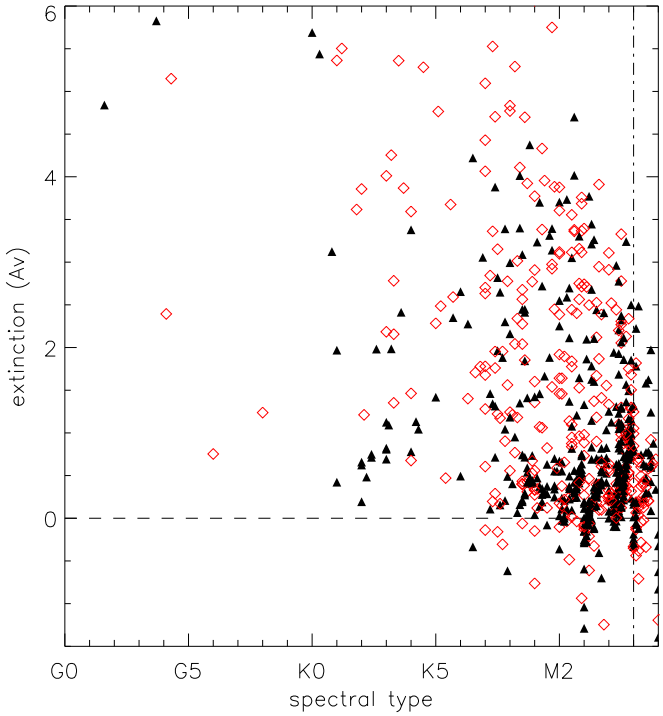

Figure 3.15: Extinction vs. spectral types for IR excess objects (red open diamonds) and non-IR excess objects (black solid triangles) estimated from E(V-I), assuming the standard extinction law from Cardelli et al. (1989) for R_V of 3.1 and intrinsic colors from Kenyon & Hartmann (1995) (for spectral types earlier than M4) and the young disk population in Leggett (1992) (for spectral types M4 and later).

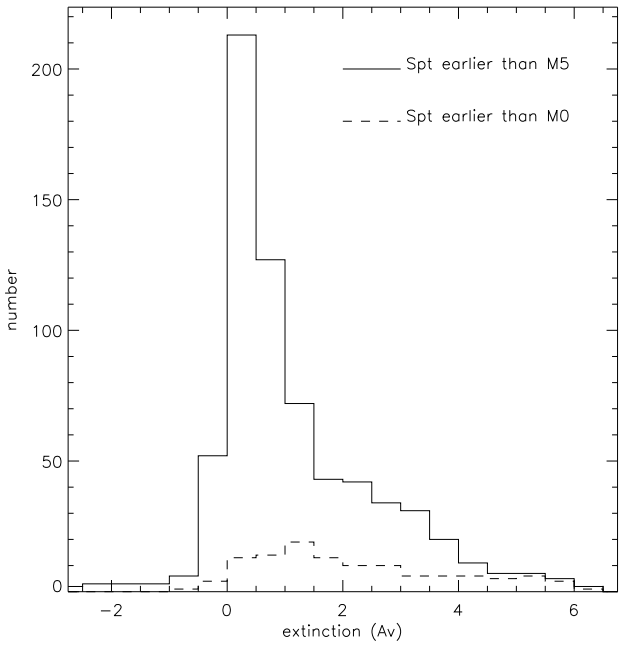

Figure 3.16: Distribution of extinction toward members with spectral types earlier than M5 (solid line) and members with spectral types earlier than M0 (dashed line). This illustrates that our sample does not have a uniform cutoff in extinction. The extinction is estimated from E(V-I) assuming the standard extinction law from Cardelli et al. (1989) for R_V of 3.1 and intrinsic colors from Kenyon & Hartmann (1995). Stars later than M5 are not considered because of the large uncertainties in spectral-typing and photometry.

Figure 3.16 shows the distribution of extinction of spectral-typed members earlier than M5 (solid line) and the subset of members earlier than M0 (dashed line). Stars later than M5 have large uncertainties in their spectral types and photometry and are excluded. The two distributions show that in extincted regions, our sample is biased toward more luminous objects because we did not apply an extinction cut in our sample selection.

We now turn our attention to the IR-excess population and assess what percentage of this population is highly extincted and not in our optical sample.

We use the 2MASS colors of the IR excess disk objects to estimate the extinction and assess the completeness of our spectroscopic sample. The top panel of Figure 3.17 shows J vs. J-H color magnitude diagram of all IR-excess objects. The objects that

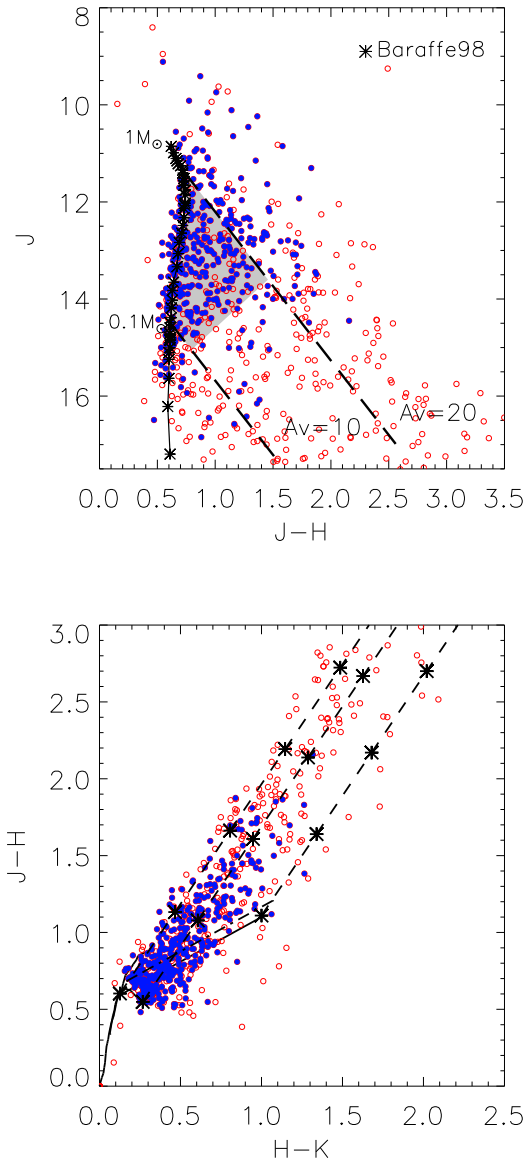

Figure 3.17: Top: J vs. J-H color magnitude diagram of all IR-excess objects. The objects that we spectral-typed are shown in solid circles (blue) and objects without spectral types are shown in open circles (red). Overplotted are the 3 Myr isochrone from Baraffe et al. (1998) and extinction vector from $1M_{\odot}$ ($A_V = 20$) and $0.1M_{\odot}$ ($A_V = 10$). In the shaded area, our optical spectroscopy sample is about 80% complete. Bottom: J-H vs. H-K color-color diagram. The two solid lines are the intrinsic colors of main sequence and giant branch (Bessell & Brett, 1988). The dashed lines and the asterisks show the extinction in A_V of 5 increments. In both plots, we use the standard extinction law from Cardelli et al. (1989) for R_V of 3.1.

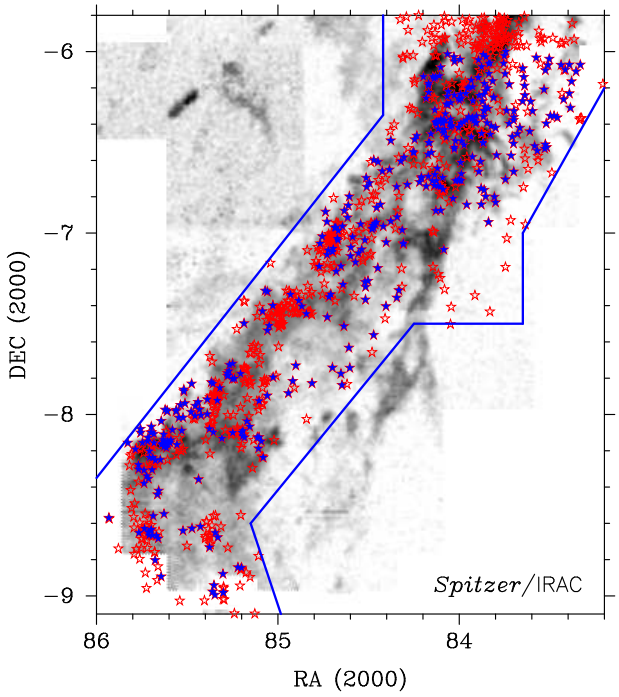

Figure 3.18: Same as Figure 3.1, but the IR-excess stas with spectral types are plotted in blue solid symbols and IR excess stars without spectral types are plotted in red open symbols. Most of the missing spectral types are due to high extinction.

we spectral-typed are shown in solid circles (blue) and objects without spectral types are shown in open circles (red). Overplotted are the 3 Myr isochrone from Baraffe et al. (1998) and extinction vector from $1M_{\odot}$ ($A_V = 20$) and $0.1M_{\odot}$ ($A_V = 10$). We use the isochrone from Baraffe et al. (1998) since they are appropriate for the mass range. We assume an age of 3 Myr because our optical photometry (Figure 3.12) shows that L1641 is approximately 3Mrys old (estimated using the Siess et al. 2000 isochrones). and the 3 Myr Baraffe et al. (1998) isochrone works the best to match up spectral type and J magnitudes. The bottom panel shows the J-H vs. H-K color-color diagram. The two solid lines are the intrinsic colors of main sequence and giant branch (Bessell & Brett, 1988). The dashed lines and the asterisks show the extinction in A_V of 5 increments. In both plots, we use the standard extinction law from Cardelli et al. (1989) for R_V of 3.1

From the distribution of the spectral-typed objects, we found that our ability to determine spectral types is limited by both the mass (corresponding to the J

magnitude) and extinction. For example we can identify and spectral type $1M_{\odot}$ stars in dense regions up to $A_V = 8$, but we can only identify and spectral type $0.1M_{\odot}$ stars up to $A_V = 2$. There are 234 IR-excess sources in the shaded region of the top panel of Figure 3.17 and more than 80% of them (192) are spectral-typed. If we limit ourselves to objects with $A_V < 2$ for 1 to $0.1M_{\odot}$, then our spectroscopic sample is about 90% (90/110) complete. We expect similar completeness for non-excess objects. Some of the intermediate-mass and massive stars are missing as a result of brightness limit of our spectroscopic survey, which we will address in Chapter 4. Of all the IR-excess objects that lie between the $0.1M_{\odot}$ and $1M_{\odot}$ line, only 60% of them have $A_V > 2$, which generally agrees with our previous finding that only half of the IR excess stars are visible in the optical with V< 21.

These results show that our spectral type distribution (Figure 3.10) is substantially incomplete at the latest types. This poses a problem for addressing the shape of the IMF at low masses, which we will also address in Chapterchap:highmass. However, from the point of view of determining whether the *high-mass* end of the IMF is deficient relative to the low-mass end, missing low-mass stars from our sample only means that our results will be underestimates of the significance of any depletion of high-mass stars.

Figure 3.18 shows the distribution of IR-excess objects and whether we have their spectral type data. No spectra were obtained for objects above -6° since they are not considered part of L1641. South of -6°, we have spectral types for 50% of the disk objects. Most of the missing spectral types are due to high extinction. In particular, the aggregates of stars between -7.6 - -6.8° in declination are highly-extincted (Gutermuth et al., 2011) and therefore were too faint for spectral typing.

Figure 3.19 shows the distribution in Declination (top) and the cumulative distribution (bottom) of the optical spectroscopically confirmed members (solid lines) and the distribution of all the IR-excess disk stars (dashed lines). In low extinction regions, we are able to classify most of the class II and class III's, and the number of spectroscopic members is larger than the IR excess sample; whereas in high extinction regions, there are very few optical members. For example, the number of optical

Table 3.5. Sample Definition

Definition	IR excess disks	no IR excess	Total Number
Spectroscopically confirmed members	406[d]	458	864
IR excess sample from Megeath *et al.* (2012)	723		723
IR excess sample with spectral type	406[c]		406
IR excess sample without spectral type	317		317
Class III's with moderate extinction [a]		$\gtrsim$458	$\gtrsim$458
All known members [b]	723	458	1181
Total Number of Class III's[c]		$\sim$900	$\sim$900
Number of moderately extincted stars	406	$\gtrsim$458	$\sim$ 860
Total number of stars	723	$\sim$900	$\sim$1600

[a]Estimated number from the V vs. V-I CMD, minus the extrapolated foreground contamination. See § 3.2.1.

[b]All known members include all spectroscopically confirmed members and the IR excess sample without spectral type.

[c]Assuming the class II/class III ratio is the same for the extincted population.

[d]This number include 8 objects that are classified as protostars, most of which are in fact flat-spectrum objects.

members is very small around Dec = -7.5° - -6.8° due to extinction.

3.4 Discussion

3.4.1 Low-Mass Population

In Section 3.3.2 we discussed our sample of optically confirmed members, including most of the moderately-extincted class II's and some class III's that were observed serendipitously. In Section 3.3.4 we discussed the sample of highly extincted class II's that are without spectral types. In this section, we will estimate the number of class III objects expected in L1641 from the CMD and compare this number to the number of class III's that we have already observed. Table 3.5 gives the definitions of the various populations and their numbers. (Note that numbers with $\sim$ signs are estimates).

We noted that most of the IR-excess stars fall in a small region on the optical CMD (Figure 3.4) between the top two parallel lines (described in Section 3.2.1). We expect that the Class III objects have similar ages and distances and therefore

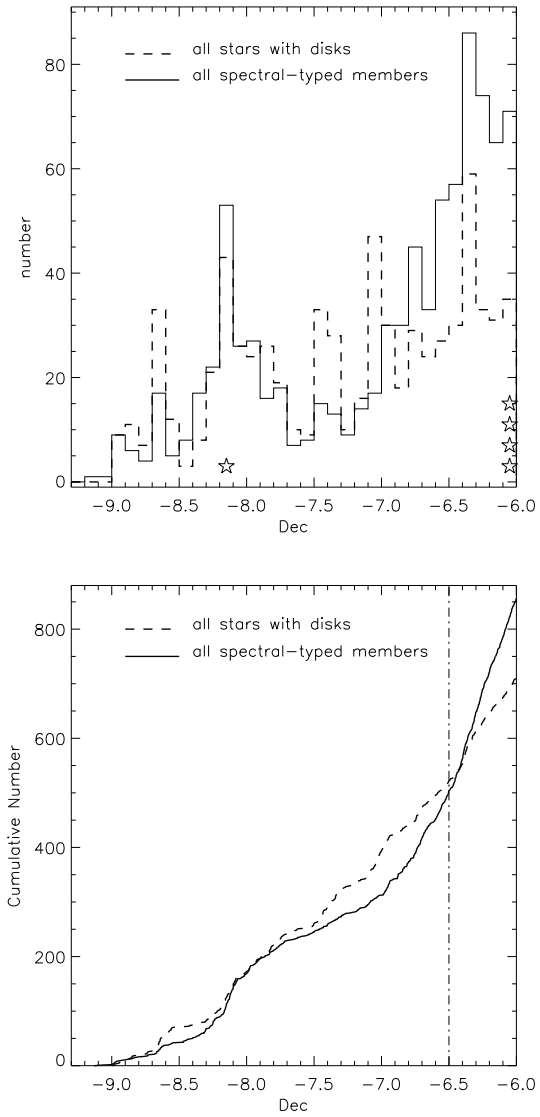

Figure 3.19: Top: Distribution of spectroscopically confirmed, spectral-typed YSOs (solid line) and all stars with disks (dashed line). The star symbols show the number of B0-B4 stars in each bin. The low number of spectral-typed stars around Dec = -7.5° - -6.8° is a result of high extinction in this declination range. Bottom: Cumulative distribution of stars along increasing Declination. The horizontal dash-dot line represents a more strict cutoff of L1641 at Dec = -6.5° (see Section 3.4.3).

fall in the same region of the CMD. However, not all the non-IR excess objects in this region are members. To estimate the fraction of the non-members in the non-IR excess sample, we use the strip one magnitude below the YSO region as a reference to estimate the number of foreground contaminants in the YSO region. Assuming no foreground extinction and uniform stellar density of foreground stars, the distribution of foreground stars in a given magnitude band is proportional to $10^{0.6\ m}$ (see Section 3.6 in Binney et al. 2000). Therefore, the number of foreground stars in the YSO region is predicted to be $10^{-0.6} + 10^{-1.2}$ times the number of foreground stars in the reference strip.

We restrict our extrapolation to V-I range of 2 - 3.5 as this is the only portion where we have data for both the reference and the YSO region. We identified 514 stars in the reference strip between V-I of 2 - 3.5 (only a very small fraction of which are members). The estimated contamination in the YSO region is therefore $514 \times (10^{-0.6} + 10^{-1.2}) \approx 162$ stars. There are 496 non-IR excess objects in the YSO region between V-I of 2 to 3.5. We therefore estimate that about 33% of the non-excess stars in the YSO strip are non-members.

The entire YSO strip from V-I of 0.5 to 4 has 772 non-excess stars. If we take the same contamination rate of 33%, we estimate that $772 \times (1 - 33\%) \sim 520$ of these non-excess stars are members. This agrees roughly with the number of class III objects (458) that we confirmed spectroscopically and shows that we have identified the vast majority of the class III objects subject to our extinction limits.

Approximately half (347 out of 723) of the IR-excess objects are identified in the optical photometry. If we further assume that the ratio of class II to class III's is constant even for the more extincted population, then we can estimate that there are approximately $458 \times 2 \sim 900$ class III objects. The total population of Class II + Class III stars in L1641 would then be roughly ~ 1600.

The above calculation, of course, is a very rough estimate, and depends upon our assumptions. First, we assumed that the the foreground stars are all main sequence stars and are uniformly distributed. We have also implicitly assumed that the class II to class III ratio is constant for all spectral types, while the observed disk frequency is

a function of spectral type (see e.g. Lada 2006); however, this is probably a reasonable assumption for the majority of our members, as the disk frequency seems to decrease most strongly for stars earlier than M. The assumption that the disk frequency is the same for the extincted population can also be problematic. The *Spitzer/IRAC* survey has found that Class II objects in L1641 are more distributed spatially compared to the class I's (Allen et al., 2007); similarly, it may be that the Class III objects are more distributed and have lower extinction systematically than the Class II stars. Megeath et al. (2012) estimated a disk fraction of 70 - 80 % in denser regions of L1641 by using off fields to subtract out the number of contaminating stars, higher than our the disk fraction we found for moderately extincted stars. Therefore, assuming the same disk fraction could lead to an overestimate of the number of class III stars.

We can compare the number of low-mass stars in L1641 to the results from surveys of the ONC. The ONC region has been surveyed multiple times both in the IR and in the optical. The number of sources found highly depends on the area and depth of the specific surveys. Most of the IR surveys go much deeper than 2MASS, which makes comparing the number of sources more difficult. The optical survey of Da Rio et al. (2010) is probably the most comparable to ours since they have a 50% V band completeness limit of 20.8. In an area of $34'$ by $34'$ they identified $\sim$ 1500 stars that are both present in the V and I bands. Hillenbrand (1997) also has a similar survey area and found similar number of objects. Therefore, we conclude that L1641 contains comparable number of stars as the half degree field centered on the ONC to within a factor of 2. This suggests that a direct comparison of the stellar IMFs in the two regions can be statistically meaningful.

3.4.2 High-Mass Population

With an idea of the number and spatial distribution of low-mass stars in L1641, we can now look into the high-mass end of the IMF. We search for known early type stars in L1641 in the catalog of spectral types compiled by Skiff (2010). There are no O stars in the area shown and the known early B type (B0 - B4) stars are shown in Figure 3.20, overlaid on the ^{13}CO map(Bally et al., 1987). Table 3.6 lists

Table 3.6. List of early B-type Stars in L1641

#	RA (J2000)	Dec (J2000)	Name	Spectral Type[a]	V[b] (mag)	B-V[b] (mag)	In Spitzer Field?[c] Y or N
1	83.7542	-6.00928	HD 36959	B1.5V[d]	5.68	-0.21	Y
2	83.7612	-6.00203	HD 36960	B0.5V[e]	4.79	-0.25	Y
3	83.8156	-6.03275	HD 37025	B2/3V[f]			Y
4	84.1487	-6.06475	HD 37209	B3IV[g]	5.72	-0.22	Y
5	84.6582	-6.57397	HD 37481	B2V[h]	5.96	-0.22	N
6	85.3434	-6.93519	HD 37889	B2.5Vsn[e]	7.65	-0.1	N
7	85.5888	-8.13339	HD 38023	B4V[i]	8.88	0.33	Y

[a]Most recent spectral type from Skiff (2010).

[b]Optical photometry from Warren & Hesser (1977).

[c]The position on the sky is within the Spitzer field. We use the Spitzer field as a proxy of the main body of the cloud.

[d]The spectral type information comes from Walborn & Fitzpatrick (1990)

[e]The spectral type information comes from Abt & Levato (1977)

[f]The spectral type information comes from Derviz (1983)

[g]The spectral type information comes from Abt (2008)

[h]The spectral type information comes from Zorec et al. (2009)

[i]The spectral type information comes from Racine (1968)

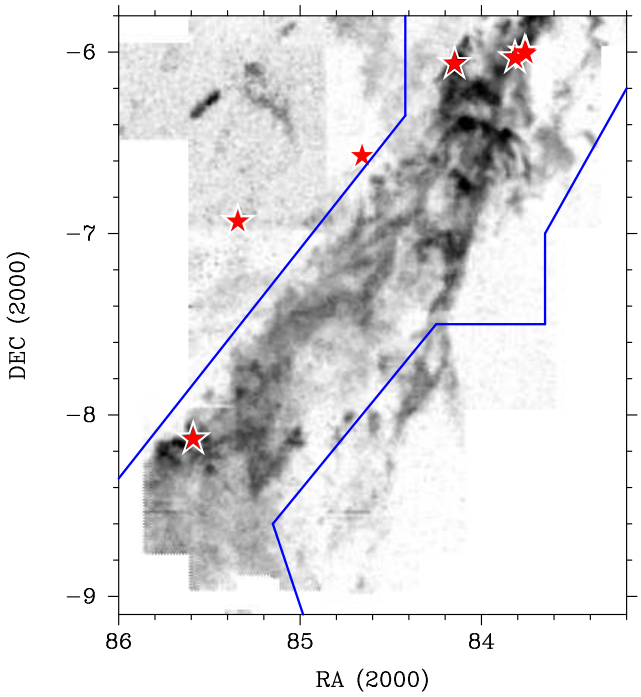

Figure 3.20: Positions of known B0 - B4 stars near L1641 overlaid on the ^{1}3CO map (Bally et al., 1987). The blue solid line outlines the *Spitzer/IRAC fields. The spectral type information is taken from the spectral type compilation by Skiff (2010). There are no O stars in this region.*

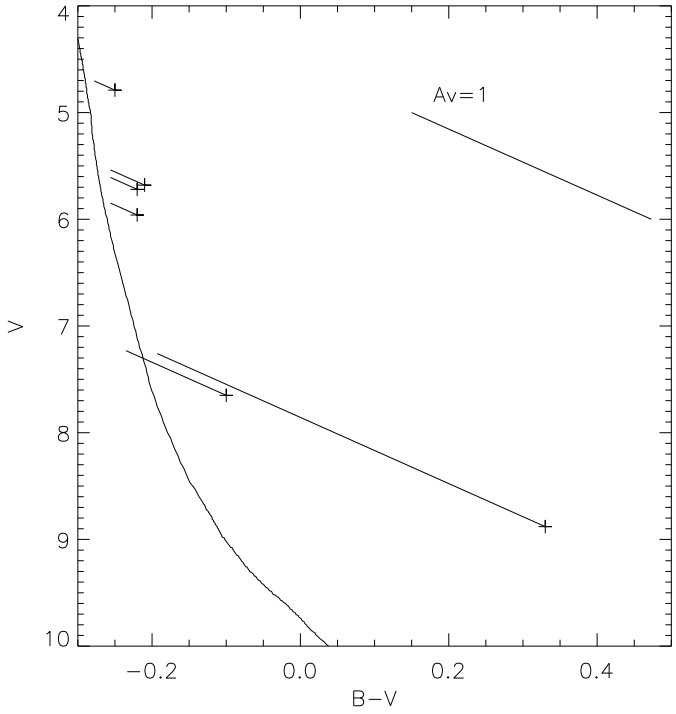

Figure 3.21: V. vs. B-V CMD of B type stars near L1641 (shown in Figure 3.20). The photometry is taken from Warren & Hesser (1977). The curved solid line is the ZAMS from Schaller et al. 1992 (Geneva tracks). Note that B and V photometry are not available for all B type stars. The solid line extending from each star shows its de-reddened position on the CMD, where the extinction is calculated from the E(B-V) color excess.

the positions, spectral types and photometry of these stars. In the case of spectral classifications from multiple sources, the most recent classification is used. There are a total of seven early B stars in this region. Four of the early B stars (1 - 4 in Table 3.6) are on the northern tip of the cloud and potentially denote the outer regions of the ONC; two other stars (5 and 6) are not associated with the cloud if seen in ^{13}CO emission but could be associated with the lower density gas probed by the near-IR (2MASS) extinction map. Since we do not have information on the low-mass population in their surroundings and they are not clearly associated with L1641, we will not consider these two stars in the IMF analysis. The other early B star (7) is the B4 star near (RA,Dec) = (5:42:21.3, -08:08:00) (Racine, 1968). Figure 3.21 shows the V vs. B-V CMD of these early B stars with photometry from Warren and Hesser (1977) with the ZAMS from Schaller et al. 1992 (Geneva tracks) overplotted. The dereddened position of each star is also shown, where the extinction is calculated from the E(B-V) color excess. All the known early B stars are consistent with the ZAMS at the distance of 414 pc, which means they are likely associated with Orion A.

From Figure 3.21, we found that all of the known early B stars have small extinctions of $A_V < 2$, which is a result of the depth of the Warren & Hesser (1977) photometry. It is therefore possible that there are embedded O or early B stars that have not been found. However, based on the existing *Spitzer* survey (Megeath et al., 2012), it is unlikely that we miss an early B star. Evolved O or early-B stars would have blown away materials nearby in a manner similar to the B4 star near (RA, Dec) = (5:42:21.3, -08:08:00) and therefore will not have high extinction. The reflection nebula near the B4 star is the only one seen in our field, which supports that there are no evolved early-B stars. (Note that there is another reflection nebula, powered by a potentially massive star further south, outside of the fields of our optical studies.) On the other hand, if there were unevolved, highly-extincted early-B stars, they would probably heat up the dust nearby and be identified as bright IR-excess sources by the *Spitzer* survey. We first examine possible high-mass disk objects in the J vs. J-H CMD (top panel of Figure 3.17). The brightest star in the J band is on the upper left

corner and has a spectral type of A1. A few other stars appear to have similar mass and are more extincted, but they all have similar masses according to the diagram. The only exception is the FU Ori star V883 Ori (with J = 9.25 and J-H = 2.49), which is dominated by accretion luminosity. We then examine the protostars that have large bolometric luminosities. The most luminous protostar in L1641 is located at (RA, Dec) = (5:40:27.4,-7:27:30) in one of the high-extinction clumps. It has L $\sim$ 490 $L_{\odot}$(Kryukova et al., 2012), and according to the Siess (2000) isochrones, has a mass less than 7 $M_{\odot}$.

3.4.3 Comparing the High-Mass IMF of L1641 to Analytical IMFs

In Section 3.4.2, we discussed the high mass population in L1641 from a literature search. In our following analysis, we assume that there are no other early B stars in the region. All but one of the early B stars are in the northern region contiguous with the ONC region. This raises the question of how we should define the region in which we construct the IMF. We need to adopt a more conservative definition and limit our sample to stars from a lower declination. This also means we have to compromise for a smaller sample size. Figure 3.19 shows that a large number of the confirmed members lie in the northern end of the cloud and that our sample size will be considerably smaller if we consider only the members further south. We need choose carefully a cutoff for our L1641 sample.

Here we discuss whether this lack of high mass stars is statistically significant with the following two approaches: 1. considering the entire L1641 region south of -6° and 2. considering only the stars south of -6.5°. For comparison, we also consider the region between -6° and -6.5°, which is a relatively higher density region in L1641 and contains 4 early B stars. Given the sample size n and the mass of the most massive star in the region M_{max}, we can then calculate how unlikely that this sample is drawn from analytic IMF models. Here we only consider the Chabrier (2005) and Kroupa (2001) IMFs. The Chabrier (2003) IMF gives results that are in between the two IMFs discussed here.

First we normalize the IMFs between 0.1 and 120$M_{\odot}$. The Chabrier (2005) IMF

can be written as:

$$\xi(\log m) = \begin{cases} = A\ \exp\{-\frac{(\log m - \log 0.25)^2}{2\times(0.55)^2}\}, & 0.1M_\odot < m < 1M_\odot, \\ = 0.549A\ m^{-1.35}, & m \geq 1M_\odot, \end{cases} \tag{3.1}$$

where A $\sim$ 0.959 normalizes the total number to unity.

The Kroupa (2001) IMF can be written as:

$$\xi(m) \begin{cases} = 2A\ m^{-1.3}, & 0.1M_\odot < m < 0.5M_\odot, \\ = A\ m^{-2.3}, & m \geq 0.5M_\odot, \end{cases} \tag{3.2}$$

where the normalization constant A $\sim$ 0.1431.

The cumulative distribution function is

$$\begin{aligned} \Sigma(M) &= \int_{\log(m=0.1\mathrm{M}_\odot)}^{\log M} \xi(\log m)\ d\log m \\ &= \int_{m=0.1\mathrm{M}_\odot}^{M} \xi(m)\ dm \end{aligned} \tag{3.3}$$

The probability that a randomly sampled star from this IMF is more massive than $\mathrm{M_{max}}$ is $p = 1 - \Sigma(\mathrm{M_{max}})$. In a population of n stars, the expected number of stars more massive than $\mathrm{M_{max}}$ is $E(>\mathrm{M_{max}}) = np$. The probability that the most massive star is below $\mathrm{M_{max}}$ is $P = (1-p)^n$.

Table 3.7 lists the sample size n, the most massive star in the region $\mathrm{M_{max}}$and $p = 1 - \Sigma(\mathrm{M_{max}})$, $E(>\mathrm{M_{max}}) = np$ for both Chabrier (2005) and Kroupa (2001) IMFs. Note that here we consider two sample sizes: spectral-typed members and total known members, which is the sum of spectral-typed members and the IR-excess members that are too extincted for optical spectroscopy. Generally, the Chabrier (2005) IMF gives a higher number of high-mass stars and therefore it is less likely to find no high-mass stars.

If we consider the entire L1641 region south of -6°, the most massive star is a B0.5V star (corresponding to $\mathrm{M_{max}} \sim 16\mathrm{M}_\odot$). We expect to see 2.4 to 4.4 stars more

massive than the B0.5V star in such a population. If the populations are randomly drawn, the probability of not finding any star more massive than $16M_{\odot}$is quite low (0.012 to 0.091). Therefore, this population has fewer high-mass stars compared to the analytic IMF models, but the result is not very statistically significant.

If we consider only the region between -6° and -6.5°, the most massive star in this region (B0.5V) is compatible with random sampling of both the analytical IMFs.

By limiting our sample to stars south of -6.5° and on the cloud (i.e. within the *Spitzer* survey area), we can ensure that our sample is not confused with stars from the ONC. There are no stars earlier than B4 (corresponding to $M_{max} \sim 7M_{\odot}$) in this sample. We expect to see 4.3 to 9.6 stars more massive than the B4V star in such a population. If the populations are randomly drawn, the probability of not finding any star more massive than $7M_{\odot}$is very low (1.4×10^{-2} to 6.4×10^{-5}). If we consider only the 500 members with optical spectral-types, the population is incompatible with the analytic IMFs to a 2 - 3 σ level; if we further include the 262 IR-excess members without optical spectral-type, the population is incompatible with the analytic IMF to a 3 - 4 σ level.

Even though we currently cannot constrain the total number of highly extincted stars, the total population will only be larger if we consider highly-extincted class III stars. Assuming a complete sample of early B stars and the lower limit of low-mass stars, the probabilities we calculated above are upper limits. Therefore the existence of highly-extincted low mass stars will only strengthen and not weaken our conclusions. On the other hand, our conclusion relies very strongly on the assumption that there are no highly-extinced high mass members, especially stars earlier than B4 in the region south of Dec = -6.5°. We also want to point out that the expected number of high-mass stars varies greatly for different IMF models due to their discrepancies in the low-mass end. The low-mass IMF is less well-studied and the discrepancies in the models can be viewed as an indication of the uncertainties.

Since we do not yet have a complete analysis of the high-mass and intermediate-mass stars in L1641, we choose not to present an HR diagram of the low-mass sample alone. We will present the high-to-intermediate mass sample in Chapter 4, in which

we will be able to construct a full IMF (down to M3) of L1641 and compare it to that of the ONC.

3.5 Conclusions

We conducted an optical photometric and spectroscopic survey of L1641 to test whether IMF varies with the environmental densities. Our spectroscopic sample consists of IR-excess objects selected from the *Spitzer/IRAC* survey and optical photometry and non-excess objects selected from optical photometry. We have spectral-typed 406 IR-excess members. We have also identified and spectral-typed 458 non-excess YSOs and 98 probable members through Li absorption and Hα emission. Our sample is limited by extinction and stellar mass in a complicated way, but overall we are able to spectral-type about 90% of class II and class III YSOs between 0.1 and 1 $M_\odot$ with $A_V \lesssim 2$. The number of spectroscopically confirmed class III objects is also consistent with the number of class III objects estimated from extrapolation of the V vs. V-I color magnitude diagram.

Assuming the class III/class II ratio is the same for the more extincted population, we estimate the total number of class II and class III's in L1641 to be around 1600, including 723 class II objects from the *Spitzer* survey and $\sim$900 class III's.

The total number of stars in L1641 is comparable within a factor of two to the number of stars used to construct the IMF in the ONC, even though the number depends on how our L1641 sample is defined. The optical photometry shows that the ONC and L1641 are of similar age, with L1641 being slightly older by $\sim$1 Myrs, indicating that any late-O to early-B star should still be on the main sequence. Assuming that we know all the early B stars in L1641, we compare the high-mass IMF to the standard analytical models. Compared to the standard models of the IMF, L1641 is deficient in O and early B stars to a 3-4σ significance level. We will make further improvements to our sample to better constrain the extincted population and compile a complete sample of B stars in Chapter 4, and the we will be able to make a direct comparison with the ONC.

Table 3.7. Samples by Region and IMF Probabilities

Region	n (Sample Size)	M_{max}[a]	$p = 1 - \Sigma(M_{max})$[b]	$E(> M_{max})$[c]	P(no stars greater than M_{max})[d]
L1641	Spectral-typed members 864	B0.5V	Chabrier05 3.74×10^{-3}	3.2	0.039
Dec < -6°		($16M_\odot$)	Kroupa01 2.77×10^{-3}	2.4	0.091
	Total Known Members[e]1181	B0.5V	Chabrier05 3.74×10^{-3}	4.4	0.012
		($16M_\odot$)	Kroupa01 2.77×10^{-3}	3.3	0.038
Dec = -6° to -6.5°	Spectral-typed members 364	B0.5V	Chabrier05 3.74×10^{-3}	1.4	0.26
		($16M_\odot$)	Kroupa01 2.77×10^{-3}	1.0	0.36
	Total Known Members[e]419	B0.5V	Chabrier05 3.74×10^{-3}	1.6	0.20
		($16M_\odot$)	Kroupa01 2.77×10^{-3}	1.2	0.31
Dec < -6.5°	Spectral-typed members 500	B4V	Chabrier05 1.26×10^{-2}	6.3	1.8×10^{-3}
		($7M_\odot$)	Kroupa01 8.55×10^{-3}	4.3	1.4×10^{-2}
	Total Known Members[e]762	B4V	Chabrier05 1.26×10^{-2}	9.6	6.4×10^{-5}
		($7M_\odot$)	Kroupa01 8.55×10^{-3}	6.5	1.4×10^{-3}

[a]Most massive star observed in this region.

[b]The probability that a random star drawn from the IMF is more massive than M_{max}.

[c]Expected number of stars more massive than M_{max}. $E(> M_{max}) = np$

[d]Drawing n stars from the given IMF, the probability of getting no stars more massive than M_{max}. $P = (1\text{-}p)^n$.

[e]Total known members include spectral-typed members and IR excess members without spectral type.

CHAPTER 4

Evidence for Environmental Dependence of the Upper Stellar Initial Mass Function in Orion A

4.1 Introduction

Does the formation of high-mass stars depend systematically on the environmental density of the star-forming cloud? In a recent review of this important question, Bastian et al. (2010) found no clear evidence for variations of the stellar initial mass function (IMF) as a function of initial conditions, but also concluded that further study in specific local and extragalactic environments is warranted. Even if the IMF is reasonably stable on a galactic scale, as a result of averaging over a variety of environments, it would still be of interest to discern IMF variations in specific regions as a clue to the processes of star formation.

Studies of very young regions are necessary to make a direct connection between environmental conditions and the production of massive stars. The most detailed investigations of the most populated nearby young clusters – the Orion Nebula Cluster (ONC; Hillenbrand 1997; Muench et al. 2002; Da Rio et al. 2010) and NGC 2264 (Sung et al., 2004) – are consistent with the the canonical IMF in general and with the Salpeter slope in the upper-mass end in particular (Bastian et al., 2010). Producing a statistically-significant test of the high-mass IMF is much more difficult in low-density regions (~ 1 – 10 stars pc^{-2}), such as Taurus or Chamaeleon, simply because there are too few low-mass stars to make a strong test (*e.g.* Luhman et al. 2009 for Taurus and Luhman 2007 for Chamaeleon I). Therefore, we need a survey of a large, well-populated low-density region with spectroscopic confirmation of membership to rule out line-of-sight contamination. It is also important to compare the high- and

low-density populations directly rather than comparing with inferred "universal" IMF forms, as the results may depend on the IMF form used and the statistical significance of disagreement can be difficult to infer (Bastian et al., 2010).

The Orion A molecular cloud is an ideal site to study star-formation in both high and low-density environments. While the ONC is one of the most thoroughly observed young dense cluster (the stellar surface density is $\sim$ 1000 pc^{-2} for the Trapezium cluster and $\sim$ 200 pc^{-2} for the whole ONC), the outlying regions provide us with a substantial low-density population. L1641, the low-density star-forming region south of the ONC, has a stellar population comparable to the ONC in size ($N > 1000$; Hsu et al. 2012; hereafter, Paper I), but has no large scale clustering and a much lower stellar surface density of $\sim$ 10 pc^{-2}, which makes it the best low-density region to study the high-mass IMF. It also has the advantage of being at approximately the same distance as the ONC ($\sim$ 414 pc; Menten et al. 2007; Kim et al. 2008), allowing the two populations to be compared directly.

In Paper I we presented an optical spectroscopic and photometric survey of the low-mass population in L1641 to test whether the previously-recognized lack of high-mass stars is statistically significant. Combining the optical data to the *Spitzer*/IRAC survey by Megeath et al. (2012), we identified and spectral-typed nearly 900 members; as we are unable to observe the heavily-extincted members, we estimated that L1641 may contain as many as $\sim$1600 stars down to 0.1M$_\odot$. Based on the large number of low-mass stars, we concluded that the lack of stars earlier than B4 is inconsistent with the canonical Chabrier (2005) or Kroupa (2001) IMFs to 3 – 4 σ significance.

In this chapter we expand our optical photometric and spectroscopic sample to the intermediate mass (late B to G) members to improve our estimates of the mass function. We first describe our observations and data reduction in Section 4.2. Then, in Section 4.3, we describe the observational results and attempts to use proper motions and radial velocities to reduce foreground/background contamination. In addition, we estimate the age of L1641 to be about 3 Myrs (see 4.3.6), so late O and early B stars should still be present. In Section 4.4, we compare the spectral type distribution and K-band luminosity function (KLF) of L1641 to that of the ONC,

finding that we cannot make detailed tests for differences between the two regions given problems of incompleteness and contamination. In Section 4.5, we relate our results to the mass of most massive star and cluster mass relation (Weidner & Kroupa, 2006) and discuss the challenges in searching for density dependence of the IMF. Our results are then summarized in Section 4.6.

4.2 Observations and Data Reduction

4.2.1 Target Selection

We aimed to target all the high to intermediate mass stars in L1641 with moderate extinction, regardless of whether they have disks. We selected our targets based on their 2MASS colors and USNOb (Monet et al., 2003) photometry because our photometric survey (described in PaperI) saturates at around I$\sim$12, which corresponds to late G to early K stars in L1641 in less extincted regions. The targets were selected using the following process:

1. We plotted the J vs. J-H color-magnitude diagram (CMD) of all objects with 2MASS magnitudes in L1641 (top panel of Figure 4.1). We then selected the targets that lie above the extinction vector originating from the location of a $1M_{\odot}$ star on the Baraffe et al. (1998) 3 Myrs isochrone. This sample included objects, if at Orion's distance, that are more massive than $1M_{\odot}$.

2. We excluded stars that already had optical spectral types from Paper I, which left us with 446 stars. In the top panel of Figure 4.1, the blue circles show objects with spectral types from Paper I.

3. We then compared the coordinates of our targets to the USNOb catalog. If there is not a match, then the star is too faint for our optical spectroscopy. We selected only objects that have B-R < 2.5 and B brighter than 15 in the USNOb catalog for spectroscopic followup.

A total of 136 potential intermediate-mass members were observed spectroscopically (4.2.2). Their positions on the J vs. J-H CMD are shown by the stars in the top

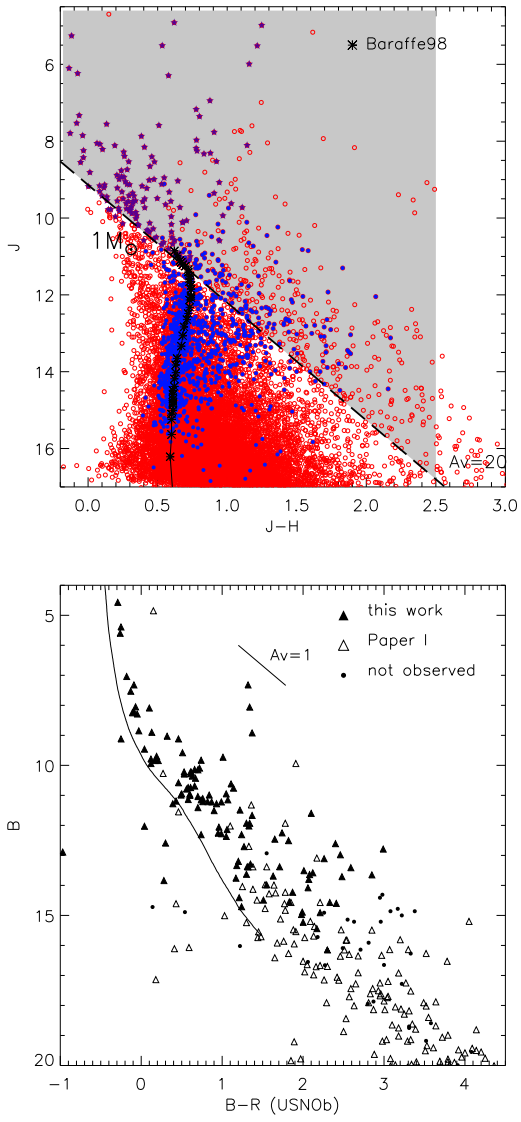

Figure 4.1: Top: J vs. J-H color-magnitude diagram (CMD) used to select targets from the 2MASS catalog. The grey shaded region indicates our initial cut for selecting targets. The blue solid circles are objects with spectral types from Paper I. The purple stars are objects that we observed with OSMOS in this study Bottom: USNOb B vs. B-R CMD of targets selected in the top panel. The solid triangles are targets observed in this work, the open triangles are targets observed in Paper I and the the black dots are objects that were not observed.

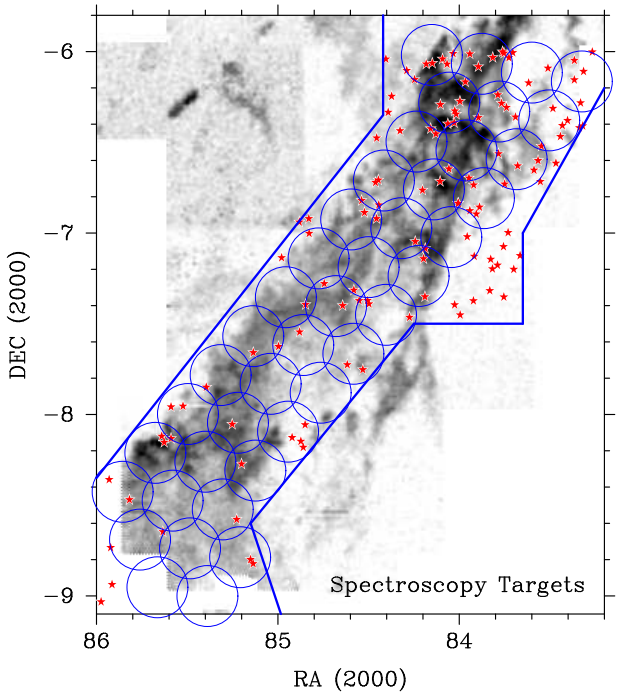

Figure 4.2: Positions of all stars observed with OSMOS spectroscopy, overlaid on ^{13}CO map from Bally et al. (1987). The blue boundary lines represent the fields covered by the *Spitzer*/IRAC survey of Orion (Megeath et al., 2012). The circles show the fields of the OSMOS photometry from Paper I.

panel of Figure 4.1. The bottom panel of Figure 4.1 shows the combined sample of stars observed in this chapter with the Ohio State Multi-Object Spectrograph (OSMOS) on the MDM 2.4m (Stoll et al., 2010; Martini et al., 2011) and stars from Paper I. The solid triangles are targets observed in this work, the open triangles are targets observed in Paper I. There are also a small number of stars that were not observed (black dots). These targets are too faint for the OSMOS spectroscopic observations. They were not observed with Hectospec or IMACS in Paper I because they either did not satisfy the selection criteria based on their position on the V vs. V-I CMD, including stars that we do not have I band photometry due to saturation. Also shown in this figure are the extinction vector corresponding to A_V=1 and the zero-age main sequence (ZAMS) from Lejeune & Schaerer (2001) (with models from Schaller et al. 1992). Figure 4.2 shows the positions of the observed stars on the sky.

4.2.2 Optical Spectroscopy of Intermediate Mass Stars

We obtained optical spectroscopy of selected objects (Section 4.2.1) with OSMOS. The observations were taken with center slit on the volume-phase holographic (VPH) grism, which yields a spectral range of 3100Å to 5950Å and efficiency peak at 5000Å. The 1.4″ slit was used, giving a spectral resolution of R=1400, or ∼2 – 4Å for the spectral range.

The data is first processed with the idl program proc4k written by Jason Eastman to subtract overscan and then bias subtracted, flat-field corrected with the MIS flat lamp to remove small-scale variation of pixel responses. Xenon comparison lamp (exposure time of 250s) is used for wavelength calibration as recommended for the center slit. Then the *IRAF* apall program is used to trace aperture and extract the spectra.

4.2.3 Optical Photometry of Intermediate Mass Stars

We used OSMOS in photometric mode to obtain $BVRI_C$ band photometry in the Johnson-Cousin system. The photometry observations were all done on the night of Jan 1 – Jan 2, 2012. The conditions were photometric with seeing $\sim 1.2''$ in the middle of the night.

Since the stars we are interested in are very bright stars that saturate in our previous photometric observations, we need to use an even shorter exposure time. (The saturation limit is I∼12 for 5s exposures; see Paper I for details.) We therefore used exposure time of 1 second for all four bands and took another 5 second exposure for the B band image. We observed the targets once with the telescope in focus and then once with the telescope out of focus and the images of stars are shaped like doughnuts. This strategy allows us to obtain photometry of brighter stars without saturating. The FWHM of the in focus images are around 1.1 – 1.4″, depending on the seeing, and the out of focus images have FWHM of 2 – 2.5 ″. The radius for the aperture photometry is 9 pixels, or 5″. To minimize errors due to shutter timing, we place the stars near the center of the field and use only the center 1k x 1k of the 4k x 4k CCD. The difference between the center and the edge of the field is about

2% in this 1k x 1k field. The 2 x 2 binning was used, which gives a plate scale of 0.55″ per pixel. For calibrations, we observed Landolt fields SA92, SA95, SA98 and SA101 throughout the night with the full field of view of OSMOS.

Each CCD frame was first corrected by overscan using the IDL program proc4k written by Jason Eastman. Basic reduction was performed following the standard procedure using *IRAF*. Sky flats were used in the flat-field correction. We then obtained aperture photometry with the *IRAF phot* package and manually choose our target stars or the Landolt standard stars. If the 5 second B band exposure is saturated, we use the magnitude obtained from the 1 second exposure. The photometric errors calculated by *IRAF phot* package are smaller than 0.04 mag in all cases. The rms departures of the Landolt stars from the calibration equations are $\sim$ 0.03 mag for all bands. We therefore expect our photometric errors to be less than 0.05 mag.

We were unable to obtain optical photometry for stars brighter than 9th magnitude in V due to saturation. We therefore use the B & V photometry from the Tycho-2 catalog (Høg et al., 2000). The Tycho-2 catalog is 99% complete to V 11.0 and the magnitude error is 0.013mag for stars brighter than 9th magnitude and 0.1mag for all other stars. The Tycho-2 photometry is transformed to the Johnson system by using the following equation (Perryman & ESA, 1997):

$$\begin{aligned} V_J &= V_T - 0.090(B-V)_T \\ (B-V)_J &= 0.850(B-V)_T \end{aligned} \tag{4.1}$$

4.2.4 Echelle Observations of Selected F & G Stars

To better distinguish foreground F & G stars from members (see Section 4.3.3), we observed 20 of the F & G stars with MIKE, the Magellan Inamori Kyocera Echelle on the Magellan Clay telescope on Feb 4 and 5, 2012. We used both the blue side (wavelength coverage: 3200 - 5000Å) and the red side (wavelength coverage: 4900 – 10000Å) simultaneously. The observations were taken with 0.7″ slits, which gives a resolving power of 42000 in the blue side and 32500 in the red side. For the red side, we used a milky flat taken using a hot blue star; for the blue side, we used a milky

flat frame taken with the quartz lamp. We also observed ThAr comparison lamps for wavelength correction. We reduced the data with the MIKE pipeline written by Dan Kelson and distributed as part of the Carnegie Python Distribution.

We then determine the radial velocities with the *rvsao.xcsao* task in *IRAF*, which cross-correlates the object spectrum with a set of template spectra. We use synthetic spectra from Munari et al. (2005) as our input velocity templates. The templates have temperatures from 3000 to 7000K, matching well with the temperature of the stars we observe. Each order was fitted independently, yielding a velocity and error estimate. We then obtain the weighted mean of the velocity estimates. Typical errors for the velocity estimates are $0.5\,\mathrm{kms}^{-1}$ for stars that are not rotating rapidly.

4.3 Results

In this section, we discuss how we determine membership and rule out background/foreground contamination as well as the results of optical spectroscopy and photometry of intermediate mass stars. Table 4.1 lists the RA, Dec, photometric $\mathrm{BVRI_C}$ magnitudes and spectral types of targets that we classify as members of L1641 (with some uncertain members in the F & G range, see discussion in 4.3.3). Table 4.2 lists objects that satisfy our selection criteria in Section 4.2.1 and observed with OSMOS targets, but ruled out as nonmembers.

4.3.1 Spectroscopy

We use SPTCLASS to spectral-type our targets (Hernández et al., 2004), a semi-automatic spectral-typing program. It uses empirical relations of spectral type and equivalent widths to classify stars. It has three schemes optimized for different mass ranges (K5 or later, late F to early K and F5 or earlier), which use different sets of lines. The user has to manually choose the best scheme for each star based on the prominent features in the spectrum and the consistency of several indicators. While SPTCLASS is insensitive to reddening and S/N of the spectra (as long as we have enough S/N to estimate the spectral indices), it does not take into account the effect of the hot continuum emission produced by the accretion shocks. This continuum

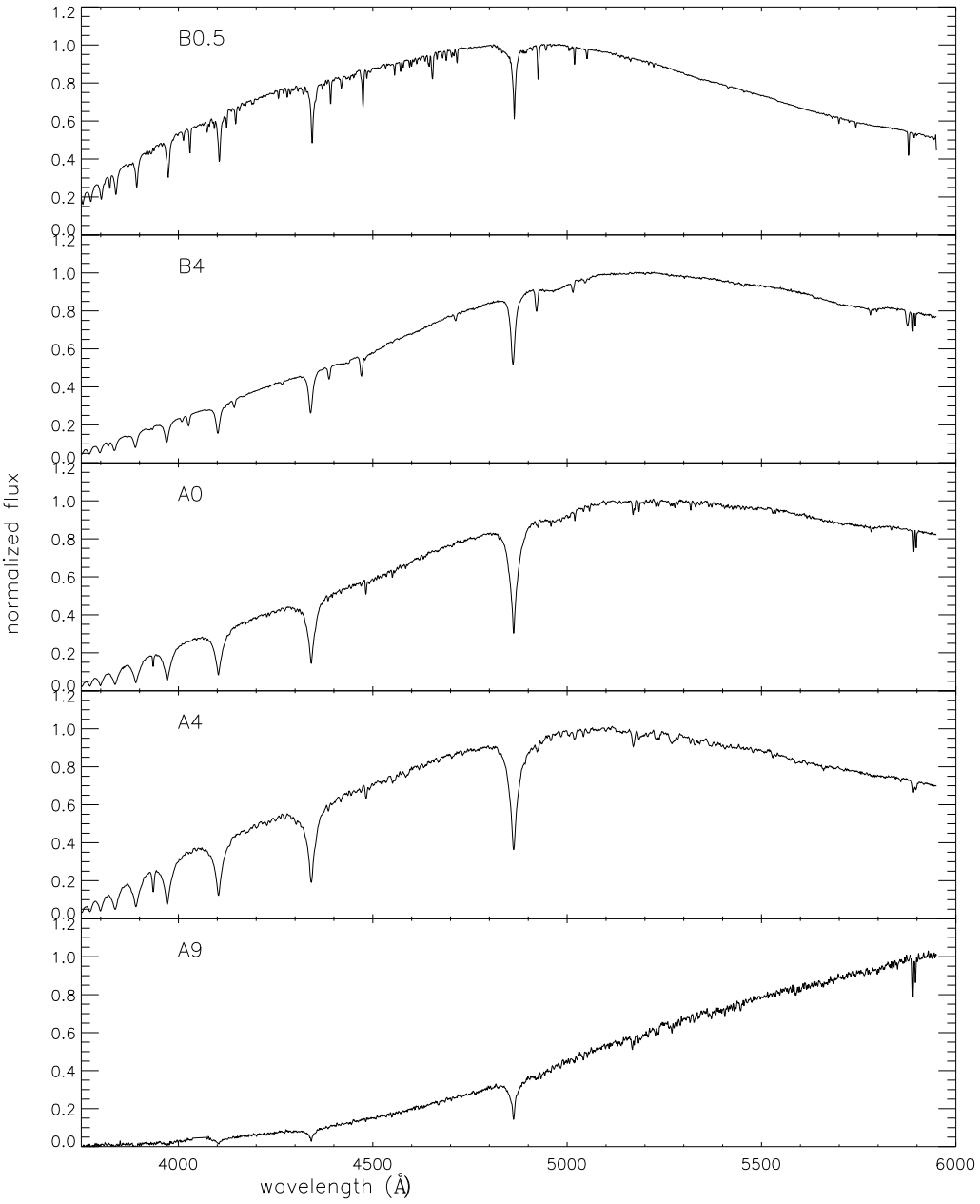

Figure 4.3: Examples of spectra from OSMOS arranged sorted by spectral types.

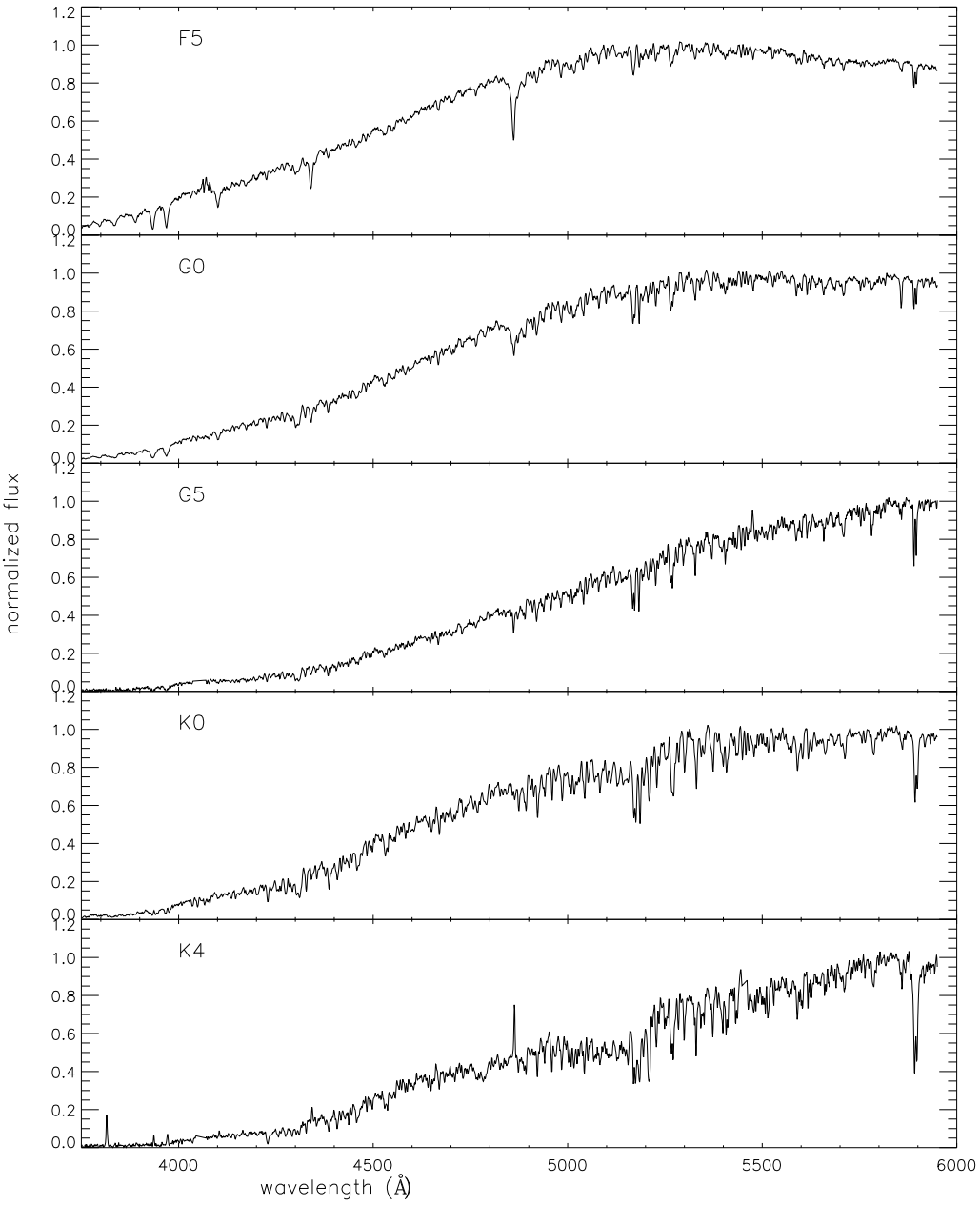

Figure 4.3: (Continued)

Table 4.1. Intermediate-mass Members of L1641

ID	RA (J2000)	Dec (J2000)	B (mag)	V (mag)	R (mag)	I (mag)	J[a] (mag)	H[a] (mag)	K_S[a] (mag)	Spec. Type	IR excess[b]	RV[c] (kms^{-1})	EW(Li)[c] (Å)	Note
1	83.31498	-6.10956	10.65	10.20	9.93	9.67	9.32	9.08	8.99	F4.0±2.0	N	17.0	0.1	
2	83.33185	-6.28275	13.92	12.72	12.08	11.52	10.63	10.09	9.93	K1.0±3.0	N	···	···	
3	83.36585	-6.04887	9.92	9.77	9.71	9.63	9.45	9.31	9.29	A4.0±2.0	N	···	···	
4	83.43192	-6.40788	···	13.59	···	12.23	11.21	10.53	10.39	K3.0±3.0	N	···	···	
5	83.46720	-6.61558	9.47	9.48	9.49	9.47	9.31	9.22	9.18	B9.0±1.5	N	···	···	
6	83.56561	-6.60124	15.21	14.06	13.37	12.46	10.59	9.65	8.97	G8.0±2.0	Y	···	···	
7	83.61783	-6.17349	13.93	12.82	12.15	11.47	10.51	9.91	9.73	K2.0±3.0	N	···	···	
8	83.67800	-6.63059	14.07	12.58	11.65	10.72	9.49	8.99	8.78	F7.0±2.0	N	···	···	
9	83.69040	-6.36113	15.40	14.06	13.18	12.27	11.02	10.35	10.16	K4.0±2.0	N	···	···	
10	83.70463	-6.00634	8.19	8.26	···	···	8.55	8.60	8.63	B8.3±1.4	N	···	···	

[a] J,H,K_S photometry is from 2MASS

[b] Criteria for IR excess are defined in Gutermuth et al. (2009) and Megeath et al. (2012).

[c] From Magellan/MIKE echelle data.

[d] Herbig Ae star V380 Ori.

Only a portion of the table is shown here. The full table is available on-line at `http://iopscience.iop.org/0004-637X/764/2/114/suppdata/apj457078t1_mrt.txt`

Table 4.2. Non-members of L1641 Observed with OSMOS

ID	RA (J2000)	Dec (J2000)	B (mag)	V (mag)	R (mag)	I (mag)	J[a] (mag)	H[a] (mag)	K_S[a] (mag)	Spec. Type	IR excess[b]	RV (kms^{-1})	EW(Li) (Å)	Note
1	83.24890	-6.11734	···	···	···	···	5.52	4.30	3.93	M8.0±2.0	N	···	···	g
2	83.26690	-6.00261	15.31	13.80	12.99	12.22	11.00	10.27	10.08	G6.0±2.0	N	···	···	g
3	83.31976	-6.40979	11.04	10.45	10.12	9.81	9.42	9.12	9.03	F9.0±2.0	N	···	···	f
4	83.33801	-6.41991	12.28	10.72	9.89	9.13	7.97	7.19	6.97	K3.0±3.0	N	···	···	g
5	83.36604	-6.15616	13.06	11.90	11.22	10.56	9.56	8.97	8.85	G2.0±2.0	N	77.0	0.0	def
6	83.40304	-6.38011	10.10	9.46	···	8.79	8.28	8.02	7.96	G0.0±1.5	N	23.5	0.0	def
7	83.44242	-6.46825	13.27	11.81	10.99	10.23	9.03	8.39	8.18	K0.0±3.0	N	···	···	g
8	83.48413	-6.31374	14.46	13.21	12.51	11.84	10.81	10.23	10.06	G3.0±2.0	N	-18.5	0.0	de
9	83.51110	-6.09196	14.77	12.88	11.75	10.68	9.07	8.13	7.91	F8.2±2.0	N	138.0	0.0	de
10	83.54718	-6.52211	11.81	10.87	10.38	9.93	9.23	8.80	8.72	G5.0±2.0	N	···	···	f

[a] J,H,K_S photometry is from 2MASS

[b] Criteria for IR excess are defined in Gutermuth et al. (2009) and Megeath et al. (2012).

[c] From Magellan/MIKE echelle data.

[d] Rejected based on radial velocity incompatible with the velocity of the cloud.

[e] Rejected based on lack of Lithium absorption.

[f] Rejected based on large proper motion.

[g] Rejected based on position on the color-magnitude diagram.

Only a portion of the table is shown here. The full table is available on-line at `http://iopscience.iop.org/0004-637X/764/2/114/suppdata/apj457078t2_mrt.txt`

emission makes the photospheric absorption lines appear weaker. SPTCLASS generally assigns an earlier spectral type to veiled stars than their and therefore the SPTCLASS outputs should be considered as the earliest spectral type limits. While SPTCLASS utilizes spectral lines from 4000Å to 9000Å, our OSMOS observations only cover a small spectral range from 3100Å to 5950Å. As a result, SPTCLASS was unable to classify some of the K type stars, which we classified by eye and assigned a larger uncertainty. Spectra of B & A stars are also rectified and classified by eye as a double-check, and the results are always similar to the SPTCLASS output within the errors. Figure 4.3 shows some sample spectra.

The earliest star found in the L1641 is a B0.5 star right at the very northern edge of the field. There are three other B1 to B3 stars within -6.1° <Dec < −6.0°. The earliest star south of this range is a B4 star at (RA,Dec) = (5:42:21.3, -08:08:00), first identified by Racine (1968). Among the 57 stars identified as members, there are 4 B0-B3 stars, 14 B4 - B9 stars, 9 A stars, 15 F stars, 5 G stars and 10 K stars. (Since we do not have radial velocity for our entire sample, we expect some of the A, F & G stars listed here are line-of-sight contamination. See 4.3.3.)

4.3.2 Photometry

Figure 4.4 shows the V-I vs. V and B-V vs. B color-magnitude diagram of all the members listed in Table 4.1 that have magnitude information in the bands plotted. For stars brighter than V∼ 11 the OSMOS observations might be saturated and the Tycho-2 magnitudes are used. Note that the most massive members are only shown in the B vs B-V CMD because we do not have their I band magnitude. The top panels show the CMD without extinction correction. The red symbols are objects with IR excess and the black symbols are the non-IR excess objects, as identified by Megeath et al. (2012). The bottom panels show the CMD with extinction correction, estimated by assuming intrinsic colors from Kenyon & Hartmann (1995, KH95) for stars earlier than M4 and Leggett (1992) for stars M4 and later and a standard extinction law with R_V of 3.1 (Cardelli et al., 1989). Overplotted are the ZAMS (solid) and 2, 4, and 10 Myr isochrones from Siess et al. (2000). The earliest type stars are essentially

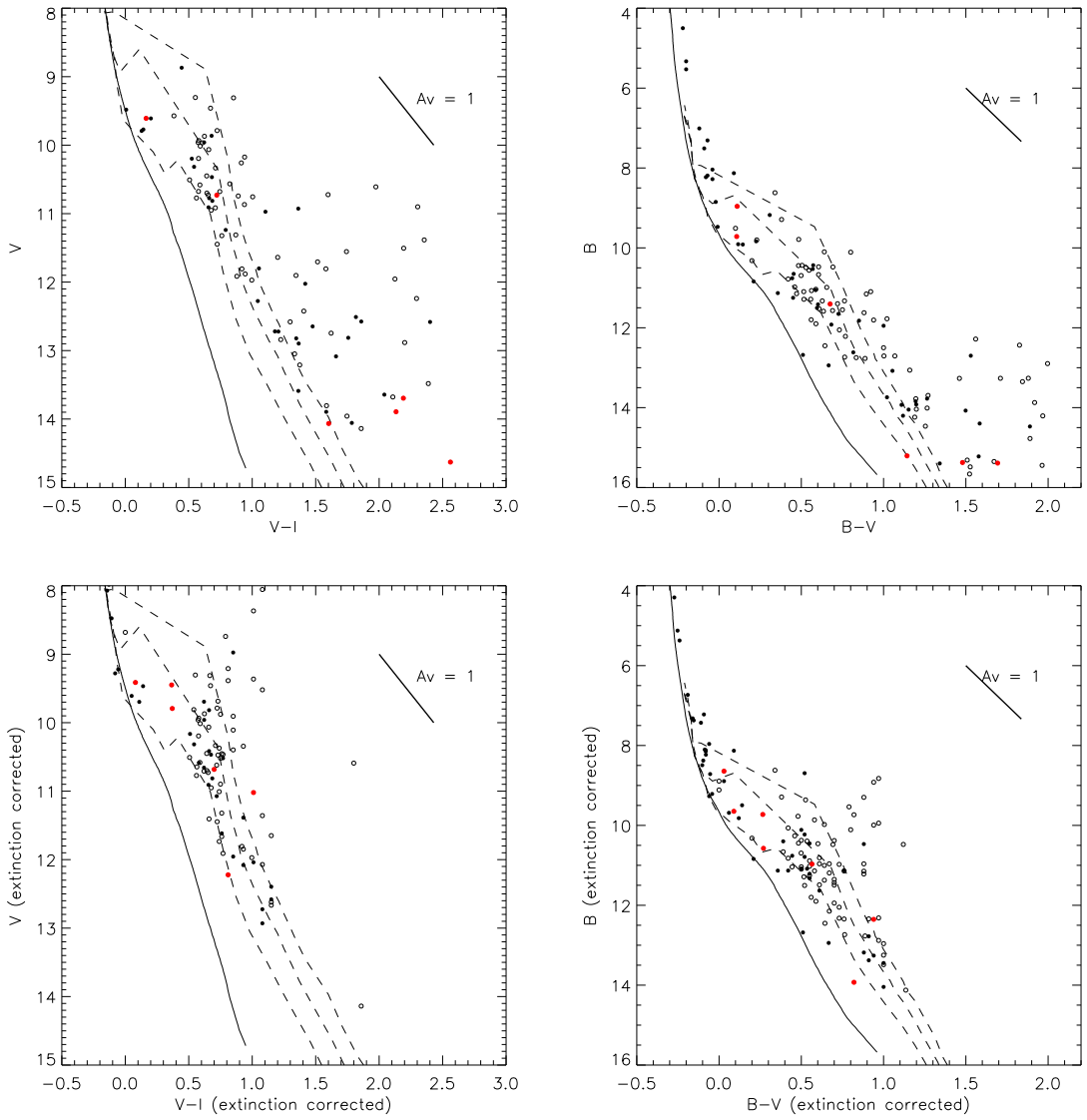

Figure 4.4: V-I vs V and B-V vs B CMDs of high-to-intermediate mass stars in L1641 with photometry. The dashed lines are 2, 4, and 10 Myr Siess et al. (2000) isochrones. The top panel shows CMDs without extinction correction; the bottom panel shows the same CMDs after correcting for extinction, assuming intrinsic colors of Kenyon & Hartmann (1995). The red symbols represent objects with IR excess. The open circles represent non-members and solid circles represent members.

on the main sequence whereas the later type stars are still above the main sequence.

Stars that are identified as non-members are removed from this figure. The background giants generally have large extinctions and lie above the 2 Myr isochrone around V-I of 0.5 - 1 and B-V of 1 in the extinction corrected CMD. Foreground objects are generally later type stars that are well-above the isochrones.

4.3.3 Membership

We expect significant contamination by non-members in our sample given the distance of L1641 and its large area on the sky. In Chapter 3, we used indicators of youth such as Li absorption and Hα emission in low-resolution optical spectra as well as the presence of IR-excess to determine membership for late type stars. In the intermediate mass range (A to G), confirming membership is more challenging. First of all, the disk fraction is lower for earlier type stars so we only find a small fraction of members with IR-excess. Secondly, intermediate mass stars have stronger Hα absorption lines which can obscure Hα emission from accretion. Finally, Li depletion timescales are longer for intermediate mass stars than for low mass stars. As demonstrated in Briceno et al. (1997), G type stars in Pleiades also show Li absorption, and the equivalent widths are hard to distinguish from that of pre-main sequence stars. As a result, we have to use additional kinematic information to help determine membership, and combine this with statistical estimates of contamination from the Besançon model of stellar populations (Robin et al., 2003) as described in Section 4.3.4.

Proper Motion

One way to help eliminate foreground stars is through their proper motions. At the $\sim$ 414 pc distance of Orion, we do not expect to detect large angular proper motions; stars with large proper motions are thus most likely foreground objects. In Figure 4.5 we plot the proper motions of our OSMOS targets from the UCAC4 (Zacharias et al., 2012). Most of our targets, as expected, show zero or very small proper motions. We fit Gaussians to the proper motion distributions in RA and Dec. The Gaussian fit to the proper motion distribution in RA peaks at 0.2 mas yr^{-1}and has a width of 2.0 mas yr^{-1}; the distribution in Dec peaks at -2.0 mas yr^{-1} with a

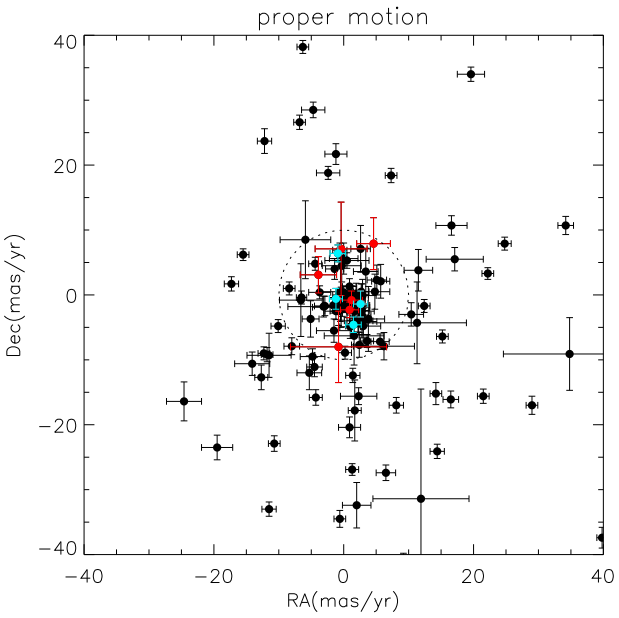

Figure 4.5: Proper motion of our targets from the fourth U.S. Naval Observatory CCD Astrograph Catalog (UCAC4; Zacharias et al. 2012). Stars with proper motions greater than 10 mas yr^{-1}, or 20 kms^{-1}, after the proper motion error is taken into account, are considered foreground objects. The red and cyan symbols represent members confirmed through IR-excess and radial velocity with MIKE echelle observations, respectively. The confirmed members all have small proper motions, well within the 10 mas yr^{-1} cutoff applied.

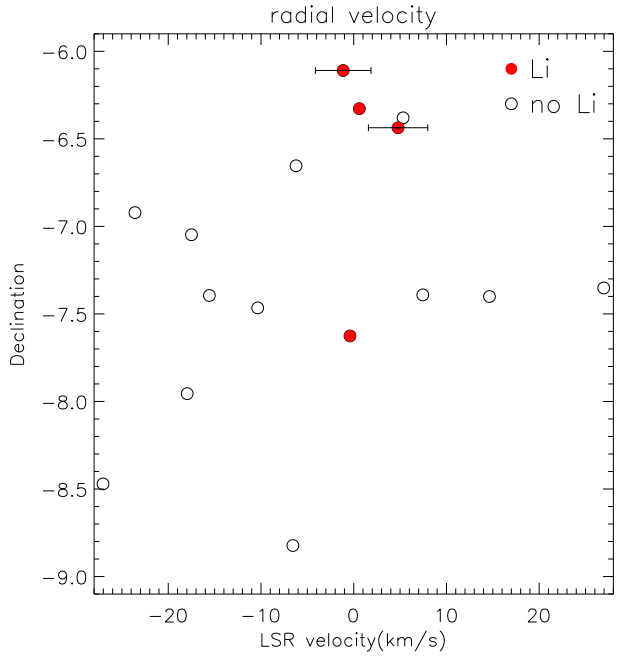

Figure 4.6: LSR velocities and Li absorption data obtained from Echelle observations of 20 F & G type stars in L1641. The red symbols are stars with Li absorption above the level seen in Pleiades (Jones et al., 1996). A member of L1641 should have velocities compatible (within 5 kms^{-1}) with the gas velocity (2 – 10 kms^{-1}, Bally et al. 1987) and Li absorption. The typical errors in velocity for slow-rotating stars are about 0.5 kms^{-1}, comparable to the size of the points. The points with error bars overplotted are fast-rotators, where velocity estimates are less certain.

width of 2.7 mas yr^{-1}.

We therefore apply a 3σ cut of 10 mas yr^{-1}, or 20 kms^{-1} and stars outside the circle (after taking into account of the proper motion errors) are considered foreground objects. Note that while 90% of the objects in this plot has errors of < 5 mas yr^{-1}, a handful of objects have larger proper motion errors and are therefore compatible with zero proper motion. This will make our effort to eliminate foreground objects less effective.

Radial Velocity

We observed 20 out of the 45 stars we classified as potential F & G members of L1641 with the MIKE echelle spectrograph. The radial velocities of these 20 objects are listed in Table 4.1 and 4.2 and shown in Figure 4.6. Members of L1641 should

have LSR radial velocities compatible with the gas velocity (2 – 10 kms^{-1}, with a gradient along north-south direction, Bally et al. 1987). Even though F & G stars usually have very weak Li absorption, we are able to measure the equivalent widths at high spectral resolution. In order to be considered a member, a star should have velocities compatible with the gas (we chose a range of -3 – 15 kms^{-1}, or within 5 kms^{-1} of the gas velocity) and also Li absorption stronger than that observed in Pleiades (Briceno et al., 1997). In Figure 4.6, we can see that most of the F& G stars observed do not have the cloud velocities and can be ruled out easily. There are 4 members that are compatible with the cloud velocities and show Li absorption. There are also one or two stars that have the cloud velocity but do not show Li absorption. The typical error for radial velocity determination is about 0.5 kms^{-1}, or the size of the dots. The larger error bars indicate fast rotating stars where it is more difficult to determine the radial velocity as accurately. However, since stellar rotation decreases with time (Skumanich, 1972), fast rotation is also a sign that these stars are young and therefore they are considered members.

To summarize the result of the membership determination, 79 out the 136 stars in our intermediate mass sample are ruled out as non-members from kinematics and their position on the CMD. Only 4 out of 20, or 20%, of the F & G type stars observed with MIKE turn out to be members. In the following discussions, we will assume that only 20% of the stars not observed with MIKE are members. However, as we do not know which stars in our sample are non-members, we retain them in Table 1 and Figure 4.7.

4.3.4 Completeness, Contamination and Sample Definition

From here on, we combine the sample of high-to-intermediate mass stars characterized above and the confirmed members of L1641 cataloged in Chapter 3 for our analysis. The sample from Chapter 3 has a total of 864 members, including our Hectospec and IMACS targets as well as the sample from Fang et al. (2009) and reference therein. The spectral types range from F to M4, where the F & G stars are mostly from the literature and not from our own observations. We assessed the completeness of the

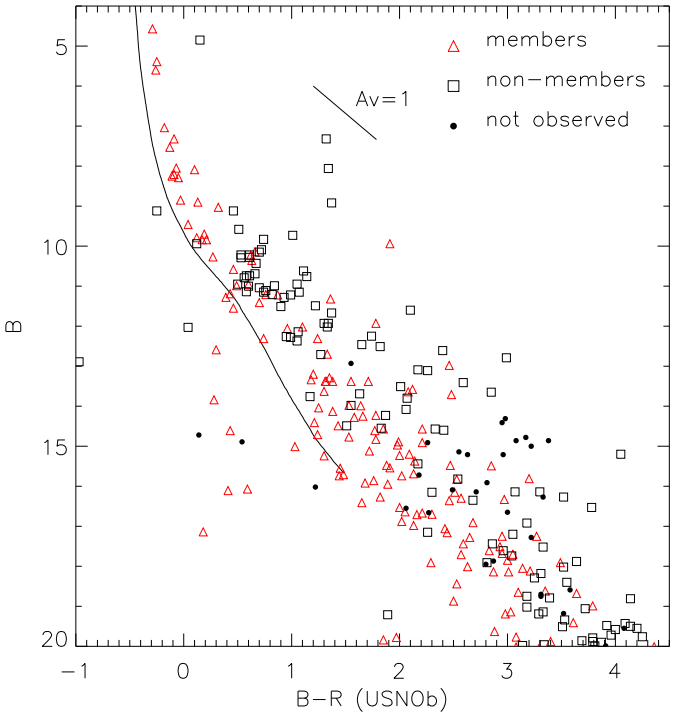

Figure 4.7: USNOb B vs. B-R CMD of candidate intermediate mass stars selected through 2MASS. The red triangles are members of L1641, the black boxes are non-members of L164 (see Section 4.3.3 for how membership is determined). The black dots are objects that were not observed. Note that some of the spectral types and membership information are obtained from Paper I.

low-mass sample by comparing the number of IR-excess stars in the Megeath et al. (2012) sample and our sample. If we limit ourselves to objects with $A_V < 2$ for 1 to $0.1 M_\odot$, then our spectroscopic sample is about 90% complete. Since we required Li absorption and/or IR-excess for membership, we expect very few contaminants in the low-mass sample. We do note that the completeness is worse for the non-excess objects because we are not able to target them as efficiently. In particular, we are missing non-IR excess objects in the G & K range that are too bright for 6.5m telescopes and as well as the lowest-mass objects because it is more difficult to observe Li absorption in lower S/N spectra. To summarize, we are missing members in the low-mass sample and the incompleteness depends somewhat on the spectral type. However, in Section 4.4, we will explain why this incompleteness does not affect our result as long as we use the lower limit of the number of low-mass stars.

Contamination rather than completeness is the problem for the higher mass objects, and identification of members is more difficult. While we can rule out foreground dwarfs and background giants to some extent based on their position in the color-magnitude diagram, but we will still have non-members in the sample that cannot be ruled out simply by proper motions and/or for which we have no radial velocity measurements. To estimate the possible contamination, we use the Besançon model (Robin et al., 2003) to help us determine the number and type of contaminants we would find along the line of sight in a 3° field toward the direction of L1641.

We first consider the range of O and B stars. Since we are trying to test the IMF variation in this mass range, it is essential that we have a complete sample. This is achieved by our survey of the brightest 2MASS stars, regardless of whether they have IR-excess. We note that because of step (3) in our target selection (see Section 4.2.1), highly embedded O or early B stars would not have been found. However, evolved O or early-B stars would have blown away materials nearby in a manner similar to the B4 star near (RA, Dec) = (5:42:21.3, -08:08:00) and therefore would not have high extinction. (Note that there is another reflection nebula, powered by a potentially massive star further south, outside of the fields of our optical studies.) On the other hand, if there were unevolved, highly-extincted early-B stars, they would heat up the

dust nearby and be identified as bright IR-excess sources by the *Spitzer* survey. We examined the brightest IR-excess sources in the field and confirmed that they are mostly A stars, with one exception being an FU Ori star (V883 Ori), where the IR luminosity is dominated by accretion. We also examined the protostars that have large bolometric luminosities. The most luminous protostar in L1641 is located at (RA, Dec) = (5:40:27.4,-7:27:30) in one of the high-extinction clumps. It has L $\sim$ 490 $L_{\odot}$(Kryukova et al., 2012), and according to the Siess (2000) isochrones, has a mass less than 7 $M_{\odot}$. Because of the short lifetime and relative small number of OB stars, we expect no contamination in this mass range that is at the right distance to appear along the ZAMS at 414 pc. The Besançon model predicts no OB stars in the field within 1 kpc.

For A stars, we expect our survey to be complete to at least $A_{\rm V}$= 2 since we targeted stars that are brighter than B = 15 and B-R < 2.5 in the USNOb catalog. Unfortunately, we do not have echelle observations of the A stars, and are therefore unable to constrain membership rate from radial velocities. We are left with estimating the level of contamination is the Besançon model, which predicts 3 foreground A stars above the region's isochrone and up to 5 background giants. The actual number of background giants that make it into our survey depends on the extinction toward them and is therefore more difficult to constrain. In Table 4.1 and 4.2, we identified 3 A stars as non-members and 9 A stars as members. From the discussion above, we therefore conclude that out of the 9 stars considered members, up to 5 of them can actually be non-members. If we adopt a moderate extinction of $A_{\rm V}$= 2, we expect 3 non-members.

We expect a large number of line of sight contamination for F & G stars. In Section 4.3.3, we determined that only 20% of the observed F & G stars are actual members based on radial velocities. Our sample also suffers from incompleteness in the G star range because of the target selection criteria in our intermediate-mass and low-mass samples tend to miss G stars that are below the 1$M_{\odot}$ line in the J vs. J-H CMD.

As discussed in Paper I, our optical photometric and spectroscopic sample include

stars in the Orion A cloud south of -6°, which we now define as the L1641-all sample. However, within this sample, the northern end is a relatively denser region and has four early-B stars that likely denote the outer regions of the ONC. We therefore further divide the L1641-all sample into subsamples L1641-n (Dec=$-6.5°$ - $-6°$ and L1641-s (Dec< $-6.5°$). Note that this definition is only for the purpose of analysis in this work and does not coincide with the small clusters L1641-North (RA$\sim$ 84.1°, Dec$\sim$ $-6.3°$) and L1641-South (RA$\sim$ 85.7°, Dec$\sim$ $-8.2°$).

4.3.5 HR diagram

We use an HR diagram to determine the ages and masses of L1641 members. We use the effective temperature scale from KH95 for stars earlier than M4 and effective temperatures from Luhman et al. (2003) for stars M4 and later. If the I_C band magnitude is available for a star, we use the following equation to determine the bolometric luminosity:

$$\log(L/L\odot) = 0.4\ [M_{\mathrm{bol},\odot} - (I_C - A_{I_C}) - DM + BC_{I_C}] \tag{4.2}$$

where the bolometric magnitude of the sun $M_{\mathrm{bol},\odot}$ is set to 4.75, A_{I_C} is the extinction at I_C determined by dereddening the the observed $V - I_C$ color and distance modulus is DM = m-M = $5\log_{10}$(d/10pc)= 8.09, assuming that L1641 is at the same distance as the ONC (414 pc; Menten et al. 2007).

If the I_C band magnitude is not available (only the brightest stars), we use a similar equation using the V band magnitude to determine the bolometric luminosity:

$$\log(L/L\odot) = 0.4\ [M_{\mathrm{bol},\odot} - (V - A_V) - DM + BC_V]. \tag{4.3}$$

where A_V is the extinction at V determined by dereddening the B-V color. We use bolometric corrections for the corresponding magnitude band from KH95 for stars earlier than M4 and Bessell (1991) for stars M4 and later. To determine the extinction, we use the V-I_C colors when both bands are available. For the brightest stars where the data is taken from the Tycho2 catalog, the B-V color is used to

estimate the extinction. The intrinsic colors are from KH95 for stars earlier than M4 and Leggett (1992) for stars M4 and later. We then calculate the extinction assuming a standard extinction law with R_V of 3.1 (Cardelli et al., 1989).

Figure 4.8 shows the HR diagram. The black symbols represents stars in L1641-s and the lighter grey symbols are stars in L1641-n (see Section 4.3.4 for the definition of the populations). The 1, 3 and 10Myr Siess et al. (2000) isochrones (Z=0.02, no overshoot) overplotted in red. The thick red line corresponds to the "early main-sequence", defined as the time when the star settles on the main sequence after the CN cycle has reached its equilibrium. In black are the evolutionary tracks for masses from 0.1 to $7M_{\odot}$. We can estimate the ages and masses from the isochrones. We first select data points on the Siess tracks with ages less than 100 Myrs and pre-main sequence or main sequence evolutionary phase. We then use the IDL programs *TRIANGULATE* and *TRIGRID* to interpolate between the evolutionary tracks to obtain the ages and masses. Objects that fall outside of the track area are not assigned masses or ages.

4.3.6 Age and Mass distribution

The top panel of Figure 4.9 shows the age distribution of the members in L1641 estimated from the HR diagram. Only objects with masses below $1M_{\odot}$ are considered in the age estimates because the birthline effect tend to make the highmass objects appear older (see *e.g.* Hartmann 2003). Both the median and the mean of the age distribution is around 6.5, with a standard deviation of 0.3 dex. Therefore, the majority of the low-mass members in L1641 are around $10^{6.5}$ years, consistent with the ages of the ONC. This is the same as the result found in Paper I where we used a more direct age estimate from the V vs. V-I CMD. This ensures that L1641 is still young enough that any early B star, if ever present, would still be on the main sequence and seen in our survey. There is also no evidence of SN bubbles from O stars.

The bottom panel of Figure 4.9 shows the mass distribution of L1641 members in log-log space. Each of the F & G unconfirmed members is considered 0.2 star in the histogram. Note that the mass histogram presented here is not extinction limited

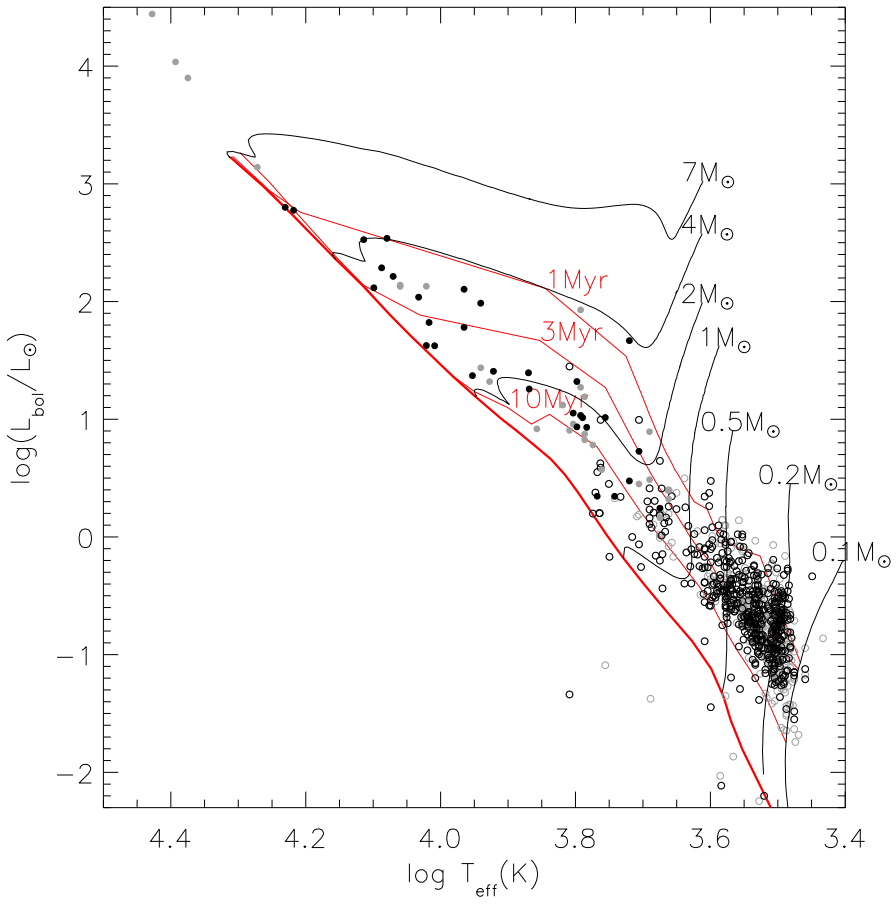

Figure 4.8: HR diagram of members of L1641. The black symbols represents stars in L1641-s and the lighter grey symbols are stars in L1641-n (see Section 4.3.4 for the definition of the populations). The 1, 3 and 10 Myr Siess et al. (2000) isochrones (Z=0.02, no overshoot) overplotted in red. The thick red line corresponds to the "early main-sequence", defined as the time when the star settles on the main sequence after the CN cycle has reached its equilibrium. In black are the evolutionary tracks for masses from 0.1 to $7M_{\odot}$.

and we did not correct for completeness. The dip around 1 $M_{\odot}$ corresponds to the gap between the intermediate-mass sample and the low-mass sample. This figure demonstrates that because of incompleteness and extinction issues, our sample does not allow us to obtain the upper-mass IMF by simply fitting a power-low.

4.4 Comparing L1641 to the ONC

We note that the selection criteria for our spectroscopic observations and when a star in our spectroscopic survey is considered a member is between Paper I and this work and the criteria are spectral type dependent. This is mainly because the youth indicators themselves are spectral-type dependent. As a result, the completeness and contamination rate is also spectral-type dependent. As a result, our sample is not a clean extinction-limited complete sample and we cannot test the form of the IMF via the distribution of spectral types and K-band luminosity. We can only compare the ratio of high-to-low mass objects.

4.4.1 Comparing L1641 and ONC spectral type distributions

The top panel of Figure 4.10 shows the spectral type distribution of the extinction limited sample ($A_{\rm V} \leq 2$) in L1641 and in the ONC. The solid line shows the spectral type distribution of L1641 members with $A_{\rm V} \leq 2$. We first remove the objects that are identified as non-members, and then we scale the F & G stars whose membership status is uncertain by 20%, based on the MIKE observations indicating that only 20% of them are actual members. The dashed line shows the spectral type distribution of ONC members from H97 with $A_{\rm V} \leq 2$ and membership probability $> 70\%$, scaled to the same number of stars as L1641.

The bottom panel is the same, but shows only stars in L1641-s. We can see that L1641, especially the southern part is deficient in stars earlier than B4 compared to the ONC. We also note that L1641 has a smaller number of late G and early K stars compared to the ONC. This is because we are missing some late G and early K stars from our target selection (see Section 4.2.1). Other than the missing members in this range, the low-mass end of the distribution look fairly similar.

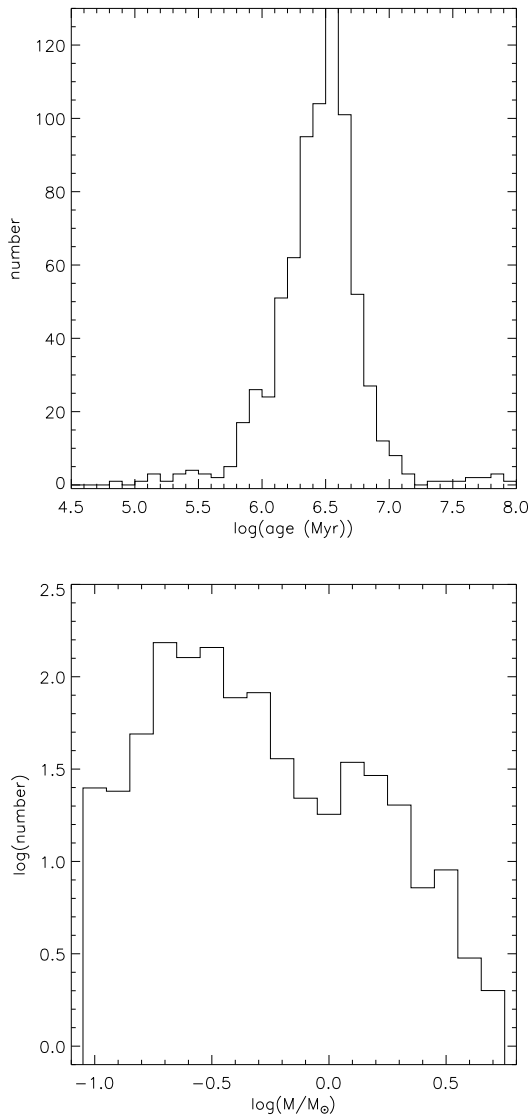

Figure 4.9: Top panel: Age distribution of objects with masses below $1M_{\odot}$as inferred from the Siess et al. (2000) isochrones. We only consider objects with masses below $1M_{\odot}$in the age estimates because the birthline effect tend to make the highmass objects appear older and the low-mass objects give a more reliable age estimate of the population. Bottom panel: Mass distribution of all the members.

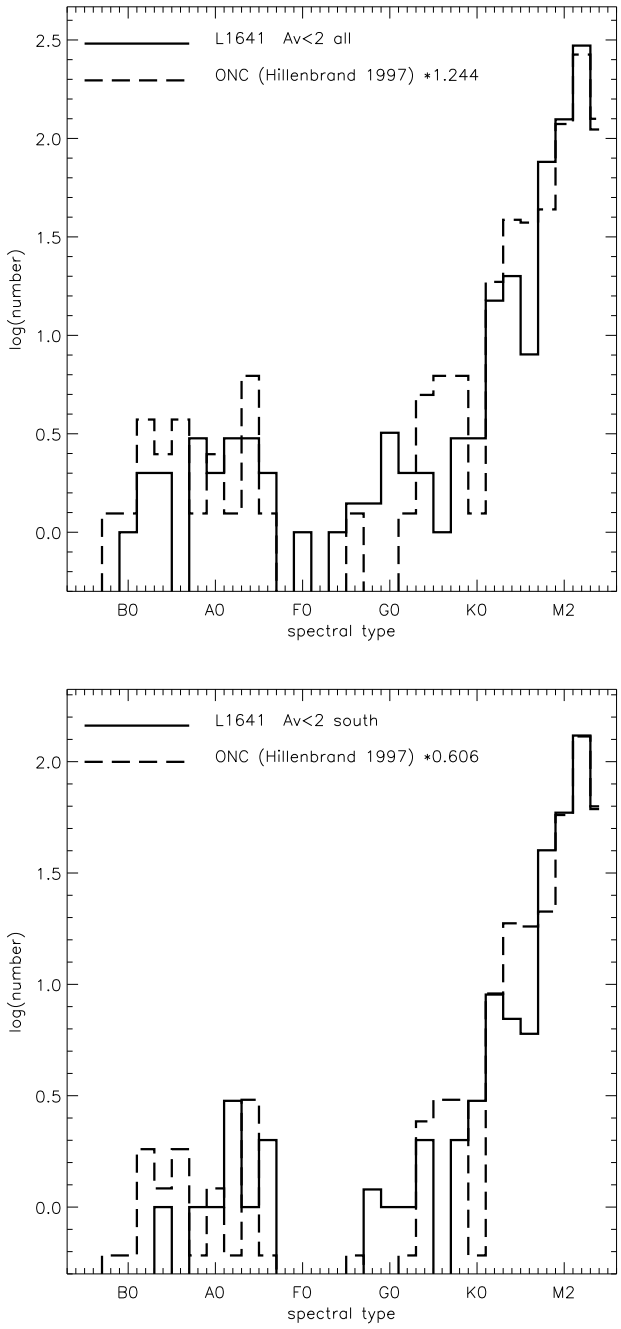

Figure 4.10: Left: Histogram of spectral type distribution of the extinction limited sample ($A_V \leq 2$) in L1641-all (solid line) and in the ONC (dashed line). Right: Same as top figure, but only considering stars in L1641-s. The ONC population is scaled to match the size of the L1641 population, and the bins with only one star gives a negative value after scaling by a factor less than 1.

Table 4.3. Number of Stars in Spectral Type Bins

Region	O stars	B0-B3	B4-B9	A stars	F0-M4
ONC (H97)[a]	2	4	7	7	437
L164-all1[b]	0	4	6	8	451
L1641-n[b]	0	4	3	2	238
L1641-s[b]	0	0	3	6	213

[a]Only stars with $A_V \leq 2$ and membership probability $> 70\%$ are considered.

[b]Only stars with $A_V \leq 2$ are considered.

In Paper I, we found that the IMF of L1641-s is inconsistent with the standard IMF models. Compared to both Chabrier (2005) and Kroupa (2001) IMFs, the L1641 is deficient in O and early B stars to a 3-4σ significance level. Here we discuss whether the ratio of high mass to low mass stars is different in L1641 and the ONC. However, instead of comparing the derived masses, a model dependent quantity, we choose to compare the directly-observable spectral types.

We then use the Fisher's exact test (Fisher, 1925) to find the significance level of the ratios between high-mass and low-mass stars in different regions of L1641 and the ONC. Since we are interested in whether the ONC has a higher frequency of high-mass stars, we use the one-sided test and do not compute the P value when the ONC has a lower frequency in the high-mass bin. The results are summarized in Table 4.4. In general, when the entire L1641 population or the northern region is considered, the frequency of high-mass stars is consistent to that in the ONC. In the L1641-s region, there is some evidence that the high-mass IMF could be different, especially when we consider the ratio of (O to B3 stars) to (B4 to M4 stars), where the significance level is 0.092. The difference in the high-mass IMF is suggestive but not conclusive, mainly due to the small number of early-type stars in both samples.

Table 4.4. Significance Level of Fisher's Exact Test on the Ratio of High-mass to Low-mass Stars in the ONC and L1641

Compared Regions	O stars/B0-M4	O-B3/B4-M4	O-B9/A0-M4
ONC[a]& L1641-all[b]	0.243	0.360	0.314
ONC[a]& L1641n[b]	0.421	···	0.599
ONC[a]& L1641s[b]	0.452	0.092	0.176

[a]Only stars with $A_V \leq 2$ and membership probability $> 70\%$ are considered. Data taken from H97.

[b]Only stars with $A_V \leq 2$ are considered.

Table 4.5. Number of Stars in K_s-magnitude Bins

Region	$K_s < 7$	$7 < K_s < 8$	$8 < K_s < 9$	$9 < K_s < 12$
ONC (Muench et al. (2002))	8	10	29	397
L1641-all	4	10	23	518
L1641-n	3	2	6	170
L1641-s	1	8	17	348

Table 4.6. Significance Level of Fisher's Exact Test on the Ratio of High-mass to Low-mass Stars in the ONC and L1641

Compared Regions	$K_s < 7$ / $7 < K_s < 12$	$K_s < 8$ / $8 < K_s < 12$	$K_s < 9$ / $9 < K_s < 12$
ONC[a]& L1641-all	0.103	0.118	0.018
ONC[a]& L1641-n	0.600	0.302	0.050
ONC[a]& L1641-s	0.034	0.131	0.044

[a]Data taken from Muench et al. (2002).

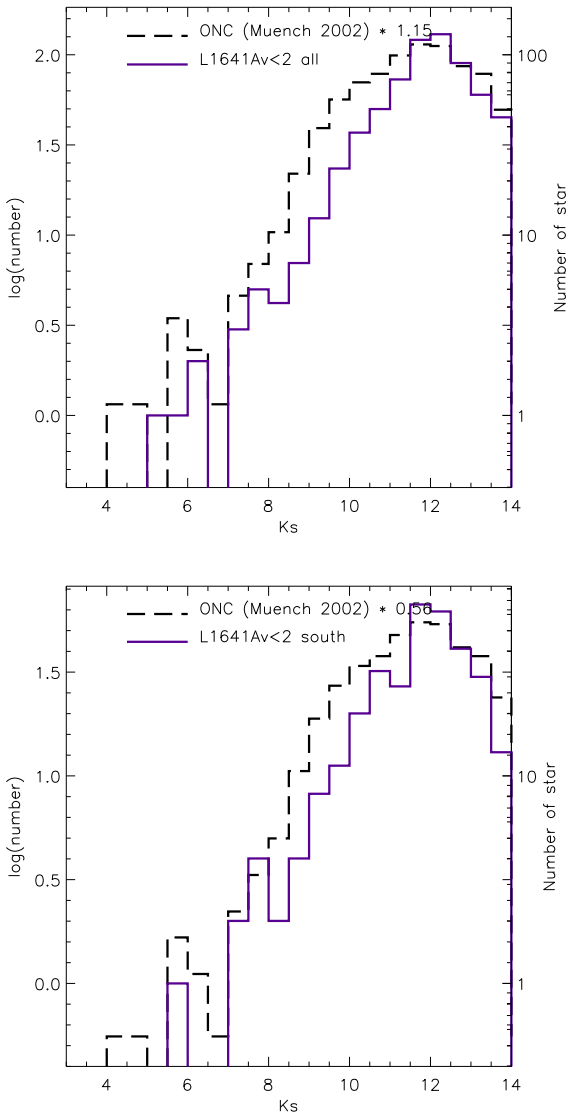

Figure 4.11: K-band luminosity function (KLF) of extinction limited L1641 sample. Top: objects in L1641-all. Bottom: only objects in L1641-s. In both figures, the black long dashed lines represent the KLF of the Trapezium from (Muench et al., 2002). The solid purple lines represent the KLF of objects in L1641.

4.4.2 Comparing the L1641 and ONC K-band luminosity functions

Next we compare the K-band luminosity function (KLF) of L1641 to that of the central regions of the ONC (the Trapezium cluster) (Muench et al., 2002).

Table 4.5 lists the number of observed stars in the Trapezium and confirmed members of L1641 in each magnitude bin, including objects that have extinction higher than $A_V = 2$ from our optical survey as well as objects that are too extincted in the optical and are identified by IR-excess only. The study of Muench et al. (2002) covered the central $5' \times 5'$of the Trapezium and it is safe to assume that in the magnitude range of our interest (K_s brighter than12), the line-of-sight contamination is very small and can be ignored. In L1641, since the field is much larger and the density of stars much lower, the contaminants outnumbers the members and making an off-field correction can lead to large errors. We therefore obtain the number of all known members by adding the spectrally-confirmed members to the highly-extincted IR-excess members. The number of stars in each magnitude bin has varying completeness and is biased against highly-extincted low-mass objects that do not show IR-excess.

Figure 4.11 shows the K-band luminosity function of extinction limited ($A_V \leq 2$) L1641 sample. The top panel shows objects in L1641-all and the bottom panel shows only objects in L1641-s.

We use the one-sided Fisher's exact test to compare the ratios of stars above and below the threshold magnitude. The hypothesis we want to test is that the L1641 has a lower proportion of stars in the high-mass bin compared to the Trapezium. We use cutoff magnitudes of K_s=7 and 8 to ensure that we are not missing members in the high-mass (bright) bin. Table 4.6 lists the significance levels of the one-sided Fisher's test. The Trapezium population has a higher fraction of high-mass stars compared to the L1641 population as a whole even though the difference is not very significant. The L1641-s population has a significantly lower fraction of high-mass stars compared to the Trapezium, with a P value of 3%.

The KLF has the advantage of being minimally affected by extinction (the extinction in K band is about one tenth of the extinction in the V band). The KLF

can also be affected by disk-excess. (Muench et al., 2002) constructed the K-band IR excess distribution function for the Trapezium, where the K band excess peaks near 0.2 with a mean of 0.4 mag. Even though disk-excess can change the shape of the KLF, this excess does not significantly affect our number counts in Table 4.5 because of our coarse binning as well as the fact that most of the brightest objects are diskless. In addition, since L1641 and the ONC has similar ages, it is reasonable to assume the disk excess would have similar effects on the L1641 sample and the Trapezium sample.

As mentioned in Section 4.3.4, since we can identify the higher-mass stars through large extinctions and we have a lower limit to the number of the low-mass stars, we are overestimating the ratio of high-to-low mass stars and therefore underestimating the significance of the result. In addition, up to half of the A stars can actually be background objects. If we account for these A stars, the high-mass bin in L1641 would have a smaller number of stars in the $K < 8$ and $K < 9$ cases. Therefore we expect the P value to be even smaller after accounting for A star contamination.

4.5 Discussion

4.5.1 M_{ecl} - m_{max} relation in Orion A

Weidner & Kroupa (2006) and Weidner et al. (2010) compiled a list of Galactic clusters and propose a relation between the most massive star (m_{max}) in a cluster and the cluster mass (M_{ecl}). Bonnell et al. (2004) also proposed a similar relation based on simulations of competitive accretion simulations.In their simulations, the most massive star tends to form in the center of a cluster and gains the majority of its mass from the infalling gas onto the cluster, which is accompanied by newly formed low mass stars. Therefore, the formation of the high-mass stars correlates with high stellar surface density. Similarly, Elmegreen (2004) also suggested that high mass stars can be formed from gravitational focused gas accretion in high-density clouds and therefore explain the steep IMF in the field. The Weidner & Kroupa (2006) and Bonnell et al. (2004) M_{ecl} - m_{max} relations are almost identical for clusters up to a

few thousand $M_\odot$, which suggests that, even though the authors did not explicitly quantify such a relation, the upper-mass IMF should also depend on the density. Therefore, qualitatively speaking, the M_{ecl} - m_{max} relation is compatible with the environmental density dependence we find in Orion A.

Quantitatively, whether L1641 follows this M_{ecl} - m_{max} relation is less clear and depends on what we define as a cluster. If we consider L1641-s as a whole, its most massive star has a smaller mass than what is expected from the M_{ecl} - m_{max} relation. The L1641-s has a total stellar mass of $\sim$1000$M_\odot$, but the most massive star is only $\sim$7$M_\odot$. However, if we consider the denser grouping of tens of stars in L1641 individually, it would be consistent with the M_{ecl} - m_{max} relation found by Weidner & Kroupa (2006).

4.5.2 Challenges in studying the density dependence of the IMF

Despite the apparent deficiency of high-mass stars in low-density regions, there are few conclusive results that demonstrate the IMF in low-density regions is different from that of clusters. Comparing the upper-mass IMF in a low-density star-forming region is difficult for many reasons, including the small number of high-mass stars intrinsic to the shape of the IMF, the significant line-of-sight contamination and the potentially different completeness in regions of different density.

In this work, we compared the largest nearby low-density and clustered star-forming regions and found moderately significant results. On one hand, this confirms that the IMF is not vastly different in regions of different density; on the other hand, the significance could be increased by deeper studies of the extincted population. We have chosen NOT to use an estimate of the significance that would be achieved if we made any correction for incompleteness in the extincted low-mass population to be conservative. Further study on the fainter members could make our result even stronger. In addition, a complete radial velocity survey of the AFG stars would be useful to test IMF differences down to lower masses.

4.6 Conclusions

We conducted a survey of the intermediate-mass stars in L1641, the lower-density star-forming region south of the ONC, aimed at testing whether the apparent deficiency of high-mass stars in low-density regions is statistically significant. This study complements the low-mass survey presented in Paper I by adding 57 stars in the range of B4 to K4.

In Paper I, we found that the lack of O and early B stars in L1641 is inconsistent with the Kroupa (2001) and Chabrier (2005) IMFs. In this work, our sample of intermediate-mass stars improves our ability to compare directly the ratio of low-mass stars to high-mass stars with the ONC. In particular, we use Fisher's exact test to compare the spectral type distribution of L1641 to that of the ONC from Hillenbrand (1997) and the K-band luminosity function of L1641 directly to those in the central region of the ONC, the Trapezium (Muench et al., 2002). The tests indicate a probability of only 3% that the ONC and the southern region of L1641 (Dec<-6.5) were drawn from the same population, supporting the hypothesis that the upper mass end of the IMF is dependent on environmental density.

CHAPTER 5

H & K Band Spectroscopy of Embedded Young Stellar Objects in L1641

5.1 Introduction

The L1641 is a low-density star-forming region in the lower part of the Orion A molecular cloud, south of the Orion Nebula Cluster (ONC) region (see Allen & Davis (2008) for a discussion of the individual clouds in L1641). It is at roughly the same distance as the ONC ($\sim$ 414pc; Menten et al. 2007; Kim et al. 2008), as the lower part of the Orion A cloud is contiguous with the ONC region. Based on the recent *Spitzer/IRAC* survey of infrared-excess stars (Megeath et al., 2012) and optical survey of pre-main sequence stars (Hsu et al., 2012), L1641 contains a much larger pre-main sequence population than other nearby low-density regions such as Taurus-Auriga (see, e.g Luhman et al. 2009; Rebull et al. 2011).

We have conducted optical photometric and spectroscopic surveys in L1641, the distributed star-forming region south of the Orion Nebula Cluster to characterize its population of young stellar objects (YSOs) (Hsu et al., 2012, 2013). We characterized $\sim$ 900 optically visible young stellar objects, allowing us characterize the age and distribution of masses. We found evidence that this low-density star-forming region has a lower frequency of high-mass stars compared to the ONC and the standard Chabrier (2005) and Kroupa (2001) IMFs.

A significant fraction of the YSO population in L1641 is too extincted for our optical survey, including most of the protostars and half of the class II's. Most of these highly-extincted objects are in small groups along the main ridge of high gas density. We therefore used MMIRS, the MMT and Magellan Infrared Spectrograph

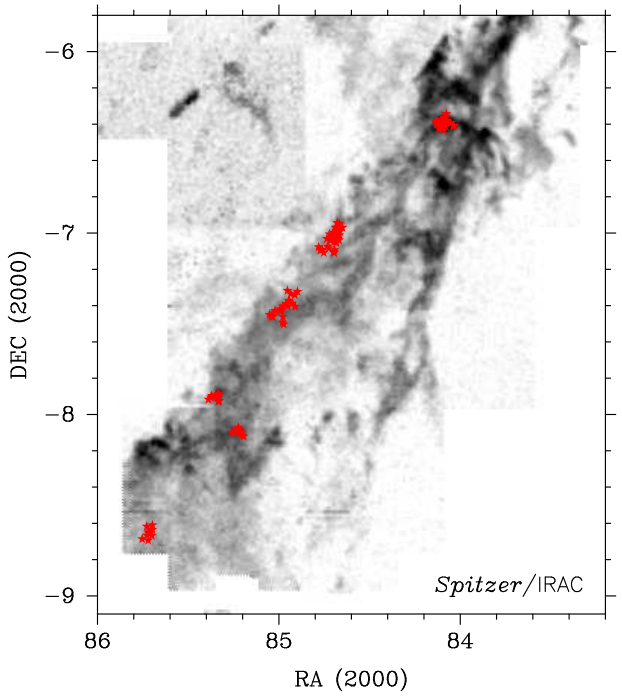

Figure 5.1: Positions of targets observed with MMIRS overlaid on the ^{13}CO map from Bally et al. (1987).

on the Magellan Clay telescope McLeod et al. (2012) to obtain multi-object, H & K band spectra of the small groups of embedded objects to characterize, when possible, their spectral types and other properties.

In Section 5.2, we describe the target selection, observations and data reduction. In Section 5.3 we describe and compare the methods used to determine the spectral types of the objects. In Section 5.4, we estimate the accretion rates through the hydrogen recombination lines. Finally, we present our conclusions in Section 5.5.

5.2 Data

5.2.1 Sample Selection

The L1641 cloud subtends 1° by 3° on the sky and MMIRS has a small field of view of 4 by 6.9 arcmin. We therefore only focused on the dense groups with the highest number of embedded YSOs. We selected our targets from the IR excess source catalogued by Megeath et al. (2012) and prioritized our target list based on

their H & K band magnitudes from 2MASS (Skrutskie et al., 2006). Within each field, we gave the highest priority to IR-excess stars that are brighter than 13th magnitude in both H & K band. Lower priorities were then given to fainter stars. Each of our 11 fields contain 10 to 15 targets. Figure 5.1 shows the positions of the targets overlaid on the ^{13}CO map. The targets were usually chosen from the densest region of the L1641 cloud, where the extinction is high and the density of YSOs with IR-excess is high. We observed 115 YSOs, including 27 class I (protostars) and 88 class II (pre-main sequence star with disk). Table 5.1 lists the basic information of the targets, including positions, YSO classification (protostars or disks), 2MASS magnitudes and the dates of observation. Figure 5.2 shows the J - H vs. H-K colors of objects observed. The objects with optical spectral type from Hsu et al. (2012) are shown in blue squares. The objects with and without IR spectral types are shown as red filled and open points, respectively. The solid curves show the intrinsic colors of main sequence and the giant branch (Bessell & Brett, 1988) and the dashed lines show the direction of extinction with extinction law from Cardelli et al. (1989) for $R_V = 3.1$, and the asterisks mark A_V of 5 increments. We also use Figure 5.2 to find the extinction needed to bring the stars onto the CTTS locus (Meyer et al., 1997), assuming all the stars are K7 stars (which is generally not a bad assumption for our targets).

5.2.2 Observations

The observations were taken with MMIRS, the MMT and Magellan Infrared Spectrograph on the Magellan Clay telescope (McLeod et al., 2012). MMIRS is a wide-field near-IR spectrograph with a field of view of 4 by 6.9′. We used the HK band grism with 0″.4 slits, which yielded a resolution of R = 1200. The wavelength coverage of the HK band grism was 1.25 μmto 2.4 μm, but some targets had a slightly smaller wavelength coverage due to their locations on the mask. The observations took place on 10/23/2010, 10/24/2010 and 03/14/2012 - 03/16/2012 (UT date at the beginning of the night). Because the sky background in the near-IR can change on timescales of a few minutes, we took short observations of 3 minutes each, with 3 and 2 dithering

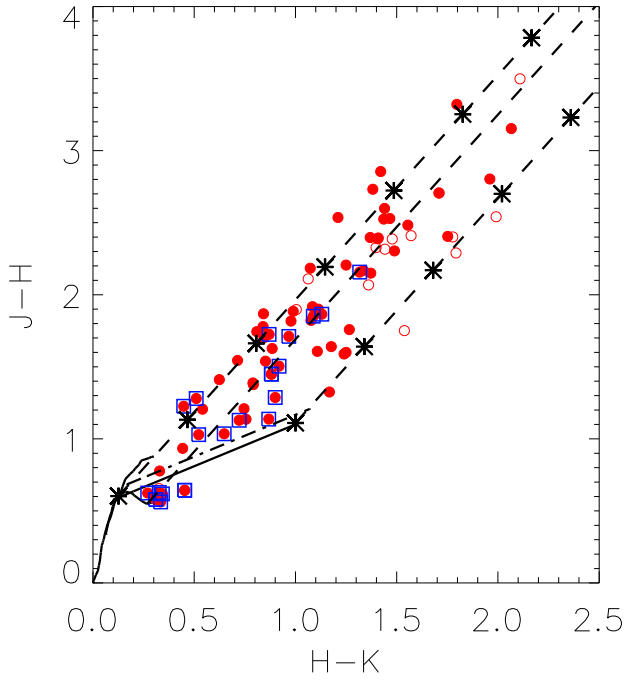

Figure 5.2: J - H vs. H-K colors of objects observed. The solid red circles are the objects that we have spectral-typed based on the shape of the water vapor band and the open red circles are the objects that we have NIR spectra but were unable to spectral type. The blue boxes mark the objects that have optical spectral types.

positions along the slit, for the first and second observing runs, respectively. We used up-the-ramp sampling with 5 seconds increments. Each target field was observed for 45 - 60 minutes. The airmass ranged between 1.1 - 1.9 for all our target observations. Between each field, we observed an argon comparison lamp for wavelength calibration, bright continuum lamp for flat-field calibration. To correct for telluric absorption, we observed a bright G0 star (A0 star in the second run) between the fields with airmasses similar to the targets. At the end of each night, dark frames were taken with the same exposure setting as the other frames.

5.2.3 Data Reduction

We follow the guidelines of data reduction outlined in the MMIRS cookbook[1]. Every image taken in up-the-ramp sampling mode is first pre-processed into one image with one value per pixel. The pre-processing program also rejects cosmic ray and corrects for non-linearity. We then correct all the science, telluric and flat frames for dark currents. To remove most of the sky emission, we subtract science image pairs from each other. We then used COSMOS, the Carnegie Observatories System for MultiObject Spectroscopy, to obtain an image of each slit and map the pixels on the CCD to wavelengths, using map solutions obtained from the comparison lamps. This allows us to separate each object and obtain wavelength corrected single object spectra. We then apply spectroscopic flat field correction to our science and telluric frames. We then used the IRAF *apextract* package to extract the 1-d spectra from the 2-d spectra. The telluric standard frames are treated the same way as the science data, which gives us a multiplication of the intrinsic spectrum of the telluric standards and the telluric absorption features. We then divide the telluric spectra by the template spectrum of the same spectral type from the IRTF Spectral Library for the G stars (Rayner et al., 2009)[2] and from the theoretical Vega spectrum from the 1993 Kurucz models (convolved to the resolution of our data) to single out the atmospheric

[1]MMIRS cookbook: `http://hopper.si.edu/wiki/mmti/MMTI/MMIRS/MMIRS+Pipeline`

[2]The IRTF Spectral Library: `http://irtfweb.ifa.hawaii.edu/~spex/IRTF_Spectral_Library/`

absorption. Finally, we input the science spectrum and the atmospheric absorption spectrum into the IRAF *telluric* package to correct the science data with atmospheric absorption. Finally, telluric corrected spectra from two or three dithering positions are combined to form the final spectra.

5.3 Spectral Types

Due to the moderate spectral resolution and S/N of our spectra, our ability to detect and measure equivalent widths of weak lines is very limited. As a result, it is not possible to determine the spectral types by modeling the equivalent widths of a large number of lines. We first note that we THdid not find any object with hydrogen lines in absorption, indicative of spectral types of G or earlier. Therefore all the stars we observed are K or later-type stars, with a small chance of having G type stars with accretion rate high enough to fill in the hydrogen absorption lines. For the M type stars, the shape of the water vapor band can be used as a crude alternative used to determine the spectral type. We use the low-resolution IR spectra of members of the TW Hya Association (K. Luhman, personal communication) as water vapor band templates, which have spectral types of K7, M0, M1, M2.5, M3.5 and M5.25. We first inspected each spectrum to look for features of the water vapor bands (a bump in the H band near 1.65 μm). For the stars that show water vapor band features, we first corrected for extinction using values estimated by their locations on the J-H vs. H-K CMD. We then divided the spectra by each of the templates to find the closest match. In general, we were able to find one or two best matches for each target and rule out the rest. Figure 5.3 shows some examples of spectra and spectral types that were assigned. 77 M type stars are spectral typed. 23 of them lie in less extincted regions, where we obtained optical spectral types with IMACS on Magellan or Hectospec on the MMT (Hsu et al., 2012). We use these 23 targets to check the reliability of the IR spectral types. Figure 5.4 shows the comparison of the spectral types obtained from the water vapor bands and the spectral type from optical absorption lines from Hsu et al. (2012). Our spectral typing errors are within 2 -3 subtypes in most cases, with the only exception being a highly veiled star, whose optical spectral type is

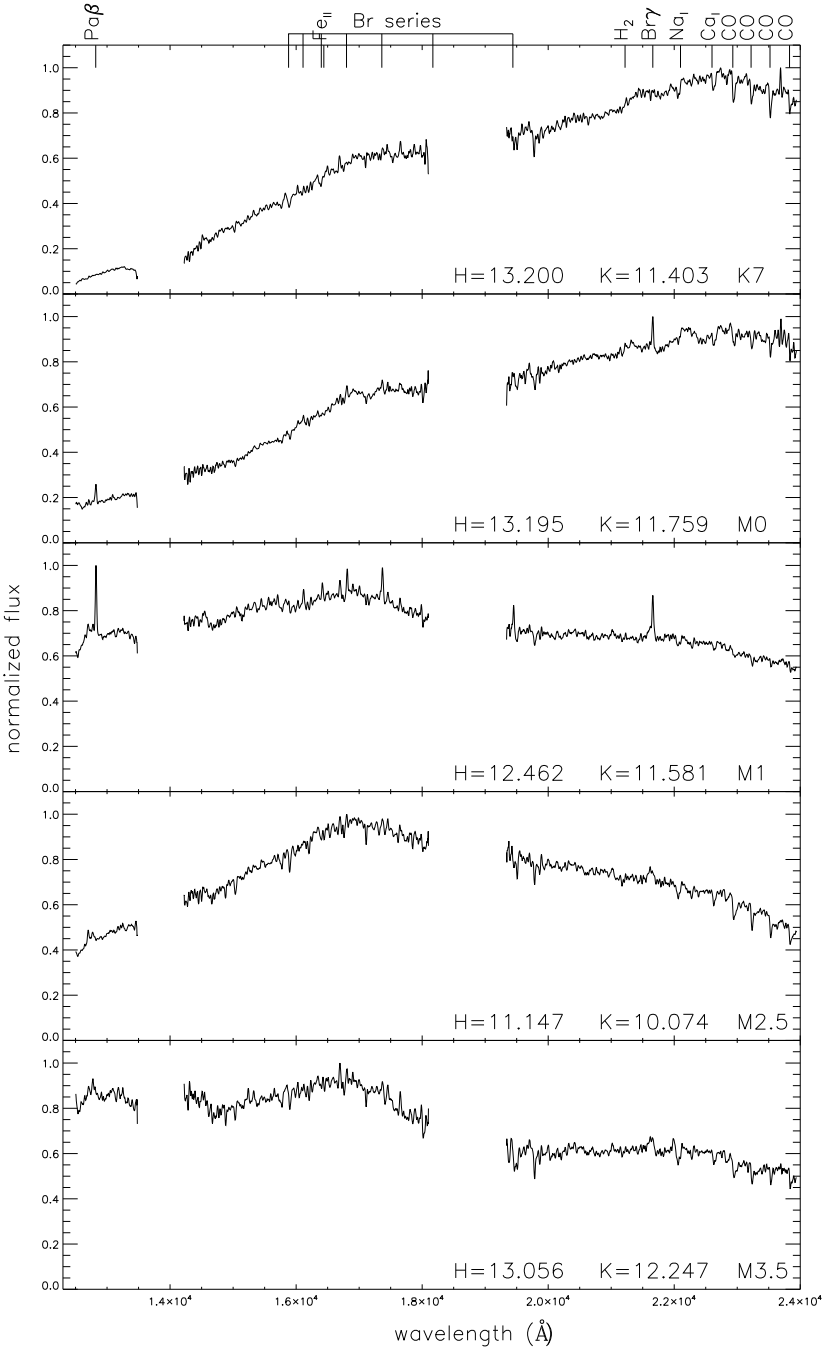

Figure 5.3: Examples of spectra obtained with MMIRS and their assigned spectral types. The wavelengths of prominent absorption and emission lines are marked at the top. The last four panels show spectra that we are unable to spectral-type.

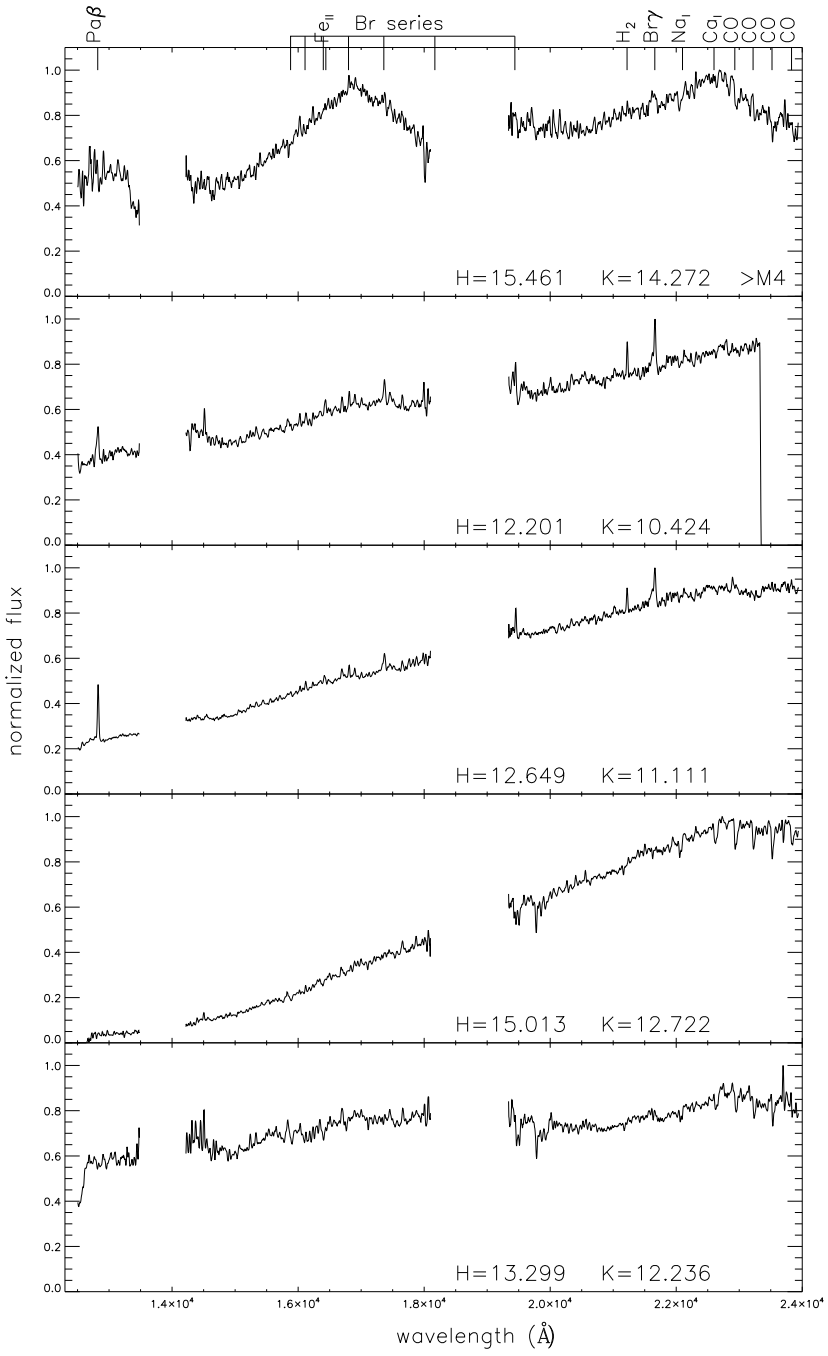

Figure 5.3: (Continued)

less reliable (marked in asterisk in Figure 5.4). Even though the water vapor bands method can only be used in M type stars and is a crude estimate of the spectral type, it is our best estimate given the quality of our data.

Figure 5.5 compares the extinction estimated from near-IR J-H vs. H-K diagram(Figure 5.2 to that from optical spectral type and V-I color excess (Hsu et al., 2012). This demonstrate that the extinction estimates from J-H vs. H-K has large uncertainties. The group of stars with zero $A_V$is likely late M type stars that lie below the CTTS in Figure 5.2. There are also a few stars where the extinction estimated from NIR colors is much higher than the extinction estimated from the optical. This can be due to having more than one star along the line of sight in the crowded regions or that the scattered light makes the optical color bluer and therefore the optical extinction is underestimated.

Besides the water vapor absorption features, the CO bands are one of the most prominent features that we could detect with good precision. Connelley & Greene (2010) found that in the case of low accretion rates, the CO features are dominated by the photospheric absorption and the equivalent widths correlate well with the spectral types. However, even in objects with low accretion, the scatter is too large for CO to be useful in spectral typing. CO emission from the disk and veiling from excess continuum emission become important for objects with higher accretion rates, making CO even less correlated with spectral type.

5.3.1 HR Diagram

For the M type stars that we can determine spectral type through water vapor bands, we derive their effective temperature and bolometric luminosity to place them on the HR diagram (Figure 5.6). The red stars show the protostars whereas the blue stars show the disk objects. The effective temperature scale is from KH95 for stars earlier than M4 and Luhman et al. (2003) for stars M4 and later. The bolometric luminosity is determined from the 2MASS J magnitude. The J band bolometric correction is calculated from KH95 for stars earlier than M4 and Bessell (1991) for stars M4 and later. For comparison, objects with optical spectra from Hsu et al. (2013) are also

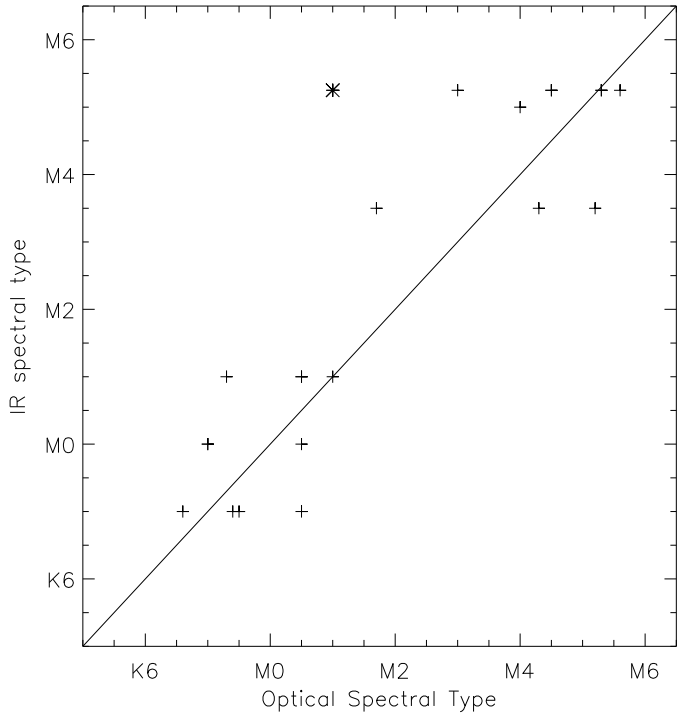

Figure 5.4: Comparison of the spectral types obtained from the water vapor bands and the spectral type from optical absorption lines from Hsu et al. (2012). The spectral types generally agree with each other to within 2 subtypes. The only exception is a highly veiled star (marked by an asterisk) where the errors for spectral typing is larger.

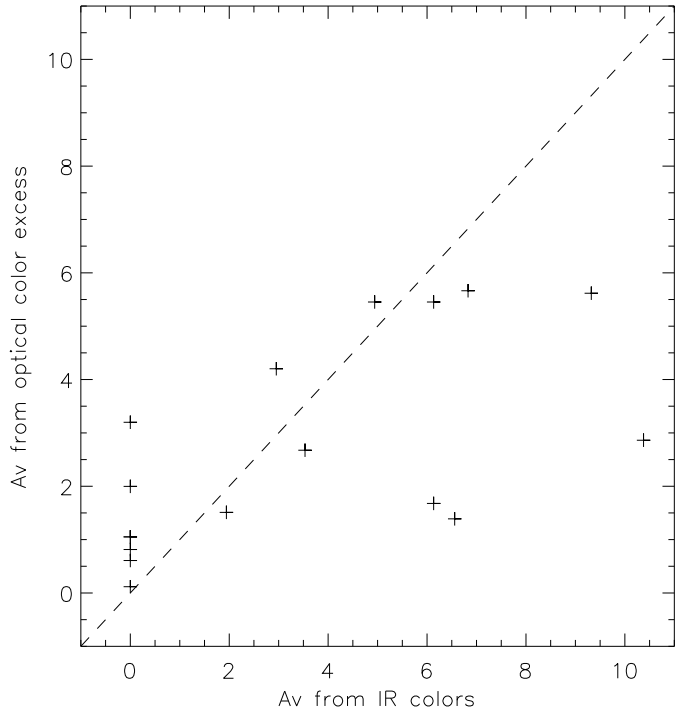

Figure 5.5: Comparison of the extinction estimated from optical spectral type and V-I color excess (Hsu et al., 2012) and from near-IR J-H vs. H-K diagram(Figure 5.2. The group of stars with zero $A_V$is likely late M type stars that lie below the CTTS in Figure 5.2. There are also a few stars where the extinction estimated from NIR colors is much higher than the extinction estimated from the optical.

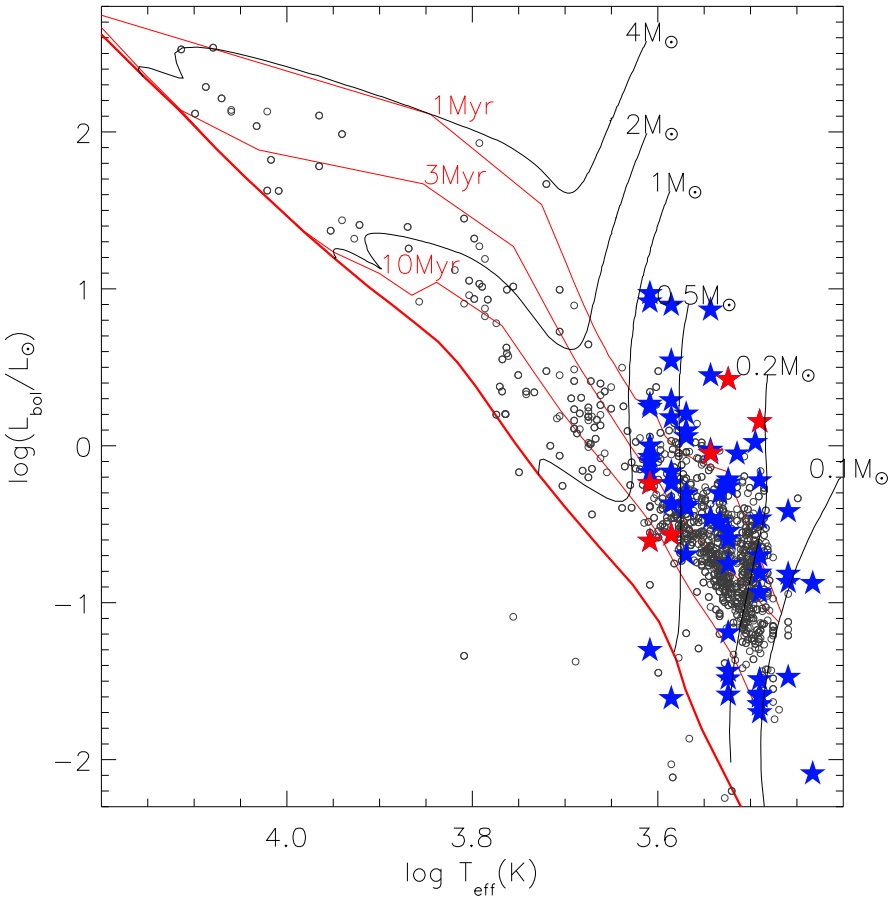

Figure 5.6: HR diagram showing the objects observed and spectral typed with MMIRS (red stars) and objects with optical spectra from Hsu et al. (2013). The effective temperature scale is from KH95 for stars earlier than M4 and Luhman et al. (2003) for stars M4 and later. The bolometric luminosity is determined from the 2MASS J magnitude. The J band bolometric correction is calculated from KH95 for stars earlier than M4 and Bessell (1991) for stars M4 and later. The 1, 3 and 10 Myr Siess et al. (2000) isochrones (Z=0.02, no overshoot) overplotted in red. The thick red line corresponds to the "early main-sequence", defined as the time when the star settles on the main sequence after the CN cycle has reached its equilibrium. In black are the evolutionary tracks for masses from 0.1 to 7$M_{\odot}$.

shown. Note that the bolometric luminosities for the optical sample come from their V or I magnitudes. The 1, 3 and 10 Myr Siess et al. (2000) isochrones (Z=0.02, no overshoot) are overplotted in red. The thick red line corresponds to the "early main-sequence", defined as the time when the star settles on the main sequence after the CN cycle has reached its equilibrium. In black are the evolutionary tracks for masses from 0.1 to $7M_{\odot}$. We note that the MMIRS sample stars all have low effective temperature as we can only classify M stars. There is a large scatter in the bolometric luminosity and therefore the estimated age also has a large spread. Overall, the ages of the MMIRS targets are consistent with the optical sample ($\sim$ 3 Myrs) or maybe slightly younger, but a few objects appear significantly brighter than the 3 Myrs isochrone. The large scatter in the luminosities can be due to an intrinsic age difference, variability, error in estimating the extinction and/or error in estimating the spectral type. The errors in estimating extinction is likely the main cause. As shown in Figure 5.5, the extinction estimated from J-H vs. H-K diagram is much higher than that estimated from optical spectral type and V-I color excess. An overestimation in the extinction will lead to an overestimate of bolometric luminosity. For the six protostars, Kryukova et al. (2012) calculated their bolometric luminosities from 2MASS and Spitzer bands. Their luminosities are consistent with what we estimated to within 0.5 dex. Given the uncertainties in the luminosity estimates, the discrepancy is reasonable.

5.4 Accretion Indicators

The Brackett γ and Paschen β emission lines can be used as indicators of accretion as their luminosities correlates with the accretion luminosity (Muzerolle et al., 1998; Calvet et al., 2000, 2004). In the sample of protostars, 4/18 have Paschen β in emission and 18/27 have Brackett γ in emission. (The sample sizes are different because some spectra did not cover the Paschen β line.) In the sample of disk objects, 18/62 have Paschen β in emission and 20/88 have Paschen β in emission.

Here we adopt the accretion luminosity relation derived for low-mass stars by

Calvet et al. (2000):

$$\log(\frac{L_{acc}}{L_{\odot}}) = 1.03 \log \frac{L_{Pa\beta}}{L_{\odot}} + 2.80 \tag{5.1}$$

$$\log(\frac{L_{acc}}{L_{\odot}}) = 1.20 \log \frac{L_{Br\gamma}}{L_{\odot}} + 4.16 \tag{5.2}$$

For simplicity, we assume that the luminosities of the hydrogen lines only account for a small fraction of their respective 2MASS bands as the 2MASS bands are much wider than the hydrogen lines. We use their 2MASS magnitudes and the zero-magnitude flux Skrutskie et al. (2006) to calculate the flux in at the midpoint wavelength of the band to serve as the continuum flux level at the wavelength of the emission line. We first correct for extinction using the extinction estimates from the near-IR colors (see Table 1). We then derive the luminosity of the hydrogen lines using their equivalent widths and their 2MASS magnitudes. The derived accretion luminosities from both lines are listed in Table 2. Figure 5.7 compares the accretion luminosities derived from Brackett γ and Paschen β lines when both lines are observed. The protostars are shown in red and the disk objects are shown in black. In general, the accretion luminosity estimates from these two lines agree well with each other and the protostars have higher accretion luminosities. The accretion luminosities of the disk objects are on the high end compared to other studies (e.g., Muzerolle et al. 1998; Calvet et al. 2004) mainly because of our limited ability to detect weak hydrogen lines.

5.5 Conclusions

We present MMIRS H & K band spectroscopy of 115 embedded YSOs in L1641, the relatively distributed star-forming south of the Orion Nebula Cluster. The sample includes 27 protostars and 88 disk objects. With 45 - 60 minutes of observation, we obtained S/N $>$ 20 for most of our targets. We found no evidence for heavily-extincted early type stars in our sample. The shape of the water vapor band allows us to obtain spectral-types for 77 M type stars, 54 of which were not previously spectral-typed with optical spectroscopy due to extinction. Comparing IR and optical

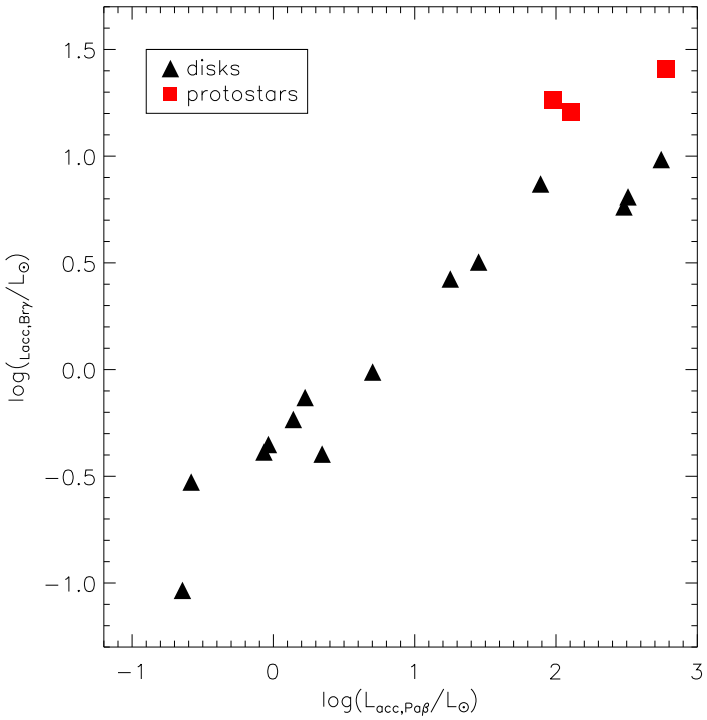

Figure 5.7: Accretion luminosity estimates using two accretion indicators: Paβ (1.282 μm) and Br γ (2.166 μm). The protostars are shown in red squares and the disk objects are shown in black triangles.

Table 5.1. Targets observed with MMIRS

ID	RA (J2000)	Dec (J2000)	class	J[a] (mag)	H[a] (mag)	K_S[a] (mag)	Observed date	S/N	IR type	optical type	A_V
1	84.67867	-6.94465	disk	16.37	14.78	13.54	Oct 23, 2010	16	M5.2	···	5.1
2	84.68720	-6.97072	disk	13.32	11.61	10.65	Oct 23, 2010	21	M1.0	K7.3	9.3
3	84.66866	-6.97269	protostar	12.87	10.58	8.79	Oct 23, 2010	18	···	···	10.8
4	84.66705	-6.98740	disk	12.84	11.55	10.65	Oct 23, 2010	25	M0.0	M0.5	3.5
5	84.66464	-6.99176	protostar	···	15.21	12.91	Oct 23, 2010	13	···	···	···
6	84.72025	-7.00671	disk	13.60	12.06	11.34	Oct 23, 2010	23	M1.0	···	9.0
7	84.70006	-7.01374	protostar	16.11	13.58	12.12	Oct 23, 2010	25	M2.5	···	17.3
8	84.68266	-7.02034	protostar	···	14.70	12.42	Oct 23, 2010	28	···	···	···
9	84.69284	-7.03152	protostar	···	···	13.88	Oct 23, 2010	15	···	···	···
10	84.67274	-7.03125	disk	13.52	12.23	11.73	Oct 23, 2010	31	M3.5	M1.7	6.8
11	84.66915	-7.03998	disk	14.12	13.09	12.57	Oct 23, 2010	28	M5.2	M3.0	3.0
12	84.68663	-7.04639	disk	14.75	12.93	11.96	Oct 23, 2010	33	M3.5	···	10.8
13	84.68318	-7.05264	disk	14.57	12.67	11.56	Oct 23, 2010	31	M5.2	···	10.9
14	84.96104	-7.39179	protostar	14.43	12.03	10.62	Oct 24, 2010	19	M3.5	···	15.7
15	84.95164	-7.40413	disk	16.78	13.62	11.56	Oct 24, 2010	19	K7.0	···	21.4
16	84.97743	-7.40412	protostar	16.56	14.16	12.40	Oct 24, 2010	26	K7.0	···	12.9
17	84.99123	-7.42031	protostar	···	15.51	12.99	Oct 24, 2010	26	···	···	···
18	84.98543	-7.43098	protostar	···	16.24	12.79	Oct 24, 2010	23	···	···	···
19	85.03659	-7.45769	protostar	···	15.76	13.96	Oct 24, 2010	20	···	···	···
20	85.38842	-7.91725	disk	12.21	11.17	10.53	Oct 24, 2010	20	M0.0	K7.0	1.9
21	85.37484	-7.90586	disk	16.86	14.38	12.83	Oct 24, 2010	27	M3.5	···	15.8
22	85.36987	-7.89750	protostar	16.62	14.08	12.09	Oct 24, 2010	28	···	···	12.9
23	85.35296	-7.90235	protostar	···	15.62	12.04	Oct 24, 2010	26	···	···	···
24	85.34986	-7.89499	protostar	···	···	13.44	Oct 24, 2010	18	···	···	···
25	85.33281	-7.92961	protostar	···	···	14.29	Oct 24, 2010	23	···	···	···
26	85.32869	-7.92474	protostar	···	14.91	12.65	Oct 24, 2010	31	···	···	···
27	85.33467	-7.88629	protostar	17.48	14.67	12.71	Oct 24, 2010	37	M0.0	···	17.1
28	85.32956	-7.89373	disk	···	15.43	13.64	Oct 24, 2010	26	M2.5	···	···
29	84.03460	-6.41049	disk	12.70	12.08	11.74	Oct 24, 2010	21	M5.2	M5.6	0.0
30	84.03968	-6.40934	disk	14.64	14.08	13.74	Oct 24, 2010	13	M3.5	M5.2	0.0
31	84.05252	-6.39429	disk	12.74	11.80	11.36	Oct 24, 2010	20	M5.2	···	2.2
32	84.08536	-6.38945	disk	15.22	13.02	11.77	Oct 24, 2010	41	M2.5	···	14.3
33	84.09100	-6.39162	protostar	13.44	11.58	10.45	Oct 24, 2010	32	M5.2	M1.0	10.2
34	84.09355	-6.39573	disk	13.91	12.46	11.58	Oct 24, 2010	38	M1.0	M0.5	6.1
35	84.09826	-6.41432	protostar	···	···	13.27	Oct 24, 2010	17	···	···	···
36	84.10773	-6.41631	protostar	16.44	12.94	10.84	Oct 24, 2010	29	···	···	26.2

spectral types while both are available (23 stars) demonstrates that the IR spectral types generally agree with the optical spectral types to within 2 subtypes. The HR diagram shows that the age of the embedded YSO sample is consistent with the age of the optical sample, with a small number of younger objects. Due to the moderate S/N ratio of our spectra, we were only able to detect the stronger lines. We catalogued the equivalent widths of strong emission and absorption lines found in the spectra, including Paschen β, Brackett γ, H_2, [Fe_{II}], Ca I, Na I, and the CO bands. We use hydrogen recombination lines (Paschen β at 1.28μm and Brackett γ at 2.16μm) to estimate the accretion luminosities. In general, the accretion rates are typical of T Tauri stars, with the protostars have higher luminosities.

Table 5.1 (cont'd)

ID	RA (J2000)	Dec (J2000)	class	J[a] (mag)	H[a] (mag)	K_S[a] (mag)	Observed date	S/N	IR type	optical type	A_V
37	84.11617	-6.42671	disk	12.93	12.31	12.04	Oct 24, 2010	21	M3.5	M4.3	0.0
38	84.12699	-6.39908	disk	15.07	14.49	14.18	Oct 24, 2010	16	M5.2	M4.5	0.0
39	84.13272	-6.38969	disk	14.94	14.30	13.85	Oct 24, 2010	17	M5.2	M5.3	0.0
40	85.22353	-8.07318	disk	16.86	15.25	14.14	Oct 23, 2010	20	M3.5	···	6.5
41	85.25831	-8.10052	protostar	17.03	14.32	12.61	Oct 23, 2010	38	K7.0	···	17.8
42	85.22505	-8.08695	protostar	···	15.24	12.65	Oct 23, 2010	29	···	···	···
43	85.22024	-8.09688	protostar	···	···	14.50	Oct 23, 2010	14	···	···	···
44	85.21070	-8.09686	disk	···	14.38	11.55	Oct 23, 2010	33	···	···	···
45	85.20800	-8.10230	protostar	···	13.61	11.15	Oct 23, 2010	35	···	···	···
46	85.20351	-8.11590	protostar	···	16.40	14.85	Oct 23, 2010	20	···	···	···
47	85.19414	-8.12025	disk	11.93	10.20	9.33	Oct 23, 2010	36	M0.0	K7.0	10.4
48	85.25831	-8.10052	protostar	17.03	14.32	12.61	Oct 23, 2010	38	···	···	17.8
49	84.66669	-6.94953	disk	16.89	15.48	14.86	Mar 14, 2012	39	M7.0	···	7.8
50	84.64970	-6.97101	disk	15.16	13.62	12.77	Mar 14, 2012	45	M5.2	···	7.7
51	84.69672	-7.03149	disk	···	14.56	11.83	Mar 14, 2012	36	···	···	···
52	84.70991	-7.03019	disk	···	16.08	14.48	Mar 14, 2012	32	···	···	···
53	84.71154	-7.03732	disk	···	15.93	13.71	Mar 14, 2012	16	···	···	···
54	84.71823	-7.03717	disk	···	14.01	12.00	Mar 14, 2012	43	···	···	···
55	84.73541	-7.03207	disk	14.73	13.03	12.19	Mar 14, 2012	67	M3.0	···	10.2
56	84.68003	-6.96914	disk	12.05	9.98	8.62	Mar 14, 2012	78	···	···	11.2
57	84.68263	-6.97287	disk	13.53	12.02	11.10	Mar 14, 2012	61	K7.0	K7.5	6.6
58	84.66660	-7.01173	disk	15.47	14.33	13.58	Mar 14, 2012	42	M3.5	···	2.5
59	84.69522	-6.99884	disk	···	16.25	14.88	Mar 14, 2012	15	M2.5	···	···
60	84.70212	-7.00030	disk	16.80	14.49	13.01	Mar 14, 2012	45	M1.0	···	13.7
61	84.68065	-7.02628	disk	14.50	11.97	10.76	Mar 14, 2012	79	K7.0	···	19.6
62	84.69703	-7.01668	disk	···	15.01	12.72	Mar 14, 2012	51	···	···	···
63	84.69047	-7.03292	disk	16.52	13.20	11.40	Mar 14, 2012	54	K7.0	···	26.3
64	84.69479	-7.04702	disk	15.75	13.88	13.04	Mar 14, 2012	56	M1.0	···	12.8
65	84.69390	-7.09374	disk	16.36	13.98	12.50	Mar 14, 2012	43	···	···	15.0
66	84.69584	-7.10908	disk	16.73	15.13	13.88	Mar 14, 2012	8	M0.0	···	5.2
67	84.69886	-7.10410	disk	13.89	12.04	10.95	Mar 14, 2012	59	M1.0	M1.0	10.4
68	84.72488	-7.08352	disk	16.20	14.99	14.45	Mar 14, 2012	11	K7.0	···	5.4
69	84.73122	-7.07480	disk	16.71	14.32	12.92	Mar 14, 2012	39	M3.0	···	15.7
70	84.75261	-7.10834	disk	16.46	13.73	12.34	Mar 14, 2012	58	M0.0	···	21.0
71	84.76069	-7.09275	disk	15.41	13.30	12.24	Mar 14, 2012	62	···	···	14.5
72	84.77180	-7.09500	disk	15.12	12.80	11.40	Mar 14, 2012	75	···	···	14.8

Table 5.1 (cont'd)

ID	RA (J2000)	Dec (J2000)	class	J[a] (mag)	H[a] (mag)	K_S[a] (mag)	Observed date	S/N	IR type	optical type	A_V
73	84.78133	-7.07788	disk	16.48	14.84	13.67	Mar 14, 2012	45	M5.2	···	6.4
74	84.90988	-7.40664	disk	15.52	13.89	13.01	Mar 15, 2012	53	M7.0	···	8.8
75	84.92686	-7.38792	disk	15.72	13.19	11.76	Mar 15, 2012	78	M0.0	···	17.5
76	84.94091	-7.37699	disk	14.44	12.04	10.67	Mar 15, 2012	104	M0.0	···	16.1
77	84.94572	-7.37337	disk	16.84	14.67	13.33	Mar 15, 2012	33	M7.0	···	13.0
78	84.91264	-7.34138	disk	16.36	13.51	12.09	Mar 15, 2012	65	M2.5	···	22.6
79	84.93451	-7.33625	disk	14.37	12.59	11.75	Mar 15, 2012	50	M4.0	···	11.5
80	84.89773	-7.32387	disk	17.29	15.53	14.27	Mar 15, 2012	34	M5.2	···	7.4
81	84.95248	-7.31808	disk	16.72	15.40	14.23	Mar 15, 2012	35	M8.0	···	1.8
82	85.02143	-7.42883	disk	···	15.40	13.48	Mar 15, 2012	18	K7.0	···	···
83	84.99545	-7.42596	disk	14.76	12.35	10.78	Mar 15, 2012	63	···	···	14.6
84	85.05089	-7.45070	disk	14.24	13.03	12.28	Mar 15, 2012	40	M8.0	···	3.7
85	85.04308	-7.46060	disk	12.86	10.97	9.96	Mar 15, 2012	99	···	···	11.8
86	85.03322	-7.46145	disk	···	14.30	12.59	Mar 15, 2012	54	M5.2	···	···
87	84.97805	-7.46224	disk	···	15.14	11.99	Mar 15, 2012	34	···	···	···
88	84.97941	-7.49360	disk	···	15.38	13.48	Mar 15, 2012	24	M7.0	···	···
89	84.97275	-7.50265	disk	···	14.66	12.50	Mar 15, 2012	35	···	···	···
90	84.07695	-6.34408	disk	12.20	11.43	11.10	Mar 16, 2012	47	M1.0	···	0.8
91	84.08756	-6.36476	disk	13.33	11.15	10.07	Mar 16, 2012	46	M2.5	···	15.5
92	84.08115	-6.41052	disk	17.51	14.91	13.47	Mar 16, 2012	38	M2.5	···	18.5
93	84.13272	-6.38969	disk	14.94	14.30	13.85	Mar 16, 2012	19	M5.2	M5.3	0.0
94	84.12699	-6.39908	disk	15.07	14.49	14.18	Mar 16, 2012	41	M5.2	M4.5	0.0
95	84.10880	-6.41437	disk	14.79	14.13	13.81	Mar 16, 2012	31	···	···	0.0
96	84.09088	-6.43386	disk	12.27	11.13	10.26	Mar 16, 2012	55	K7.0	K7.4	1.6
97	84.08578	-6.37108	disk	···	15.46	14.27	Mar 16, 2012	29	M7.0	···	···
98	84.07351	-6.38042	disk	···	15.92	14.54	Mar 16, 2012	18	M3.0	···	···
99	84.07947	-6.38074	disk	14.90	14.28	13.95	Mar 16, 2012	31	M5.2	M8.0	0.0
100	84.10197	-6.37312	disk	12.75	11.52	11.07	Mar 16, 2012	46	M5.0	M4.0	6.6
101	84.08977	-6.38123	disk	14.45	12.29	10.97	Mar 16, 2012	54	K7.0	M0.5	13.0
102	84.09903	-6.38642	disk	14.40	12.65	11.11	Mar 16, 2012	43	···	···	4.9
103	84.09355	-6.39573	disk	13.91	12.46	11.58	Mar 16, 2012	51	M1.0	M0.5	6.1
104	84.12530	-6.38613	disk	12.17	11.04	10.32	Mar 16, 2012	57	K7.0	K6.6	2.7
105	85.69677	-8.61016	protostar	···	15.38	14.17	Mar 16, 2012	21	···	···	···
106	85.72803	-8.61777	disk	15.85	13.96	12.97	Mar 16, 2012	39	M3.5	···	11.7
107	85.75375	-8.68729	disk	···	15.87	14.61	Mar 16, 2012	10	M7.0	···	···
108	85.69736	-8.63573	disk	13.80	11.97	10.90	Mar 16, 2012	36	M1.0	···	10.0

Table 5.1 (cont'd)

ID	RA (J2000)	Dec (J2000)	class	J[a] (mag)	H[a] (mag)	K_S[a] (mag)	Observed date	S/N	IR type	optical type	A_V
109	85.70725	-8.64046	disk	15.26	12.95	11.51	Mar 16, 2012	40	···	···	14.3
110	85.70826	-8.65077	disk	13.74	12.36	11.57	Mar 16, 2012	29	M7.0	···	6.0
111	85.71679	-8.64991	disk	14.80	13.06	12.25	Mar 16, 2012	38	M3.5	···	11.2
112	85.71871	-8.65462	disk	13.23	11.85	11.06	Mar 16, 2012	38	K7.0	···	5.8
113	85.70039	-8.66897	protostar	14.60	12.20	10.42	Mar 16, 2012	28	···	···	12.6
114	85.72806	-8.66653	disk	17.24	15.32	14.24	Mar 16, 2012	11	M3.5	···	11.4
115	85.72037	-8.69477	disk	15.66	13.51	12.14	Mar 16, 2012	37	M0.0	···	12.4

[a]J,H,K_S photometry is from 2MASS

Table 5.2. Equivalent Widths of Emission and Absorption Lines

ID	Pa β	$\log(L_{acc,Pa\beta}/L_\odot)$	Br γ	$\log(L_{acc,Br\gamma}/L_\odot)$	H_2	[Fe II] (1.644Å)	Ca I	Na I	CO (2.293)	CO (2.322)	CO(2.352)
1	···	···	···	···	···	···	0.9	0.6	77.9	···	···
2	-9.5	1.4	-5.3	0.5	···	-0.7	1.7	3.0	3.6	2.5	0.8
3	-16.0	2.4	-2.9	1.3	···	···	1.2	···	···	···	···
4	-26.5	0.3	-8.4	-0.1	···	···	3.4	···	···	···	···
5	···	···	···	···	···	-2.7	1.8	···	···	···	···
6	···	···	···	···	···	···	1.4	5.7	5.4	5.0	7.3
7	···	···	···	···	···	···	3.7	4.4	6.5	3.4	6.3
8	···	···	-1.3	···	···	···	0.7	1.7	1.7	-1.2	1.7
9	···	···	···	···	···	···	3.4	2.8	2.3	4.1	4.8
10	···	···	···	···	···	···	4.6	4.1	6.9	1.9	6.4
11	···	···	···	···	···	···	4.1	3.4	7.0	2.2	5.5
12	···	···	···	···	···	···	1.4	5.1	3.1	3.7	2.7
13	···	···	···	···	···	···	2.0	2.7	5.7	2.6	5.0
14	-12.4	3.1	-6.4	1.5	···	···	1.6	-0.7	1.0	-0.6	-0.2
15	···	···	···	···	-2.1	···	0.6	1.6	37.6	···	···
16	···	···	-5.1	0.1	···	···	3.4	-1.4	-0.3	-3.1	-1.8
17	···	···	-4.0	···	···	···	3.5	1.4	2.0	0.9	2.8
18	···	···	···	···	···	···	4.1	-0.1	4.7	2.1	4.4
19	···	···	-2.5	···	-2.4	···	1.7	1.5	2.9	0.9	2.4
20	-5.9	-0.7	-2.0	-1.0	···	···	3.1	1.7	1.9	-1.9	···
21	···	···	···	···	···	···	1.5	2.6	3.7	1.9	2.3
22	···	···	-2.3	-0.2	···	···	2.5	4.2	0.2	-0.7	20.5
23	···	···	···	···	···	···	0.6	0.9	1.9	-1.9	-0.3
24	···	···	-1.9	···	···	···	2.8	2.2	2.6	···	-1.6
25	···	···	-3.4	···	···	···	0.2	0.8	0.5	-0.9	-3.4
26	···	···	-2.7	···	-4.6	-8.8	-0.7	0.2	-1.0	-3.8	-3.7
27	···	···	-2.7	0.2	···	···	1.0	2.1	2.4	-1.4	···
28	···	···	···	···	···	···	3.2	2.4	5.3	3.1	3.3
29	-1.2	···	···	···	···	···	2.4	1.9	···	···	···
30	-2.7	···	-2.9	···	···	···	6.6	4.2	-14.5	···	···
31	···	···	···	···	···	···	2.6	5.8	5.3	0.6	0.6
32	···	···	-3.1	0.4	···	···	2.3	0.2	3.5	2.1	0.3
33	···	···	-1.9	0.2	···	···	1.2	3.8	0.4	-0.5	-0.4
34	-17.1	0.4	-6.0	-0.4	···	···	2.3	-0.7	1.3	-0.7	0.2
35	···	···	···	···	···	···	-0.2	1.9	5.2	-0.7	-0.9
36	···	···	-1.9	2.3	···	···	1.3	1.2	2.8	-0.2	0.3
37	···	···	···	···	···	···	5.2	3.2	4.7	2.9	···

Table 5.2 (cont'd)

ID	Pa β	$\log(L_{acc,Pa\beta}/L_\odot)$	Br γ	$\log(L_{acc,Br\gamma}/L_\odot)$	H_2	[Fe II] (1.644Å)	Ca I	Na I	CO (2.293)	CO (2.322)	CO(2.352)
38	···	···	···	···	···	···	5.9	2.2	6.3	4.0	-5.4
39	···	···	···	···	···	-1.9	3.2	-0.5	5.5	-3.3	-0.2
40	···	···	···	···	···	···	3.6	1.0	2.6	···	···
41	···	···	-2.5	0.3	···	···	0.3	1.5	2.1	0.4	1.1
42	···	···	···	···	···	···	0.5	2.8	4.1	3.9	1.2
43	···	···	···	···	···	···	6.0	5.2	6.4	7.6	3.6
44	···	···	-2.4	···	···	···	1.8	2.0	4.9	···	···
45	-8.2	···	-5.6	···	···	···	0.9	0.5	2.5	63.3	···
46	···	···	···	···	-183.0	-35.0	3.1	7.9	-13.9	-11.0	30.1
47	···	···	···	···	···	···	2.7	3.0	···	···	···
48	···	···	-2.5	0.3	···	···	0.3	1.5	2.1	0.4	1.1
49	···	···	···	···	···	···	2.3	-1.0	6.8	4.4	5.0
50	···	···	···	···	···	···	2.4	2.3	5.7	3.8	5.5
51	···	···	···	···	···	···	-1.9	-0.6	-0.7	-1.0	-1.0
52	···	···	···	···	···	···	2.6	2.9	4.0	5.2	6.9
53	···	···	···	···	19.2	···	4.7	6.4	4.8	5.3	-2.9
54	···	···	···	···	···	···	3.1	2.7	8.1	4.9	3.6
55	···	···	···	···	···	···	2.7	3.4	5.2	4.4	5.6
56	···	···	-4.3	1.7	···	···	-0.0	1.1	0.2	0.5	0.1
57	···	···	-2.2	-0.6	···	···	2.6	2.4	3.1	2.9	3.9
58	···	···	···	···	···	···	-0.1	1.2	4.7	3.2	4.3
59	···	···	···	···	···	···	8.5	1.5	8.6	-5.6	2.2
60	···	···	···	···	···	···	1.9	1.5	4.2	2.2	3.6
61	···	···	···	···	···	···	2.3	3.3	3.6	3.1	1.9
62	···	···	···	···	···	···	3.0	4.4	5.7	4.2	5.6
63	···	···	···	···	···	···	2.7	3.3	4.9	4.3	6.1
64	···	···	···	···	···	···	3.1	4.8	5.6	3.1	3.7
65	···	···	···	···	···	···	-2.3	-0.2	2.4	1.2	3.0
66	···	···	···	···	···	···	···	···	···	···	···
67	···	···	···	···	···	···	2.2	···	···	···	···
68	···	···	···	···	···	···	3.6	-1.2	11.2	13.2	21.4
69	···	···	···	···	···	···	2.1	3.0	5.9	3.6	5.4
70	···	···	···	···	···	···	2.8	···	···	···	···
71	···	···	···	···	···	···	2.4	3.8	4.1	4.0	4.8
72	···	···	···	···	···	···	0.4	1.8	1.3	1.3	2.3
73	···	···	···	···	···	···	1.3	3.4	6.0	3.2	6.9
74	···	···	···	···	···	···	3.9	2.2	3.5	3.7	6.5

Table 5.2 (cont'd)

ID	Pa β	$\log(L_{acc,Pa\beta}/L_\odot)$	Br γ	$\log(L_{acc,Br\gamma}/L_\odot)$	H_2	[Fe II] (1.644Å)	Ca I	Na I	CO (2.293)	CO (2.322)	CO(2.352)
75	-12.3	3.1	-5.1	1.1	···	···	1.0	2.8	3.2	2.1	3.3
76	-5.3	2.8	-1.9	0.9	···	···	1.1	2.6	1.9	3.2	4.5
77	···	···	···	···	···	···	1.8	2.6	5.6	2.0	···
78	···	···	···	···	···	···	3.8	5.3	5.2	5.1	5.1
79	···	···	···	···	···	···	3.1	3.7	5.6	0.8	6.0
80	···	···	···	···	···	···	1.6	1.4	4.7	3.5	4.1
81	···	···	···	···	···	···	2.1	···	···	···	···
82	···	···	···	···	···	···	-0.1	-2.2	1.0	11.0	4.0
83	-18.7	2.8	-2.9	0.9	···	···	37.8	···	···	···	···
84	···	···	···	···	···	···	1.6	0.8	6.1	3.3	6.7
85	···	···	···	···	···	···	0.9	2.3	4.6	4.7	5.7
86	···	···	···	···	···	···	2.5	2.9	5.5	4.4	7.6
87	···	···	···	···	···	···	···	···	···	···	···
88	···	···	···	···	···	···	1.5	3.5	-80.6	···	3.0
89	···	···	···	···	···	···	1.0	···	···	···	···
90	···	···	···	···	···	···	3.9	4.8	4.2	4.1	4.7
91	···	···	···	···	···	···	4.3	3.6	7.4	5.9	6.8
92	···	···	···	···	···	···	3.5	···	···	···	···
93	···	···	···	···	···	···	-3.1	-0.6	9.1	-3.2	2.0
94	···	···	···	···	···	···	2.8	1.7	6.2	3.1	3.9
95	···	···	···	···	···	···	7.7	6.0	6.6	6.5	4.9
96	-9.2	-0.6	-4.6	-0.5	···	···	-12.6	···	···	···	···
97	···	···	···	···	···	···	4.0	1.1	4.9	0.8	7.1
98	···	···	···	···	···	···	1.4	0.3	-59.8	···	···
99	···	···	···	···	···	···	4.2	1.4	4.1	4.6	···
100	···	···	···	···	···	···	5.0	3.5	6.7	5.4	6.8
101	-3.9	1.7	-3.2	0.6	···	···	2.6	1.2	3.2	2.3	1.8
102	-25.0	···	-5.8	-0.3	-3.2	···	1.0	1.1	-0.8	1.0	-0.2
103	-10.8	0.2	-8.2	-0.2	···	-2.2	3.0	1.6	2.1	2.4	1.9
104	···	···	···	···	···	···	2.1	1.1	1.8	2.4	1.9
105	···	···	-3.9	···	···	···	5.7	2.0	1.2	4.8	1.2
106	···	···	-6.3	-0.2	···	···	4.1	1.3	4.6	2.3	4.7
107	···	···	···	···	···	···	3.8	1.2	15.0	0.5	13.0
108	-2.7	0.8	-2.4	···	···	···	2.9	1.2	3.5	3.2	2.1
109	-9.5	2.1	-7.5	1.0	···	···	2.7	1.3	1.3	1.5	-0.5
110	···	···	···	···	···	···	4.4	1.4	6.5	4.1	5.5
111	···	···	···	···	···	···	7.4	3.6	7.0	4.8	5.3

Table 5.2 (cont'd)

ID	Pa β	$\log(L_{acc,Pa\beta}/L_\odot)$	Br γ	$\log(L_{acc,Br\gamma}/L_\odot)$	H_2	[Fe II] (1.644Å)	Ca I	Na I	CO (2.293)	CO (2.322)	CO(2.352)
112	-4.4	-0.0	-4.1	-0.3	···	···	3.6	1.7	4.6	2.6	3.0
113	-18.4	2.2	-9.1	1.4	-4.9	···	2.2	0.8	1.0	-47.9	···
114	···	···	···	···	···	···	-0.8	-3.8	-9.5	-5.4	-1.9
115	···	···	···	···	···	···	4.3	2.8	5.7	2.4	3.0

CHAPTER 6

Conclusions

6.1 Competitive Accretion and the IMF in Non-clustered Environment

In Chapter 2, we presented numerical experiments using the Gadget-2 SPH simulations with sink particles. The goal of this numerical experiment is to test whether the competitive accretion model applies to initial conditions where the cloud does not follow a spherical cluster gravitational potential that are commonly used in previous simulations (Bonnell et al., 2001a,b). We used a flat sheet-like geometry that has a shallow gravitational potential. In our simple setup, the differential gas accretion onto protostars under gravity gives rise to the high-mass end of the IMF, with slopes that gradually flattens and approaches $\Gamma = 1$.

When looking at the individual sinks, the mass growth rate of high-mass sinks follows $\dot{M} \propto M^2$, while the low-mass sinks lose the competition and accrete under this rate. By increasing the initial randomness such as variations in initial clumps masses and surface density, we obtain a power-law tail that flattens faster. In our simulations, the asymptotic slope is not reached and we had to terminate the simulation around one free-fall time of the cloud due to gas depletion. In real molecular cloud environments, we expect that the accretion process will terminate due to stellar feedback and gas depletion.

Because of our simple setup, we are able to identify the most important physical processes that contribute to the high-mass end of the IMF: gravity and Bondi-Hoyle accretion. The Bondi-Hoyle accretion works similarly in a sheet-like geometry and in a spherical cluster and results in the Salpeter-like slope in both cases. In the

simulations, we start with a spatially random distribution of sinks. As the system evolves, sinks tend to aggregate into small groups as a result of gravitational focusing. The small groups can further merge and form clusters. Bressert et al. (2010) have shown that the YSOs form in a smooth distribution of surface densities instead of two discrete modes (cluster vs. distributed), which is consistent with predictions of hierarchically structured star-formation. We also noted in our simulation that the clusters form in a way similar to sink particles accrete and $\Gamma \sim 1$ power-law distributions are also found in the cluster mass function (e.g., Zhang & Fall 1999; Chandar 2009; Chandar et al. 2010), suggesting that the cluster mass function could be the result of a similar process on a larger scale. If we increase the scale of our simulations with many more sink particles, it will be possible to follow the mass distribution of groups into clusters and compare the clustering of sinks to the observations.

In our simulations, we omitted several physical processes that also affect the high-mass IMF. For example, by manually populating the sinks, we omitted the problem of creating density enhancements through turbulence (see Mac Low & Klessen 2004 and references therein) and details of how gravitational fragmentation depends thermal properties of the molecular cloud (Larson, 2005). Additionally, including feedback from high mass stars can have interesting effects such as heating up the cloud and suppressing fragmentation (Krumholz et al., 2010), slowing down the star-formation process and preventing the most massive stars from accreting more material (Dale & Bonnell, 2008) and disrupting the cloud through photoionization and/or supernova explosions (Dale et al., 2012). While it could be difficult to self-consistently model the feedback processes, it is possible to mimic the effects of feedback. The effect of photoionization and supernovae can be modeled by removing gas over the corresponding timescale.

Besides feedback, another aspect of the simulation that we can improve on is using more realistic molecular cloud geometry. Heitsch & Hartmann (2008) studied the formation of molecular clouds in large-scale colliding flows with self-gravity. In these simulations, atomic gas is compressed and piled up at the interface of two colliding flows and form molecular gas. The molecular gas piles up until its self-gravity is

strong enough so that the molecular cloud starts collapsing. The small perturbation in the colliding front leads to irregular molecular clouds and dense cores naturally appears from gravitational focusing. The colliding flow model provides a physically motivated way to create initial conditions for our simulations.

6.2 Observational Evidence of Environmental Dependence of the IMF

In Chapter 3 and 4, we presented two parts of a project on searching for evidence of density dependence of the stellar IMF. We used the Orion A molecular cloud as our case study. It is home to the nearest large cluster of YSOs, the ONC, as well as the low-density star-forming region L1641, just south of the ONC.

In Chapter 3, we presented results from an optical photometric and spectroscopic survey of the young stellar population in L1641 to show that L1641 has a large enough low-mass population to make the known lack of high-mass stars a statistically-significant result. Our spectroscopic sample consists of IR-excess objects selected from the *Spitzer/IRAC* survey and non-excess objects selected from optical photometry. We have spectral confirmation of 864 members, with another 98 probable members; of the confirmed members, 406 have infrared excesses and 458 do not. Assuming the same ratio of stars with and without IR excesses in the highly-extincted regions, L1641 may contain as many as ~ 1600 stars down to $\sim 0.1 M_{\odot}$, comparable within a factor of two to the the ONC. Compared to the standard models of the IMF, L1641 is deficient in O and early B stars to a 3-4σ significance level, assuming that we know of all the massive stars in L1641.

In Chapter 4, we extended the survey to identify the intermediate mass (late B to G) L1641 members in an attempt to make a more direct comparison with the mass function of the nearby ONC. The spectral type distribution and the K-band luminosity function of L1641 are similar to those of the ONC (Hillenbrand, 1997; Muench et al., 2002), but problems of incompleteness and contamination prevent us from making a detailed test for differences. We limit our analysis to statistical

tests of the ratio of high-mass to low-mass stars, which indicate a probability of only 3% that the ONC and the southern region of L1641 were drawn from the same population. While our results support the hypothesis that the upper mass end of the IMF is dependent on environmental density, our results also demonstrate that a large sample size is key to finding IMF variations. To build up the low-density stellar population, we can combine several small low-density star-forming regions. If we combine the population of Taurus ($\sim$ 350 members; Luhman et al. 2009, 2010), Ophiuchus ($\sim$ 300 members; Wilking et al. 2008), Chamaeleon($\sim$ 240 members in Cha I and $\sim$ 50 in Cha II; Luhman 2008), and L1641 ($\sim$ 1000; Hsu et al. 2012, 2013), we can constrain the highmass IMF with a large population of nearly 2000 stars.

In Chapter 5, we used MMIRS (the MMT and Magellan Infrared Spectrograph) H & K band spectroscopy of embedded YSOs in L1641. 115 YSOs were observed, including 27 class I protostars and 88 class II's (pre-main sequence star with disk). The shape of the water vapor band allows us to obtain spectral-types for M type stars. Comparing IR and optical spectral types while both are available demonstrates that the IR spectral types generally agree with the optical spectral types. We use hydrogen recombination lines (Paschen β at 1.28μm and Brackett γ at 2.16μm) to estimate the accretion luminosities. The MMIRS observations also confirmed that there are no other A or earlier type stars in the embedded region we observed, with the caveat that the coverage with MMIRS is much smaller than the whole L1641 field previously observed.

With spectra and photometry of the majority of optical members and a small fraction of IR members, we now have a large catalog of members of L1641. This provides us with many opportunities to further study this region. For example, we can expand on the studies of Fang et al. (2009) and investigate the accretion properties over a large spatial range. We also have potential targets for a radial velocity study in L1641 to complement the radial velocity study of the ONC (Tobin et al., 2009). Our YSO list will also used to match the radio non-thermal emitters to identify potential targets for the VLBA Gould's Belt Distance Survey (Loinard, 2013). Combined the radio velocity studies and the VLBA distance and proper motion measurements, we

will have a three dimensional understanding of the structure and kinematics of the Orion A molecular cloud.

To further search for evidence of environmental dependence of the IMF, we need to extend our studies of stellar populations to larger number of stars and wider range of environments. This requires observations beyond the nearest star-forming regions out to the molecular ring of the Galaxy and the giant molecular clouds toward the Galactic center. An angular resolution of 0.1″is needed to resolve individual stars in regions as dense as the Trapezium cluster out to 8kpc. Next-generation facilities such as JWST and adaptive optics systems for large ground-based telescopes will provide the angular resolution required to distinguish individual stars such dense distant regions.

BIBLIOGRAPHY

Abt, H. A. 2008, ApJS, 176, 216

Abt, H. A. & Levato, H. 1977, PASP, 89, 797

Allen, L., Megeath, S. T., Gutermuth, R., Myers, P. C., Wolk, S., Adams, F. C., Muzerolle, J., Young, E., & Pipher, J. L. 2007, Protostars and Planets V, 361

Allen, L. E. 1995, PhD thesis, University of Massachusetts, Amherst

Allen, L. E. & Davis, C. J. 2008, Low Mass Star Formation in the Lynds 1641 Molecular Cloud, ed. Reipurth, B., 621

Bally, J., Lanber, W. D., Stark, A. A., & Wilson, R. W. 1987, ApJ, 312, L45

Baraffe, I., Chabrier, G., Allard, F., & Hauschildt, P. H. 1998, A&A, 337, 403

Bastian, N., Covey, K. R., & Meyer, M. R. 2010, ARA&A, 48, 339

Bate, M. R. 2009, MNRAS, 397, 232

Bate, M. R., Bonnell, I. A., & Bromm, V. 2003, MNRAS, 339, 577

Bate, M. R., Bonnell, I. A., & Price, N. M. 1995, MNRAS, 277, 362

Bessell, M. S. 1991, AJ, 101, 662

Bessell, M. S. & Brett, J. M. 1988, PASP, 100, 1134

Bigelow, B. C. & Dressler, A. M. 2003, in Society of Photo-Optical Instrumentation Engineers (SPIE) Conference Series, Vol. 4841, Society of Photo-Optical Instrumentation Engineers (SPIE) Conference Series, ed. M. Iye & A. F. M. Moorwood, 1727–1738

Binney, J., Merrifield, M., & Wegner, G. A. 2000, American Journal of Physics, 68, 95

Bondi, H. & Hoyle, F. 1944, MNRAS, 104, 273

Bonnell, I. A., Bate, M. R., Clarke, C. J., & Pringle, J. E. 2001a, MNRAS, 323, 785

Bonnell, I. A., Bate, M. R., & Vine, S. G. 2003, MNRAS, 343, 413

Bonnell, I. A., Clark, P., & Bate, M. R. 2008, MNRAS, 389, 1556

Bonnell, I. A., Clarke, C. J., Bate, M. R., & Pringle, J. E. 2001b, MNRAS, 324, 573

Bonnell, I. A., Larson, R. B., & Zinnecker, H. 2007, in Protostars and Planets V, ed. B. Reipurth, D. Jewitt, & K. Keil, 149

Bonnell, I. A., Vine, S. G., & Bate, M. R. 2004, MNRAS, 349, 735

Bressert, E., et al. 2010, MNRAS, 409, L54

Briceno, C., Hartmann, L. W., Stauffer, J. R., Gagne, M., Stern, R. A., & Caillault, J.-P. 1997, AJ, 113, 740

Burkert, A. & Hartmann, L. 2004, ApJ, 616, 288

Calvet, N., Hartmann, L., & Strom, S. E. 2000, Protostars and Planets IV, 377

Calvet, N., Muzerolle, J., Briceño, C., Hernández, J., Hartmann, L., Saucedo, J. L., & Gordon, K. D. 2004, AJ, 128, 1294

Cardelli, J. A., Clayton, G. C., & Mathis, J. S. 1989, ApJ, 345, 245

Chabrier, G. 2003, PASP, 115, 763

Chabrier, G. 2005, in Astrophysics and Space Science Library, Vol. 327, The Initial Mass Function 50 Years Later, ed. E. Corbelli, F. Palla, & H. Zinnecker, 41

Chandar, R. 2009, Ap&SS, 324, 315

Chandar, R., et al. 2010, ApJ, 719, 966

Clark, P. C., Glover, S. C. O., Bonnell, I. A., & Klessen, R. S. 2009, ArXiv e-prints

Clarke, C. J. 2009, Ap&SS, 324, 121

Connelley, M. S. & Greene, T. P. 2010, AJ, 140, 1214

Da Rio, N., Robberto, M., Soderblom, D. R., Panagia, N., Hillenbrand, L. A., Palla, F., & Stassun, K. 2009, ApJS, 183, 261

Da Rio, N., Robberto, M., Soderblom, D. R., Panagia, N., Hillenbrand, L. A., Palla, F., & Stassun, K. G. 2010, ApJ, 722, 1092

Dale, J. E. & Bonnell, I. A. 2008, MNRAS, 391, 2

Dale, J. E., Ercolano, B., & Bonnell, I. A. 2012, MNRAS, 424, 377

Derviz, T. E. 1983, Trudy Astronomicheskoj Observatorii Leningrad, 38, 62

Elmegreen, B. G. 2004, MNRAS, 354, 367

Elmegreen, B. G. 2009, in The Evolving ISM in the Milky Way and Nearby Galaxies

Elmegreen, B. G. & Efremov, Y. N. 1997, ApJ, 480, 235

Espinoza, P., Selman, F. J., & Melnick, J. 2009, A&A, 501, 563

Fabricant, D., et al. 2005, PASP, 117, 1411

Fang, M., van Boekel, R., Wang, W., Carmona, A., Sicilia-Aguilar, A., & Henning, T. 2009, A&A, 504, 461

Fisher, R. A. 1925, Statistical Methods for Research Workers (Edinburgh: Oliver and Boyd)

Gâlfalk, M. & Olofsson, G. 2008, A&A, 489, 1409

Gutermuth, R. A., Megeath, S. T., Myers, P. C., Allen, L. E., Pipher, J. L., & Fazio, G. G. 2009, ApJS, 184, 18

Gutermuth, R. A., Pipher, J. L., Megeath, S. T., Myers, P. C., Allen, L. E., & Allen, T. S. 2011, ApJ, 739, 84

Harayama, Y., Eisenhauer, F., & Martins, F. 2008, ApJ, 675, 1319

Hartmann, L. 2003, ApJ, 585, 398

Hartmann, L., Ballesteros-Paredes, J., & Bergin, E. A. 2001, ApJ, 562, 852

Heitsch, F. & Hartmann, L. 2008, ApJ, 689, 290

Heitsch, F., Hartmann, L. W., & Burkert, A. 2008a, ApJ, 683, 786

Heitsch, F., Hartmann, L. W., Slyz, A. D., Devriendt, J. E. G., & Burkert, A. 2008b, ApJ, 674, 316

Heitsch, F., Slyz, A. D., Devriendt, J. E. G., Hartmann, L. W., & Burkert, A. 2006, ApJ, 648, 1052

Hennebelle, P. & Chabrier, G. 2008, ApJ, 684, 395

Hernández, J., Calvet, N., Briceño, C., Hartmann, L., & Berlind, P. 2004, AJ, 127, 1682

Hillenbrand, L. A. 1997, AJ, 113, 1733

Hillenbrand, L. A. & Hartmann, L. W. 1998, ApJ, 492, 540

Høg, E., Fabricius, C., Makarov, V. V., Urban, S., Corbin, T., Wycoff, G., Bastian, U., Schwekendiek, P., & Wicenec, A. 2000, A&A, 355, L27

Hsu, W.-H., Hartmann, L., Allen, L., Hernández, J., Megeath, S. T., Mosby, G., Tobin, J. J., & Espaillat, C. 2012, ApJ, 752, 59

Hsu, W.-H., Hartmann, L., Allen, L., Hernández, J., Megeath, S. T., Tobin, J. J., & Ingleby, L. 2013, ApJ, 764, 114

Hsu, W.-H., Hartmann, L., Heitsch, F., & Gómez, G. C. 2010, ApJ, 721, 1531

Jappsen, A., Klessen, R. S., Larson, R. B., Li, Y., & Mac Low, M. 2005, A&A, 435, 611

Jenkins, A., Frenk, C. S., White, S. D. M., Colberg, J. M., Cole, S., Evrard, A. E., Couchman, H. M. P., & Yoshida, N. 2001, MNRAS, 321, 372

Jones, B. F., Shetrone, M., Fischer, D., & Soderblom, D. R. 1996, AJ, 112, 186

Kenyon, S. J. & Hartmann, L. 1995, ApJS, 101, 117

Kim, M. K., et al. 2008, PASJ, 60, 991

Kirk, H. & Myers, P. C. 2012, ApJ, 745, 131

Klein, R. I., Inutsuka, S., Padoan, P., & Tomisaka, K. 2007, in Protostars and Planets V, ed. B. Reipurth, D. Jewitt, & K. Keil, 99–116

Klessen, R. S. & Burkert, A. 2001, ApJ, 549, 386

Klessen, R. S., Heitsch, F., & Mac Low, M. 2000, ApJ, 535, 887

Koenigl, A. 1991, ApJ, 370, L39

Kroupa, P. 2001, MNRAS, 322, 231

Kroupa, P. & Weidner, C. 2003, ApJ, 598, 1076

Kroupa, P. & Weidner, C. 2005, in Astrophysics and Space Science Library, Vol. 327, The Initial Mass Function 50 Years Later, ed. E. Corbelli, F. Palla, & H. Zinnecker, 175

Krumholz, M. R., Cunningham, A. J., Klein, R. I., & McKee, C. F. 2010, ApJ, 713, 1120

Krumholz, M. R., Klein, R. I., & McKee, C. F. 2012, ApJ, 754, 71

Krumholz, M. R. & McKee, C. F. 2005, ApJ, 630, 250

Kryukova, E., Megeath, S. T., Gutermuth, R. A., Pipher, J., Allen, T. S., Allen, L. E., Myers, P. C., & Muzerolle, J. 2012, AJ, 144, 31

Lada, C. J. 2006, ApJ, 640, L63

Lada, C. J. & Lada, E. A. 2003, ARA&A, 41, 57

Lamb, J. B., Oey, M. S., Werk, J. K., & Ingleby, L. D. 2010, ApJ, 725, 1886

Larson, R. B. 2005, MNRAS, 359, 211

Leggett, S. K. 1992, ApJS, 82, 351

Lejeune, T. & Schaerer, D. 2001, A&A, 366, 538

Loinard, L. 2013, in IAU Symposium, Vol. 289, IAU Symposium, ed. R. de Grijs, 36–43

Luhman, K. L. 2000, ApJ, 544, 1044

Luhman, K. L. 2007, ApJS, 173, 104

Luhman, K. L. 2008, Chamaeleon, ed. B. Reipurth, 169

Luhman, K. L., Allen, P. R., Espaillat, C., Hartmann, L., & Calvet, N. 2010, ApJS, 186, 111

Luhman, K. L., Mamajek, E. E., Allen, P. R., & Cruz, K. L. 2009, ApJ, 703, 399

Luhman, K. L., Stauffer, J. R., Muench, A. A., Rieke, G. H., Lada, E. A., Bouvier, J., & Lada, C. J. 2003, ApJ, 593, 1093

Mac Low, M.-M. & Klessen, R. S. 2004, Reviews of Modern Physics, 76, 125

Martini, P., et al. 2011, PASP, 123, 187

Maschberger, T., Clarke, C. J., Bonnell, I. A., & Kroupa, P. 2010, MNRAS, 404, 1061

Maschberger, T. & Kroupa, P. 2009, MNRAS, 395, 931

Massi, F., Testi, L., & Vanzi, L. 2006, A&A, 448, 1007

McKee, C. F. & Ostriker, E. C. 2007, ARA&A, 45, 565

McKee, C. F. & Tan, J. C. 2002, Nature, 416, 59

McKee, C. F. & Williams, J. P. 1997, ApJ, 476, 144

McLeod, B., et al. 2012, PASP, 124, 1318

Megeath, S. T., et al. 2012, AJ, 144, 192

Menten, K. M., Reid, M. J., Forbrich, J., & Brunthaler, A. 2007, A&A, 474, 515

Meyer, M. R., Calvet, N., & Hillenbrand, L. A. 1997, AJ, 114, 288

Mink, D. J., Wyatt, W. F., Caldwell, N., Conroy, M. A., Furesz, G., & Tokarz, S. P. 2007, in Astronomical Society of the Pacific Conference Series, Vol. 376, Astronomical Data Analysis Software and Systems XVI, ed. R. A. Shaw, F. Hill, & D. J. Bell, 249–+

Monet, D. G., et al. 2003, AJ, 125, 984

Muench, A. A., Lada, E. A., Lada, C. J., & Alves, J. 2002, ApJ, 573, 366

Muzerolle, J., Hartmann, L., & Calvet, N. 1998, AJ, 116, 2965

Padoan, P. & Nordlund, Å. 2002, ApJ, 576, 870

Padoan, P., Nordlund, Å., Kritsuk, A. G., Norman, M. L., & Li, P. S. 2007, ApJ, 661, 972

Perryman, M. A. C. & ESA, eds. 1997, ESA Special Publication, Vol. 1200, The HIPPARCOS and TYCHO catalogues. Astrometric and photometric star catalogues derived from the ESA HIPPARCOS Space Astrometry Mission

Proszkow, E., Adams, F. C., Hartmann, L. W., & Tobin, J. J. 2009, ApJ, 697, 1020

Racine, R. 1968, AJ, 73, 233

Rayner, J. T., Cushing, M. C., & Vacca, W. D. 2009, ApJS, 185, 289

Rebull, L. M., et al. 2011, ApJS, 196, 4

Robberto, M., Soderblom, D. R., Scandariato, G., Smith, K., Da Rio, N., Pagano, I., & Spezzi, L. 2010, AJ, 139, 950

Robin, A. C., Reylé, C., Derrière, S., & Picaud, S. 2003, A&A, 409, 523

Rybicki, G. B. 1971, Ap&SS, 14, 15

Salpeter, E. E. 1955, ApJ, 121, 161

Schaller, G., Schaerer, D., Meynet, G., & Maeder, A. 1992, A&AS, 96, 269

Siess, L., Dufour, E., & Forestini, M. 2000, A&A, 358, 593

Skiff, B. A. 2010, VizieR Online Data Catalog, 1, 2023

Skrutskie, M. F., et al. 2006, AJ, 131, 1163

Skumanich, A. 1972, ApJ, 171, 565

Springel, V. 2005, MNRAS, 364, 1105

Springel, V., Yoshida, N., & White, S. D. M. 2001, New Astronomy, 6, 79

Stauffer, J. R., Hartmann, L. W., Prosser, C. F., Randich, S., Balachandran, S., Patten, B. M., Simon, T., & Giampapa, M. 1997, ApJ, 479, 776

Stoll, R., Martini, P., Derwent, M. A., Gonzalez, R., O'Brien, T. P., Pappalardo, D. P., Pogge, R. W., Wong, M.-H., & Zhelem, R. 2010, in Society of Photo-Optical Instrumentation Engineers (SPIE) Conference Series, Vol. 7735, Society of Photo-Optical Instrumentation Engineers (SPIE) Conference Series

Stolte, A., Brandner, W., Brandl, B., & Zinnecker, H. 2006, AJ

Stolte, A., Brandner, W., Grebel, E. K., Lenzen, R., & Lagrange, A.-M. 2005, ApJ, 628, L113

Sung, H. & Bessell, M. S. 2004, AJ, 127, 1014

Sung, H., Bessell, M. S., & Chun, M.-Y. 2004, AJ, 128, 1684

Tan, J. C., Krumholz, M. R., & McKee, C. F. 2006, ApJ, 641, L121

Tobin, J. J., Hartmann, L., Furesz, G., Mateo, M., & Megeath, S. T. 2009, ApJ, 697, 1103

Vázquez-Semadeni, E., Gómez, G. C., Jappsen, A. K., Ballesteros-Paredes, J., González, R. F., & Klessen, R. S. 2007, ApJ, 657, 870

Vázquez-Semadeni, E., Ryu, D., Passot, T., González, R. F., & Gazol, A. 2006, ApJ, 643, 245

Walborn, N. R. & Fitzpatrick, E. L. 1990, PASP, 102, 379

Warren, W. H. & Hesser, J. E. 1977, ApJS, 34, 115

Weidner, C. & Kroupa, P. 2006, MNRAS, 365, 1333

Weidner, C., Kroupa, P., & Bonnell, I. A. D. 2010, MNRAS, 401, 275

White, R. J. & Basri, G. 2003, ApJ, 582, 1109

Wilking, B. A., Gagné, M., & Allen, L. E. 2008, Star Formation in the ρ Ophiuchi Molecular Cloud, ed. B. Reipurth, 351

Zacharias, N., Finch, C. T., Girard, T. M., Henden, A., Bartlet, J. L., Monet, D. G., & Zacharias, M. I. 2012, VizieR Online Data Catalog, 1322, 0

Zhang, Q. & Fall, S. M. 1999, ApJ, 527, L81

Zinnecker, H. 1982, New York Academy Sciences Annals, 395, 226

Zinnecker, H. & Yorke, H. W. 2007, ARA&A, 45, 481

Zorec, J., Cidale, L., Arias, M. L., Frémat, Y., Muratore, M. F., Torres, A. F., & Martayan, C. 2009, A&A, 501, 297